**Coherent Electron Cooling and Two Stream Instabilities Due to Electron Cooling**

A Dissertation Presented

by

**Gang Wang**

to

The Graduate School

in Partial fulfillment of the

Requirements

for the Degree of

**Doctor of Philosophy**

in

**Physics**

Stony Brook University

**December 2008**

**Stony Brook University**

The Graduate School

Gang Wang

We, the dissertation committee for the above candidate for the Doctor of Philosophy degree, hereby recommend acceptance of this dissertation.

Ilan Ben-Zvi – Dissertation Advisor
Adjunct Professor, Department of Physics and Astronomy

Jacobus Verbaarschot – Chairperson of Defense
Professor, Department of Physics and Astronomy

Thomas K. Hemmick
Distinguished Teaching Professor, Department of Physics and Astronomy

Jorg Kewisch
Scientist, Collider Accelerator Department, Brookhaven National Laboratory

This dissertation is accepted by the Graduate School.

Lawrence Martin
Dean of the Graduate School

Abstract of the Dissertation

**Coherent Electron Cooling and Two Stream Instabilities Due to Electron Cooling**

by

Gang Wang

**Doctor of Philosophy**

in

**Physics**

Stony Brook University

2008

This thesis deals with beam dynamics issues associated with electron cooling of an ion beam in a storage ring. In the presence of electron cooling, various effects could happen to the circulating ion beam other than the desired incoherent cooling due to scattering. Firstly, the long-range Coulomb's interaction between the ions and electrons can coherently stabilize or destabilize the ion beam depending on certain cooling schemes. Secondly, as a result of cooling, the momentum spread could be reduced too much such that the Landau damping cease to stabilize the beam and cause the so-called 'over-cooling'. Finally, the coherent effects of the electron beam can serve as a mechanism for stochastic cooling. Under certain circumstance, the coherent electron cooling rate can be much higher than what is due to scattering.

The coherent instabilities of monopole, dipole and quadruple type were studied and their thresholds as well as growth rates are given. For magnetized electron cooling scheme, the ion clouds accumulation was studied and their effects on the two stream instabilities were calculated for the RHIC parameters. A simulation code, TRANFT, was

used to track the ion beam in presence of the electron coherent force and coupling impedance of the accelerator. The instability threshold for the energy spread and the bunch population was found from the simulation and compared with the theoretical estimate.

Beyond the stability issues, the long range Coulomb force from the electron beam can also be used to cool the ion beam which brings the new concept of cooling, the coherent electron cooling. The basic concept of the coherent electron cooling is introduced and the dynamics of the first process, the modulation process, and the second process, the FEL amplification process, have been studied in detail. It is shown that analytic formula can be derived to estimate the electron response to a moving ion under certain assumptions and the FEL amplification process can be analytically described by 1D FEL theory. For more general cases of the modulation process, the numerical calculation is also presented.

# Contents

## LIST OF FIGURES

# LIST OF TABLES

## ACKNOWLEGMENTS

I would like to thank my advisor, Dr. Ilan Ben-zvi, for introducing me into the field of accelerator physics, encouraging me to explore the exciting subject of electron cooling theory and being supportive all the time. A major amount of this work is under the supervision and help of Dr. Michael Blaskiewicz without whom many theoretical and simulation progresses shown here would be impossible. I also want to express my gratitude to Dr. Alexei Fedotov for suggestions and help with the subject of electron cooling related instabilities. Many members from the BNL Superconducting Accelerator and Electron Cooling group provide important and very useful discussions on this work. Among them are Prof. Vladimir N. Litvinenko, Dr. Ady Hershcovitch, Dr. Nikolayn Malitsky, Dr. Jörg Kewisch and Dr. Xiangyun Chang. Many calculations about RHIC Electron Cooling two stream instabilities are based on the theory developed by Prof. V. Parkhomchuk and Dr. V. B. Reva. I would like to thank them for providing detailed information and helpful discussions. I want to thank my committee members Prof. Ilan Ben-Zvi, Prof. Thomas K. Hemmick, Prof. Jacobus Verbaarschot, and Dr. Jörg Kewisch.

Financial support came from the US Department of Energy.

# CHAPTER 1. INTRODUCTION

## *1.1. Electron Cooling Technique*

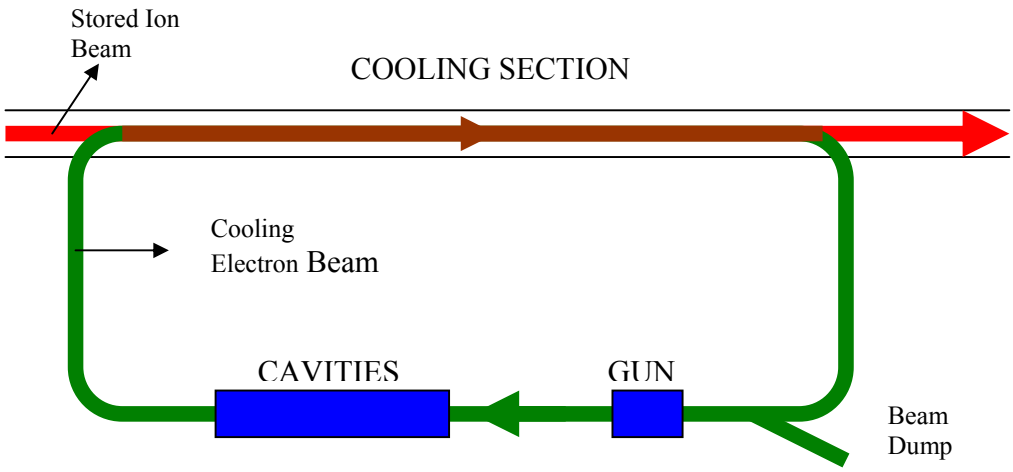


Figure 1.1 Schematic Graph of Electron Cooling.

As an essential tool of modern physics studies, particle accelerators are built around the world to generate high quality particle beams. One of the most important parameters to measure the performance of colliders is the Luminosity as defined below

$$L = \frac{N_i^2 f_b}{4\pi\varepsilon_\perp \beta^*}, \tag{1.1}$$

where $N_i$ is the bunch population, $f_b$ is the bunch repetition frequency, $\varepsilon_\perp$ is the transverse emittance and $\beta^*$ is the betatron function at Interaction Point. As can be seen in equation (1), the Luminosity can be increased by reducing the transverse emittance,

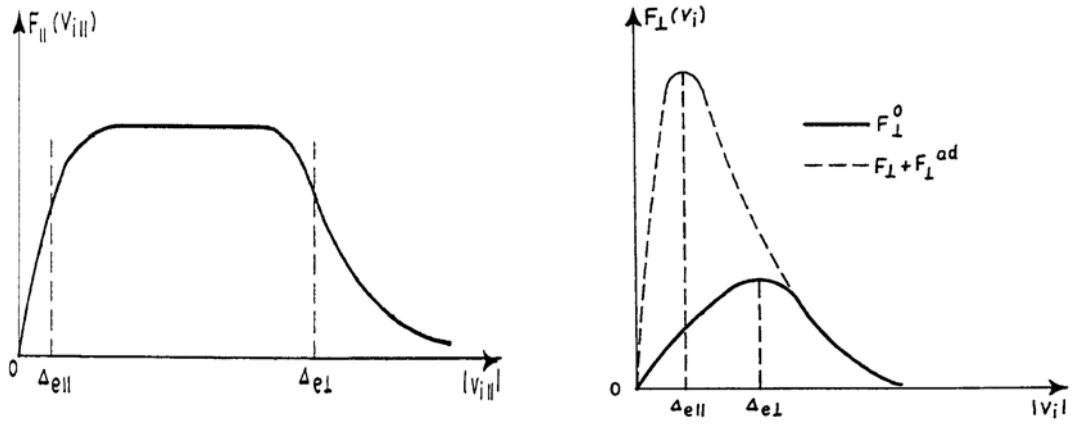


(a) (b)

Figure 1.2 Shape of Electron Cooling Force (Taken from ref.[1]). (a) Longitudinal electron cooling force without solenoid field as a function of the ion longitudinal velocity; (b) Transverse electron cooling force as a function of the ion transverse velocity. The solid curve is for cooling force without solenoid field and the dash curve is for cooling force with solenoid field.

and this is the objective of beam cooling. One of the most effective methods of beam cooling is Electron Cooling which was proposed by G.Budker in 1960s and demonstrated first in Novosibirsk, then later also at many other accelerators, including CERN and Fermilab. As shown in Fig.1.1, an electron cooler is composed of an electron gun, accelerating cavities, straight cooling section and beam dump. The cold electron beams are generated in the electron gun, accelerated to the same velocity of the ion beams and then merged with the ion beams. Through Coulomb collisions, the heat carried by the ions is transferred to the electrons and result in smaller ion beam emittances. The electron beam is renewed every turn and in the ideal case the final ion velocity spread is determined by the following relation,

$$\left\langle v_i^2 \right\rangle = \left\langle v_e^2 \right\rangle \frac{m_e}{m_i}, \tag{1.2}$$

where $\left\langle v_i^2 \right\rangle$ is the velocity spread of the ion and $\left\langle v_e^2 \right\rangle$ is the velocity spread of the cold electron beam generated by the electron cooler. Since the intra beam scattering within ions tends to increase the emittance, the electron cooling has to be faster than the IBS. The electron drag force for an ion moving with velocity $v_i$ can be estimated from the following formula

$$\frac{1}{\tau_i} = -\frac{F(v_i)}{p_i}, \tag{1.3}$$

where $F(v_i)$ is the drag force from the electrons and $p_i$ is the momentum of the moving ion in the commoving frame. A solenoid field is usually applied to the cooling section in order to hold the electron beam from expanding due to the space charge, increase the cooling rate or overcome the recombination of the ions with the cooling electrons. Figure 1.2 shows the shape of the cooling force as a function of the ion velocity and detailed derivation and asymptotic formula can be found in ref. [1]

## *1.2. RHIC-II Electron Cooler Design*

In order to upgrade RHIC to higher Luminosity and overcome the emittance growth due to IBS, electron cooling was proposed and studied by the electron cooling group of Brookhaven National Laboratory[2]. As shown in Fig.1.3, the designed electron cooler is

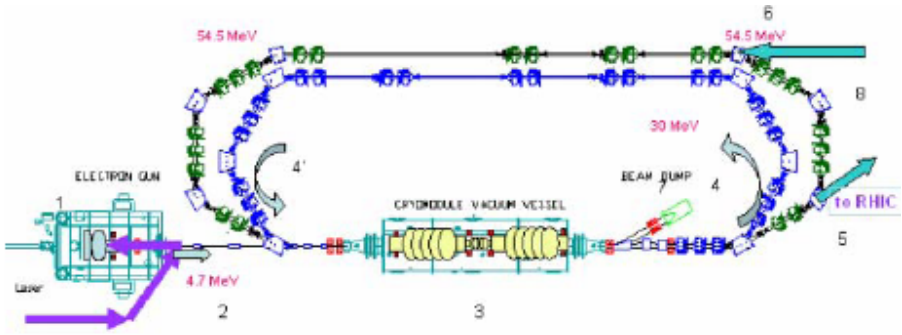


Figure 1.3 ERL Based Electron Cooler For RHIC-II (Taken from ref. [2]).

| Parameter | Value | Units |
|---|---|---|
| RF frequency | 703.75 | MHz |
| Bunch frequency | 9.38 | MHz |
| Bunch charge | 5 | Nano Coulombs |
| Gun kinetic energy | 4.7 | MeV |
| Linac kinetic energy | 54.34 | MeV |
| Normalized rms emittance | ~3 | μm |
| Momentum spread, rms | $1.8 \cdot 10^{-4}$ | - |
| Bunch length, rms | 7.8 | mm |

Table 1.1 RHIC eCOOLER Designed Parameters (Taken from ref. [2])

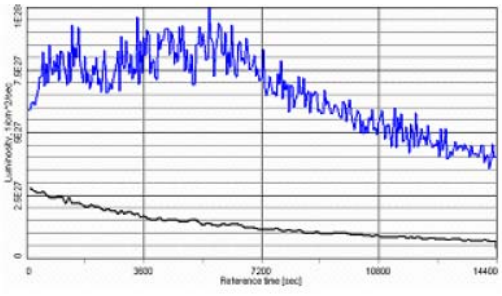

Figure 1.4 Simulation Result of The RHIC Gold Ion Luminosity With and Without Ecooling. The abscissa is the number of turns and the ordinate is the stored ion Luminosity. The snapshot is taken after 4 hours run (Taken from ref. [2]).

based on the Energy Recovery Linac. The electron beam is generated in the SRF gun, the electron bunch then passes the accelerating cavities twice in order to reach the required energy of 54 Mev. Then, the electron bunch is delivered to the RHIC cooling section to merge with the ion beam. A 180 degree turn has to be made by the electron beam such that both the blue and yellow ring could be cooled. The designed parameters are shown in Table 1.1. In the cooling section, a wiggler is included in order to reduce the recombination rate and a few short solenoids are used to overcome the expansion of the electron beam due to space charge. The simulation results show significant Luminosity increase due to RHIC electron cooling as shown in Fig.1.4 for the Au ion beam.

It is necessary to mention that a strong solenoid field of 5T was included in the initial design for the magnetized electron cooling scheme[3]. Some of its designed parameters are used in the calculations of the following chapters.

## *1.3 Coherent Two Stream Interactions In Electron Cooler*

According to the change of momentum and impact distance, the Coulomb interaction is divided into the collisions and the long range interaction. Typically, the cooling force and diffusion are caused by the collision and the long range interaction could be a reason for beam instability. As the cooling electron beam is renewed every turn, free energy may be introduced to the ion beams and drive the ion beam unstable[4, 5]. In the presence

of solenoid field, the instability threshold can be significantly affected by the ion clouds densities and the efficiency of the feedback system[6]. Usually, the low order instability has lower instability threshold than the higher order instabilities. However, as the dipole type instability can be corrected by a feedback system, higher order oscillations might also become dominant. When the electron beam density is below the instability threshold, the long range interaction will generally damp the coherent oscillation of the ion beam. The detailed modeling and calculations are described in the following chapters.

## *1.4 Coherent Electron Cooling*

It is mentioned in section 1.3 that the long range Coulomb force from the cooling electron beam can damp the coherent oscillation of the ion beam if the electron density is below certain instability threshold. This damping effect can be amplified through some instability mechanism such as the negative mass instability as mentioned in Ya. Derbenev's paper [7] and the instability growth in the Free Electron Laser as proposed recently by V. N. Litvinenko[8]. Since the coherent error is proportional to the RMS beam size or energy spread due to the central limit theory, the emittance can be reduced by continuously correcting the coherent signal and randomizing the beam. In other words, The basic idea of the Coherent Electron Cooling is to use the electron beam as the picking up and correcting devices to perform stochastic cooling.

For an ideal electron beam with zero temperature in all direction, the calculations have been made in previous work for various accelerators and significant short cooling times have been estimated[8]. A slightly different description of the coherent electron cooling process is given in section 6.1 for cold electron beam, which adopt the wave description instead of the single particle description but should essentially be equivalent to the latter. The modeling and calculations for finite temperature electron beam are also made in Chapter 6, especially for the modulation process. Further study of the physics encountered in the Coherent Electron Cooling process is still work in progresses.

# CHAPTER 2. TWO STREAM DIPOLE INSTABILITY IN ABSENCE OF MAGNETIC FIELD

In 1998, a substantial shorter beam life time was observed as soon as the E-Cooler was turned on in Celsius and this phenomenon has been called 'electron heating'[9]. Similar phenomena have also been observed by other facilities such as NAP-M, Fermi lab, Indiana, TARN II and COSY. Although a nonlinear electric field is regarded as an important reason for the fast beam loss in Celsius due to the fact that the electron beams has a smaller radius than the ion beam, the coherent ion-electron beam interaction may also play a role. For RHIC e-cooler, since the electron beam and the ion beam have essentially the same beam size, the nonlinear electric field effects are greatly reduced and the coherent ion-electron interaction could be important for the ion beam stability. V.V.Parkhamchuk and V.B.Reva developed a dipole oscillation model to estimate the growth rate due to transversal coherent oscillation induced by electron beam[4, 5]. It is also shown that this coherent effect could be amplified in the presence of the ion clouds ionized from the residue gas3. This model is reviewed and applied to the RHIC electron cooling parameters. In section 2, the longitudinal two stream coupling is studied and the instability threshold is shown for the designed RHIC parameters. In section 3, the transverse two stream coupling equation is solved and the growth rate of the transverse coherent oscillation is estimated for the magnetized electron cooling scheme. The effects of the ion clouds in the cooling section have been taken into account and the dependence of the growth rate on the neutralization factor is derived[6]. The stability analysis of the

ion clouds motion inside the cooling section has also been made in order to estimate the neutralization ratio. It is shown that, in the presence of a strong longitudinal magnetic field, the ion clouds may not be removed by simply making a gap due to the Larmor oscillation resonance. The calculation for non-magnetized electron cooling design is given in subsection 3.4 and it shows that the designed electron density is three orders of magnitude smaller than the transverse instability threshold.

## *2.1. Longitudinal-Longitudinal Coupling*

### 2.1.1. Langmuir Oscillation Equations Of Motion

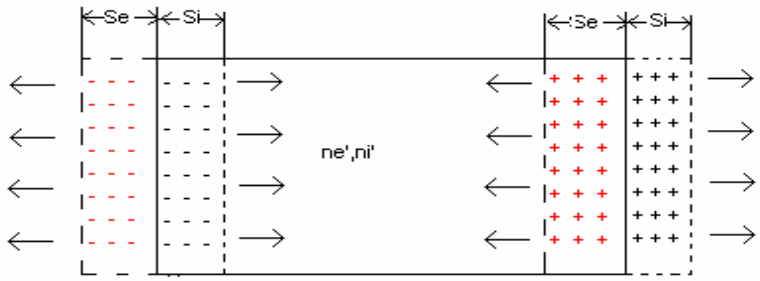


Figure 2.1: Illustration of Langmuir Oscillation. The coherent displacement of all ions/electrons within a local region of the ion beam, Si, makes the charge density inside the region different from the equilibrium and thus induces local electrostatic field, which in turn act back on the perturbing particles and make them oscillate around the equilibrium position.

In the presence of the electron beam, the longitudinal electrostatic oscillations (Langmuir oscillations) can be excited and amplified from turn to turn, leading to an ion beam instability [4-6]. As shown in Fig.2.1, the electron and ion displacement from their equilibrium position make the local longitudinal boundaries carry opposite surface charge

$$\sigma(z,t) = -en_e s_e(z,t) + Z_i en_i s_i(z,t),$$

where $Z_i$ is the ion charge number. Assuming the volume charge density variation due to the displacement within the considered region is negligible, the electrostatic field due to the displacement is

$$E_z(z,t) = \frac{1}{\varepsilon_0}\left(en_e s_e(z,t) - Z_i en_i s_i(z,t)\right). \tag{2.1}$$

The negative sign comes from the fact that the positive longitudinal displacement of positive charge particles introduces positive surface charge to the right boundary and thus creates a negative electrostatic field. The factor of 2 comes from the fact that both boundaries contribute the same amount of surface charge with opposite sign. The equations of longitudinal motion for an electron/ion within the considered region are thus,

$$m_e \frac{d^2 z_e}{dt^2} = -\frac{n_e e^2}{\varepsilon_0} s_e(z,t) + \frac{Z_i n_i e^2}{\varepsilon_0} s_i(z,t), \tag{2.2}$$

$$M_i \frac{d^2 z_i}{dt^2} = \frac{Z_i n_e e^2}{\varepsilon_0} s_e(z,t) - \frac{Z_i^2 n_i e^2}{\varepsilon_0} s_i(z,t). \tag{2.3}$$

Since inside the considered region, the longitudinal position of each particle is the sum of its equilibrium position and the longitudinal displacement, i.e.

$$z_{e,i} = z_{c,i}^0 + s_{e,i},$$

and since the unperturbed equilibrium position for each particle is independent of time, the equation of motion for the displacements have been obtained as following,

$$\frac{d^2 s_e}{dt^2} + \omega_{pe}^2 s_e = \omega_{ei}^2 s_i, \tag{2.4}$$

$$\frac{d^2 s_i}{dt^2} + \omega_{pi}^2 s_i = \omega_{ie}^2 s_e \tag{2.5}$$

, where the plasma frequencies are defined as[1]

$$\omega_{pe} = \sqrt{\frac{n_e e^2}{m_e \varepsilon_0}} = 1.504 \times 10^9 s^{-1}, \qquad \omega_{pi} = \sqrt{\frac{Z_i^2 n_i e^2}{M_i \varepsilon_0}} = 6.518 \times 10^6 s^{-1},$$

$$\omega_{ie} = \sqrt{\frac{Z_i n_e e^2}{M_i \varepsilon_0}} = 2.23 \times 10^7 s^{-1}, \qquad \omega_{ei} = \sqrt{\frac{Z_i n_i e^2}{m_e \varepsilon_0}} = 4.396 \times 10^8 s^{-1}.$$

### 2.1.2. Transfer Matrix for Langmuir Oscillation in Cooling Section

Given the initial condition, the equation (2.4) and (2.5) can be solved and thus the displacements at the back end of the cooling section can be obtained. Since the electron beam is much colder than the ion beam and will be renewed for each turn, the initial condition for the electron beam can be set to

[1] All the numbers are given for the commoving frame densities $n_i = 7.697 \times 10^{11} m^{-3}$ and $n_e = 7.117 \times 10^{16} m^{-3}$, which correspond to RHIC magnetized cooling parameters.

$$s_e(z,0) = 0\,, \tag{2.6}$$

$$\frac{d}{dt}s_e(z,0) = 0\,, \tag{2.7}$$

where $t = 0$ corresponds to front end of the cooling section. Equation (2.1) can be rewritten as,

$$E_z(z,t) = \frac{m_e}{e}\left(\omega_{pe}^2 s_e(z,t) - \omega_{ei}^2 s_i(z,t)\right). \tag{2.8}$$

By applying equation (2.4), (2.5) and (2.8), the differential equation for the longitudinal electric field can be derived as

$$\frac{d^2}{dt^2}E_z(z,t) = -\omega_0^2 E_z(z,t)\,,$$

where $\omega_0 = \sqrt{\omega_{pe}^2 + \omega_{pi}^2} = 1.504\times10^9\, s^{-1}$. Thus the longitudinal electric field due to the displacements of ions and electrons in the considered region turns out to be

$$E_z(z,t) = \hat{E}_z(z)\cos(\omega_0 t + \varphi)\,. \tag{2.10}$$

At $t = 0$, by equating equation (2.8) and (2.10), one gets

$$\cos(\varphi) = -\frac{m_e}{\hat{E}_z(z)e}\omega_{ei}^2 s_i(z,0)\,, \tag{2.11}$$

$$\sin(\varphi) = \frac{m_e}{\hat{E}_z(z)\omega_0 e}\omega_{ei}^2 \dot{s}_i(z,0)\,. \tag{2.12}$$

By equation (2.3) and (2.10), the equation of motion for ion displacement can be rewritten to

$$\frac{d^2}{dt^2}s_i(z,t) = \frac{Z_i e}{M_i}\hat{E}_z(z)\cos(\omega_0 t + \varphi)\,. \tag{2.13}$$

Integrating equation (2.13) over t, the velocity of the particles' longitudinal shift can be obtained,

$$\frac{d}{dt}s_i(z,t) = -\xi\omega_0 \sin(\omega_0\tau)s_i(z,0) + \left[\xi(\cos(\omega_0\tau)-1)+1\right]\dot{s}_i(z,0), \tag{2.14}$$

where $\xi = \frac{\omega_{pi}^2}{\omega_0^2} = 1.879\times10^{-5}$, $\tau = \frac{l_{cool}}{\gamma c}$ is the flight time in the commoving frame and $l_{cool}$ is the length of the cooling section. Then we can get the solution of the displacement, $s_i$ by integrating equation (2.14),

$$s_i(z,t) = \left[\xi(\cos(\omega_0\tau)-1)+1\right]s_i(z,0) + \frac{1}{\omega_0}\left[\xi\sin(\omega_0\tau) + (1-\xi)\omega_0\tau\right]\dot{s}_i(z,0). \tag{2.15}$$

From equation (2.14) and (2.15), the transfer matrix for the ion displacement due to coherent Langmuir oscillation in the cooling section is

$$M_{langmuir} = \begin{pmatrix} \xi(\cos(\omega_0\tau)-1)+1 & \frac{1}{\omega_0}\left[\xi\sin(\omega_0\tau)+(1-\xi)\omega_0\tau\right] \\ -\xi\omega_0\sin(\omega_0\tau) & \xi(\cos(\omega_0\tau)-1)+1 \end{pmatrix}. \tag{2.16}$$

Thus for each turn passing through the cooling section, the ions' local longitudinal displacements varies as

$$\begin{pmatrix} s_i \\ \dot{s}_i \end{pmatrix}_\tau = M_{langmuir}\begin{pmatrix} s_i \\ \dot{s}_i \end{pmatrix}.$$

The determinant of the transfer matrix can be represented in terms of the plasma frequencies as following,

$$\left|M_{langmuir}\right| = 1 + \frac{\omega_{ie}^2\omega_{ei}^2}{\omega_0^4}\omega_0\tau\sin(\omega_0\tau) + \frac{2\omega_{ie}^2\omega_{ei}^2}{\omega_0^4}(\cos(\omega_0\tau)-1), \tag{2.17}$$

where the relation $\omega_{pi}^2\omega_{pe}^2 = \omega_{ei}^2\omega_{ie}^2$ is used in the derivation. If $\left|M_{langmuir}\right| > 1$, the electron beam will transfer energy to the ion oscillation and thus increase the local electrostatic

oscillation and cause instability. From equation (2.17), the condition for $\left|M_{langmuir}\right|>1$ can be depicted as follows,

$$\left|M_{langmuir}\right|-1=\frac{4\omega_{ie}^2\omega_{ei}^2}{\omega_0^4}\sin^2(\frac{\omega_0\tau}{2})\left[\frac{\omega_0\tau}{2}\cot(\frac{\omega_0\tau}{2})-1\right]. \tag{2.18}$$

Thus the threshold for the determinant of the transfer matrix to be bigger than 1 is

$$\omega_0\tau=2\pi\,. \tag{2.19}$$

The RHIC gold beam parameters in the cooling section are shown in Table 1. As shown in Fig.2.3, the longitudinal electrostatic oscillation puts an electron density limitation, $n_{e,th}=1.24\times10^{16}\,m^{-3}$ , which correspond to $\omega_0\tau=2\pi$ , for the ion beam to be stable. For the current electron cooler design, the electron beam has the parameters shown in Table 2.

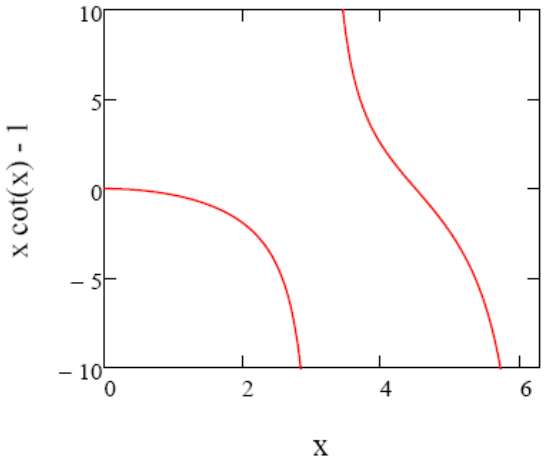


Figure 2.2: Sign of $\left|M_{langmuir}\right|-1$. The red solid curve is for $y(x)=x\cot(x)$. The plot shows the sign changes at $x=\pi$, i.e. $\omega_0\tau=2\pi$.

| | |
|---|---|
| $\varepsilon_{nx}, \varepsilon_{ny}$ | 15 $\pi$ mm.mrad. |
| $\beta_x, \beta_y$ | 60 meter |
| $N_i$ (Particles per bunch) | $10^9$ |
| $l_i$ (rms Bunch length) | 0.37 meter |
| $\gamma$ (Beam energy) | 100 |
| $\sigma_x, \sigma_y$ (Ion beam size) | 1.2 mm |
| $n_i$ (Ion beam density in beam frame) | $7.697\times10^{11}\, meter^{-3}$ |
| $\tau$ (Cooling section flight time in beam frame ) | $2\times10^{-9}$ s |

Table 2.1: RHIC gold ion beam parameters in the cooling section. For simplicity, a round beam approximation is used in the calculation. The emittance refers to 95% emittance.

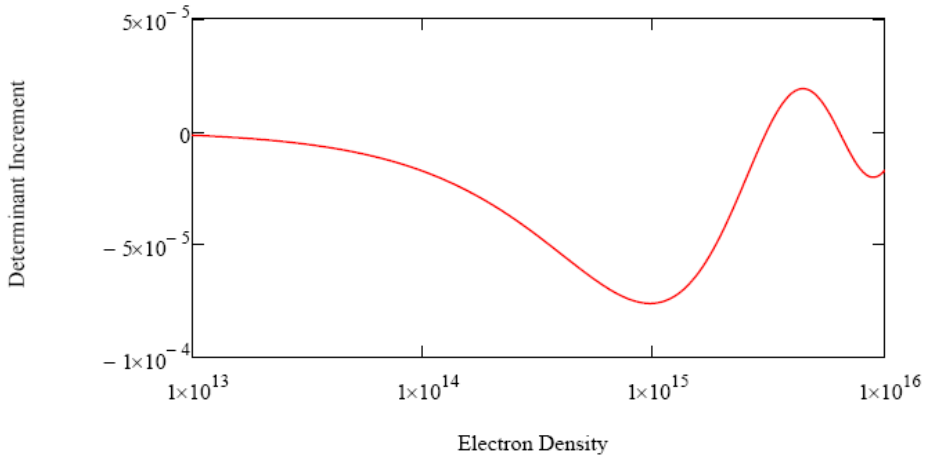


Figure 2.3: $\left|M_{langmuir}\right|-1$ dependence of the electron beam density. The abscissa is the electron density in unit of $m^{-3}$ and the ordinate is $\left|M_{Langmuir}\right|-1$.

| | |
|---|---|
| $Q_e$ (Electron charge per bunch) | 20 nC |
| $N_e$ (Electron number per bunch) | $1.25\times10^{11}$ |
| $\sigma_e$ (Electron rms beam size) | $1.225\times10^{-3}m$ |

Table 2.2 Electron beam parameters for the current electron cooler design.

Thus, the density limitation corresponds to a bunch length limitation of the electron beam,

$$l_e \geq \frac{N_e}{\pi\sigma_e^2 n_{e,th}\gamma} = 8.02\times10^{-3}m.$$

There are other limitations on the electron beam bunch length set by the requirement of optimizing the cooling force. For example if the electron bunch is shorter than 18 cm, Debye screening starts to reduce the cooling force. Since the electron beam bunch length is already 2 cm at the exit of the gun and stretchers have been designed to stretch the beam for higher cooling rate, this coherent longitudinal instability does not affect the current RHIC magnetized electron cooler design.

Although $\left|M_{Langmuir}\right| \leq 1$ is necessary condition for the ion beam to be stable, it may not be sufficient. In order to make the oscillation stable, any linear combination of the velocity and displacement of the local electrostatic oscillation has to be bounded. In other words, the eigenvalues of the transfer matrix has to be smaller or equal to 1 as well. The two eigenvalues of the transfer matrix (2.16) can be calculated from the following equations,

$$\lambda_{\pm} = 1 + \xi\left(\cos(\omega_0\tau) - 1\right) \pm \sqrt{\xi \sin(\omega_0\tau)\left[\omega_0\tau(\xi - 1) - \xi\sin(\omega_0\tau)\right]}\,. \tag{2.20}$$

For RHIC parameters, as we have seen above, $\xi << 1$ and equation (2.20) can be rewritten to

$$\lambda_{+} - 1 = \sqrt{-\xi\omega_0\tau\sin(\omega_0\tau)} + O(\xi)\,. \tag{2.21}$$

Therefore, the condition for $\left|\lambda_{+} - 1\right| \le 1$ is $\sin(\omega_0\tau) \ge 0$ or

$$\omega_0\tau = \pi\,, \tag{2.22}$$

which correspond to the following electron beam bunch length

$$l_e = \frac{N_e}{\pi\sigma_e^2 n_{e,th}\gamma} = 3.26\times10^{-2} m\,.$$

Outside the cooling section, the ion beam Plasma oscillation will be described by the following equation,

$$\frac{d^2 s_i}{dt^2} + \omega_{pi}^2 s_i = 0\,. \tag{2.23}$$

The corresponding transfer matrix is

$$M_{rest} = \begin{pmatrix} \cos(\omega_{pi}\tau_{rest}) & \dfrac{\sin(\omega_{pi}\tau_{rest})}{\omega_{pi}} \\ -\omega_{pi}\sin(\omega_{pi}\tau_{rest}) & \cos(\omega_{pi}\tau_{rest}) \end{pmatrix}, \tag{2.24}$$

where

$$\tau_{rest} = \frac{C_{RHIC} - l_{cool}}{\gamma c} = 1.269\times10^{-7} \tag{2.25}$$

is the flight time outside the electron cooling section and $C_{RHIC} = 3833.845m$ is the circumference of RHIC. Thus the one turn transfer matrix for the longitudinal plasma oscillation is

$$M_{ring} = M_{Langmuir} M_{rest} . \tag{2.26}$$

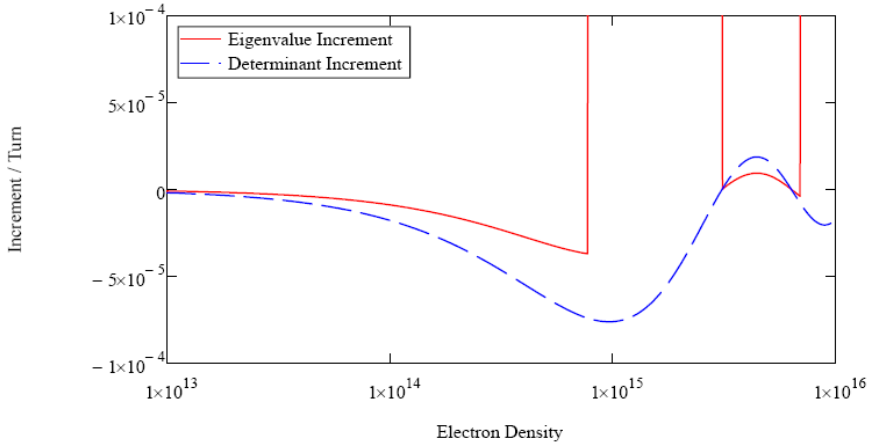


Figure 2.4 Plots of the eigenvalues and the determinant of the transfer matrix. The abscissa is the electron density in units of $m^{-3}$. The red solid curve is $|\lambda_+|-1$ and the blue dash curve is $|M_{langmuir}|-1$as already shown in the Fig.3. The maximal value of $|\lambda_+|-1$is around 0.01, which is much larger than the maximum of $|M_{langmuir}|$, and the threshold happens at $\omega_0 \tau = \pi$, i.e. $n_e = 3.1\times10^{15} m^{-3}$.

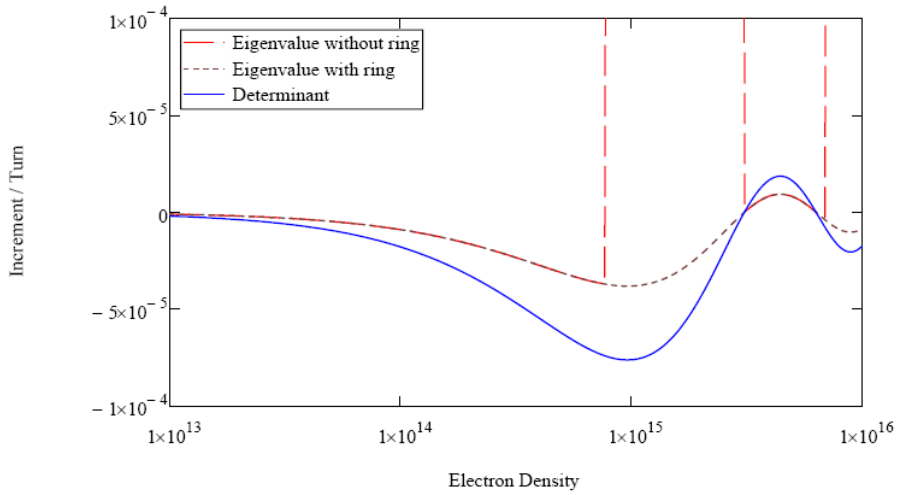


Figure 2.5 Comparison of the determinant and eigenvalues of $M_{ring}$ and $M_{Langmuir}$. The red dash line is the eigenvalue of $M_{Langmuir}$. The blue solid and brown dot curves are the determinant and eigenvalue of $M_{ring}$ respectively. The abscissa is the commoving frame electron density in units of $m^{-3}$.

As shown in Fig.2.4, including the rest of the ring does not affect the determinant of the one turn transfer matrix but the maximal eigenvalue does change. As a result, the eigenvalue and the determinant set the same limitation to the electron beam density, which for the current magnetized electron cooler design is

$$l_e \geq \frac{N_e}{\pi \sigma_e^2 n_{e,th} \gamma} = 8.02 \times 10^{-3} m .$$

The synchrotron tune of RHIC is $3.7 \times 10^{-4}$ which is 5 times faster than the maximal growth rate, $6.6 \times 10^{-5}$ per turn. So the oscillation could be distorted by the synchrotron motion before it is actually built up.

## *2.2 Transverse-Transverse Coupling*

When the beam enters the cooling section and merges with the cooling electron beam, a misalignment perturbation of the two beams can cause their centroids to perform transversal oscillation as shown in Fig.6. In order to obtain the equation of motion for the beam centroids, let's consider the electrostatic field within the beams in the commoving frame. As mentioned in section 2, in commoving frame, the beams have the geometry as the following,

$$l_e' = l_e \gamma = 0.18 \times 100 = 18m >> \sigma_e = 0.002m , \tag{2.27}$$

$$l_i' = l_i \gamma = 0.3 \times 100 = 30m >> \sigma_i = 0.0014m . \tag{2.28}$$

As shown in Fig.6 (b), the coordinates relations among the beam centroids frame and the commoving frame is

$$\vec{r} = \vec{R}_e + \vec{r}_e' = \vec{R}_i + \vec{r}_i', \tag{2.29}$$

where,

$$\vec{R}_e = \int \vec{r}_e f_e(x,y,z,t)dxdy \qquad \text{(integrate over electron beam cross section)} \tag{2.30}$$

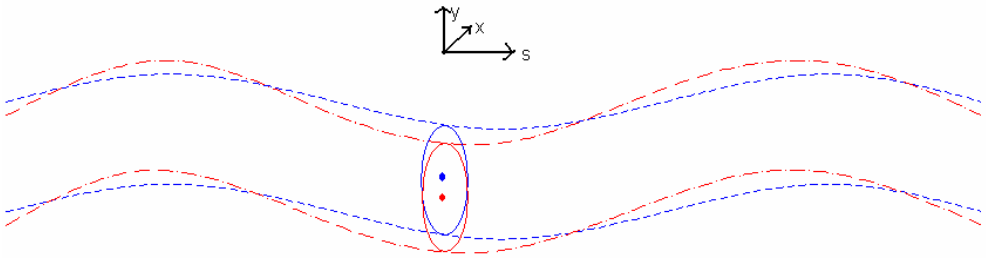


(a)

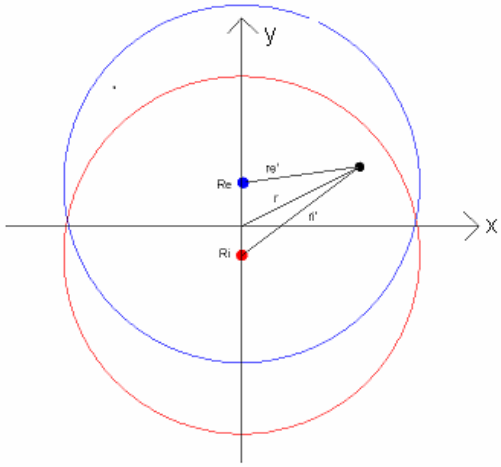


(b)

Figure 2.6 Illustration of Transversal Coupling in the cooling section. (a) The red dash curve represents for the ion beam and the blue dash-dot curve represents for the electron beam. The two circles represent the cross-section of the two beam and the solid spots are their centroids. (b) The cross sections of the beams shows the coordinates relations, where similar with (a), the solid spots are the beam centroids and $\vec{R}_e, \vec{R}_i$ are their coordinates.

$$\vec{R}_i = \int \vec{r}_i f_e(x,y,z,t)dxdy \qquad \text{(integrate over ion beam cross section).} \qquad (2.31)$$

Equation (2.27) and (2.28) show that infinite long beam approximation could be used to calculate the transverse electric field. If the oscillation amplitude is smaller than the beam size, the electric field within the overlapping part of the two beams is

$$\vec{E}_\perp(\vec{r},t) = \frac{-en_e\vec{r}_e'}{2\varepsilon_0} + \frac{Z_i en_i\vec{r}_i'}{2\varepsilon_0}. \qquad (2.32)$$

Thus in the rest frame, for an ion/electron sitting in position $\vec{r}$ and in time t, the transversal electrostatic force it sees is

$$\vec{F}_\perp^e(\vec{r},t) = \frac{e^2 n_e\vec{r}_e'}{2\varepsilon_0} - \frac{Z_i e^2 n_i\vec{r}_i'}{2\varepsilon_0}, \qquad \text{(for an electron in } (\vec{r},t)) \qquad (2.33)$$

$$\vec{F}_\perp^i(\vec{r},t) = -\frac{Z_i e^2 n_e\vec{r}_e'}{2\varepsilon_0} + \frac{Z_i^2 e^2 n_i\vec{r}_i'}{2\varepsilon_0}. \qquad \text{(for an ion in } (\vec{r},t)) \qquad (2.34)$$

And its equation of motion is

$$\frac{d^2}{dt^2}\vec{r}_e' = \omega_{pe}^2\vec{r}_e' - \omega_{ei}^2(\vec{r}_e - \vec{R}_i), \qquad \text{(for an electron in } (\vec{r}_e,t)) \qquad (2.35)$$

$$\frac{d^2}{dt^2}\vec{r}_i = -\omega_{ie}^2(\vec{r}_i - \vec{R}_e) + \omega_{pi}^2\vec{r}_i'. \qquad \text{(for an ion in } (\vec{r}_i,t)) \qquad (2.36)$$

Assuming the beam distribution function changes slowly with time and by integrating equation (3.9) and (3.10) over the cross section according to the beam distribution, the centroids' equations of motion can be obtained as following,

$$\frac{d^2}{dt^2}\vec{R}_e(z,t) + \omega_{ei}^2\vec{R}_e(z,t) = \omega_{ei}^2\vec{R}_i(z,t), \qquad (2.37)$$

$$\frac{d^2}{dt^2}\vec{R}_i(z,t) + \omega_{ie}^2\vec{R}_i(z,t) = \omega_{ie}^2\vec{R}_e(z,t). \qquad (2.38)$$

The transversal commoving frame plasma frequencies, $\omega_{pi}, \omega_{pe}, \omega_{ie}, \omega_{ei}$ are defined as

$$\omega_{pe} = \sqrt{\frac{n_e e^2}{2m_e \varepsilon_0}}, \qquad \omega_{pi} = \sqrt{\frac{Z_i^2 n_i e^2}{2M_i \varepsilon_0}},$$

$$\omega_{ie} = \sqrt{\frac{Z_i n_e e^2}{2M_i \varepsilon_0}}, \qquad \omega_{ei} = \sqrt{\frac{Z_i n_i e^2}{2m_e \varepsilon_0}}.$$

Comparing with equation (2.4) and (2.5), the only difference is the coefficients of the second terms at the left hand side both for ion and electron beam. So the steps for solving (2.37) and (2.38) are similar with what has been done in section 2.1. By setting the initial condition,

$$\vec{R}_e(z,0) = \frac{d}{dt}\vec{R}_e(z,0) = 0,$$

one gets

$$\frac{d^2}{dt^2}\vec{R}_i(z,t) = -\omega_{ie}^2\left[\vec{R}_i(z,0)\cos(\omega_0 t) + \frac{1}{\omega_0}\dot{\vec{R}}_i(z,0)\sin(\omega_0 t)\right], \tag{2.40}$$

where $\omega_0$ is now defined as $\omega_0 = \sqrt{\omega_{ie}^2 + \omega_{ei}^2}$. Integrating equation (3.17) from the front end of the cooling section $t = 0$, one obtains

$$\frac{d}{dt}\vec{R}_i(z,t) = -\xi\omega_0 \sin(\omega_0 t)\vec{R}_i(z,0) + \left[1 + \xi(\cos(\omega_0 t) - 1)\right]\dot{\vec{R}}_i(z,0), \tag{2.41}$$

$$\vec{R}_i(z,\tau) = \left[1 + \xi(\cos(\omega_0 \tau) - 1)\right]\vec{R}_i(z,0) + \frac{1}{\omega_0}\left[\omega_0\tau(1-\xi) + \xi\sin(\omega_0\tau)\right]\dot{\vec{R}}_i(z,0), \tag{2.42}$$

where $\xi$ is now defined as $\xi = \frac{\omega_{ie}^2}{\omega_0^2}$. Thus the transfer matrix of two stream dipole type transversal interaction for the ion beam centroid is

$$M_{transverse} = \begin{pmatrix} \xi(\cos(\omega_0\tau) - 1) + 1 & \frac{1}{\omega_0}\left[\xi\sin(\omega_0\tau) + (1-\xi)\omega_0\tau\right] \\ -\xi\omega_0\sin(\omega_0\tau) & \xi(\cos(\omega_0\tau) - 1) + 1 \end{pmatrix}, \tag{2.43}$$

which has exactly the same form of the transfer matrix due to the longitudinal Langmuir oscillation as shown in equation (2.16) except that the $\xi$ and $\omega_0$ are defined differently from section 2.1. Thus for each turn passing through the cooling section, the transversal centroid motion is effected by the electron beam according to the following expression,

$$\begin{pmatrix} R_i \\ \dot{R}_i \end{pmatrix}_\tau = M_{transverse} \begin{pmatrix} R_i \\ \dot{R}_i \end{pmatrix}_0 .$$

The calculation of $|M_{transverse}|$ is the same as in equation (2.17) and (2.18)

$$|M_{transverse}| - 1 = \frac{4\omega_{ie}^2 \omega_{ei}^2}{\omega_0^4} \sin^2(\frac{\omega_0 \tau}{2}) \left[ \frac{\omega_0 \tau}{2} \cot(\frac{\omega_0 \tau}{2}) - 1 \right]. \tag{2.44}$$

As shown in Fig.2.7[2], since the oscillation frequency for the transverse oscillation , $\omega_0$ , is 5 orders smaller than the longitudinal Langmuir oscillation, the instability threshold is 5 orders larger than what the longitudinal oscillation has and thus is not likely to be a real limitation for the electron cooler design. The eigenvalues of $M_{transverse}$ is also the same as (2.20) with different definitions of $\xi$ and $\omega_0$.

$$\lambda_\pm = 1 + \xi(\cos(\omega_0 \tau) - 1) \pm \sqrt{\xi \sin(\omega_0 \tau)[\omega_0 \tau(\xi - 1) - \xi \sin(\omega_0 \tau)]} . \tag{2.45}$$

Comparing with the longitudinal oscillation, the instability threshold of the electron beam density is pretty much the same for the eigenvalue restriction and the determinant restriction as shown in Fig.8. To implement $M_{transverse}$ into the ring, one need to do the Lorentz transformation at the entrance and inverse Lorentz transformation at the end of the cooling section since $M_{transverse}$ is derived in the commoving frame. Furthermore, to avoid double counting the phase advance inside the cooling section, one may add

[2] All the Figures in this subsection are given for the commoving frame densities $n_i = 5.3 \times 10^{12} m^{-3}$ and $n_e = 3.3 \times 10^{15} m^{-3}$ . The more realistic calculation for non-magnetized electron cooling design with wiggler field will be given in subsetion 3.4.

negative drift matrix to compensate. As a result, the transfer matrix in lab frame is given by

$$M_{tranlab} = R_{twiss} L_{drift} L_{lorentz}^{-1} M_{transverse} L_{lorentz} L_{drift} ,$$

where

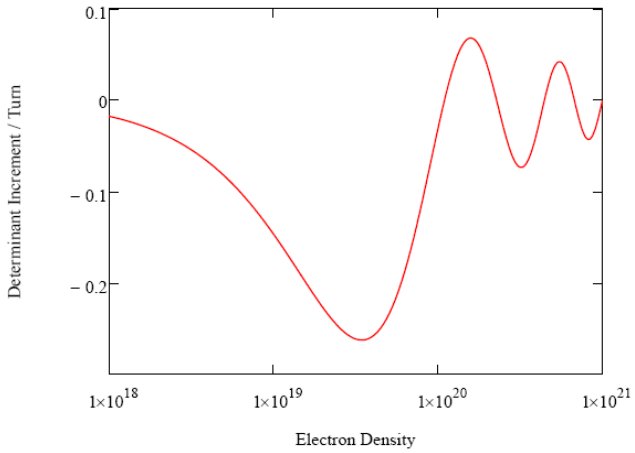


Figure 2.7 The dependence of $|M_{transverse}| - 1$ on the electron density $n_e$ shows a instability threshold 5 orders larger than the longitudinal Langmuir oscillation.

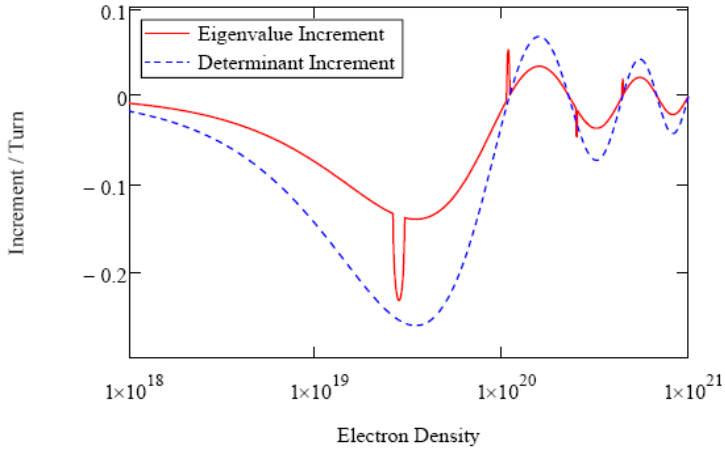


Figure 2.8 Plot of $|\lambda_+| - 1$ and $|M_{transverse}| - 1$ for the transverse dipole type oscillation. The abscissa is the electron density in units of $m^{-3}$. The red solid curve is $|\lambda_+| - 1$ and the blue dot curve is $|M_{transverse}| - 1$.

$$R_{twiss}=\begin{pmatrix}\cos(2\pi\nu_{x,y})+\alpha_{x,y}\cdot\sin(2\pi\nu_{x,y}) & \beta_{x,y}\sin(2\pi\nu_{x,y})\\ \dfrac{-(1+{\alpha_{x,y}}^{2})\sin(2\pi\nu_{x,y})}{\beta_{x,y}} & \cos(2\pi\nu_{x,y})-\alpha_{x,y}\cdot\sin(2\pi\nu_{x,y})\end{pmatrix},$$

$$L_{lorentz}=\begin{pmatrix}1 & 0\\ 0 & \gamma\end{pmatrix},\qquad L_{drift}=\begin{pmatrix}1 & -\dfrac{l_{cool}}{2}\\ 0 & 1\end{pmatrix},\qquad \alpha_{x,y}=-\frac{\beta_{x,y}'}{2}.$$

As shown in Fig.2.9, the threshold of the instability decreases about two orders of magnitude after including the cooling section into the ring.

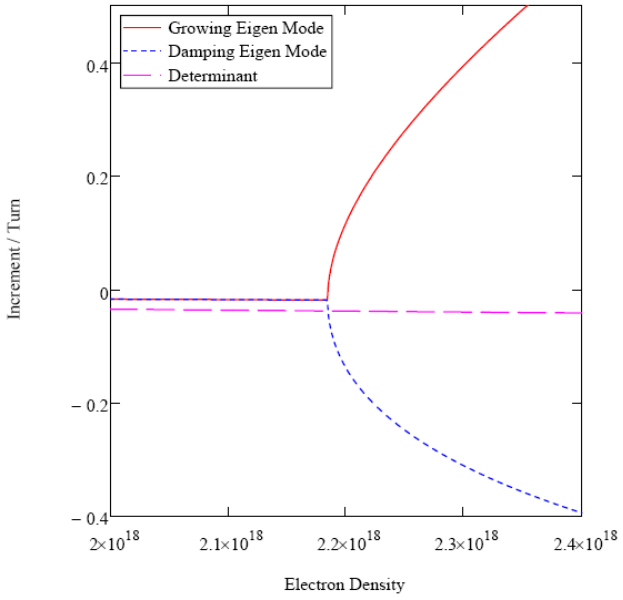


Figure 2.9 Plot of $|\lambda_{tranlab}|-1$ and $|M_{tranlab}|-1$ for the transverse dipole type oscillation. The abscissa is the electron density in units of $m^{-3}$ (in beam frame). The purple dash curve is $|M_{tranlab}|-1$. The blue dot curve and the red solid curves are the two eigen-values of $M_{tranlab}$, i.e. $|\lambda_{tranlab}|-1$. The tune has been taken as $\nu_x=28.23$ and the betatron function is taken as $\beta_x=40 meter$.

***APPENDIX A: Another Way To Derive Langmuir Equation***

The longitudinal continuous equations in the co-moving beam frame are

$$\frac{d}{dt}\lambda_{i,e} + \frac{d}{ds}\left(\lambda_{i,e} v_{i,e}\right) = 0\,, \tag{A.1}$$

where $\lambda_{i,e}$ is the line number density $v_{i,e}$ is the average longitudinal velocity. We consider the variation of a specific wavelength as the following

$$\lambda_{i,e}(s,t) = \overline{\lambda}_{i,e} + \widetilde{\lambda}_{i,e}(t)\exp(iks)\,, \tag{A.2}$$

where $\overline{\lambda}_{i,e}$ are the unperturbed line densities and $\widetilde{\lambda}_{i,e}(t)$ are the perturbation on top of the background. One can define parameters such that

$$v_{i,e} \equiv \frac{d}{dt}\xi_{i,e}\,, \tag{A.3}$$

$\xi_{i,e}$ are the longitudinal displacement of an infinitesimal thin slice of the beam plus a random constant. As we will see later, the random constant can be determined by the local line charge density variation. Inserting (A.2) into (A.1) and taking only the first order terms, one gets

$$\frac{d}{dt}\widetilde{\lambda}_{i,e}(s,t) + \overline{\lambda}_{i,e}\frac{d}{ds}v_{i,e} = 0\,. \tag{A.4}$$

From (A.2) and (A.4)

$$ik\widetilde{\lambda}_{i,e}(t)e^{iks} + \overline{\lambda}_{i,e}\frac{d^2}{ds^2}\xi_{i,e}(s,t) = g(s)\,. \tag{A.5}$$

In order to make (A.5) be satisfied for all s, the displacement and the integral constant must satisfy

$$\xi_{i,e}(s,t) = \xi_{i,e}(t)e^{iks}\,,$$

$$g(s) = g_0 e^{iks}\,.$$

Thus equation (A.5) can be written as

$$ik\tilde{\lambda}_{i,e}(t) - k^2\bar{\lambda}_{i,e}\xi_{i,e}(t) = g_0 . \tag{A.6}$$

The first term in equation (A.6) is proportional to the space charge force and the second term is proportional to the displacement. The random constant is chosen such that the force acted in the slice is zero when the displacements are zero, i.e. $g_0 = 0$. Thus we have

$$\tilde{\lambda}_{i,e}(s,t) = -ik\bar{\lambda}_{i,e}\xi_{i,e}(s,t). \tag{A.7}$$

The coherent acceleration due to the longitudinal space charge force is

$$\frac{d}{dt}v_{i,e} = -\left(\frac{Q_{i,e}g_0}{2\pi\varepsilon_0 m_{i,e}}\right)\left(Q_i\frac{d}{ds}\tilde{\lambda}_i + Q_e\frac{d}{ds}\tilde{\lambda}_e\right). \tag{A.8}$$

From equation (A.3), (A.7) and (A.8), one obtains

$$\frac{d^2}{dt^2}\xi_{i,e}(t) = -\frac{Q_{i,e}g_0k^2\bar{\lambda}_{i,e}}{2\pi\varepsilon_0 m_{i,e}}\left[Q_i\xi_i(t) + Q_e\xi_e(t)\right]. \tag{A.9}$$

The equations of motion for ion and electron displacements can be written down separately as

$$\frac{d^2}{dt^2}\xi_i = \omega_{ie}^2\xi_e - \omega_{pi}^2\xi_i , \tag{A.10}$$

$$\frac{d^2}{dt^2}\xi_e = \omega_{ei}^2\xi_i - \omega_{pe}^2\xi_e . \tag{A.11}$$

The plasma frequencies are defined as the following

$$\omega_{pe} = \sqrt{\frac{g_0(ka)^2 n_e e^2}{2m_e\varepsilon_0}} , \qquad \omega_{pi} = \sqrt{\frac{g_0(ka)^2 Z_i^2 n_i e^2}{2M_i\varepsilon_0}} ,$$

$$\omega_{ie} = \sqrt{\frac{g_0(ka)^2 Z_i n_e e^2}{2M_i\varepsilon_0}} , \qquad \omega_{ei} = \sqrt{\frac{g_0(ka)^2 Z_i n_i e^2}{2m_e\varepsilon_0}} .$$

The electric field induced by the two stream perturbations is

$$E_s = \frac{m_e}{e}\left(\omega_{pe}^2 \xi_e - \omega_{ei}^2 \xi_i\right). \tag{A.12}$$

From (A.10), (A.11) and (A.12), it is easy to show that the electric field is oscillating with frequency $\omega_0 = \sqrt{\omega_{pi}^2 + \omega_{pe}^2}$ and the solution can be directly integrating the following relation

$$\frac{d^2}{dt^2}\xi_{i,e}(t) = \frac{Q_{i,e}}{m_{i,e}}\hat{E}_s \cos(\omega_0 t + \varphi).$$

The solution of equation (A.10) and (A.11) can be expressed into the following transfer matrix

$$\begin{pmatrix} \xi_i \\ p_i \\ \xi_e \\ p_e \end{pmatrix}_t = \begin{pmatrix} 1+\Lambda_{pi}(\cos\psi - 1) & \Lambda_{pi}\sin\psi + (1-\Lambda_{pi})\psi & \Lambda_{ie}(1-\cos\psi) & \Lambda_{ie}(\psi - \sin\psi) \\ -\Lambda_{pi}\sin\psi & 1+\Lambda_{pi}(\cos\psi - 1) & \Lambda_{ie}\sin\psi & \Lambda_{ie}(1-\cos\psi) \\ \Lambda_{ei}(1-\cos\psi) & \Lambda_{ei}(\psi - \sin\psi) & 1+\Lambda_{pe}(\cos\psi - 1) & \Lambda_{pe}\sin\psi + (1-\Lambda_{pe})\psi \\ \Lambda_{ei}\sin\psi & \Lambda_{ei}(1-\cos\psi) & -\Lambda_{pe}\sin\psi & 1+\Lambda_{pe}(\cos\psi - 1) \end{pmatrix} \begin{pmatrix} \xi_i \\ p_i \\ \xi_e \\ p_e \end{pmatrix}_0, \tag{A.13}$$

where $\psi = \omega_0 t$, $\Lambda_{ei} = \frac{\omega_{ei}^2}{\omega_0^2}$, $\Lambda_{ie} = \frac{\omega_{ie}^2}{\omega_0^2}$ and $p_{i,e} = \frac{\dot{\xi}_{i,e}}{\omega_0}$.

# CHAPTER 3. TWO STREAM DIPOLE INSTABILITIES IN PRESENCE OF MAGNETIC FIELD

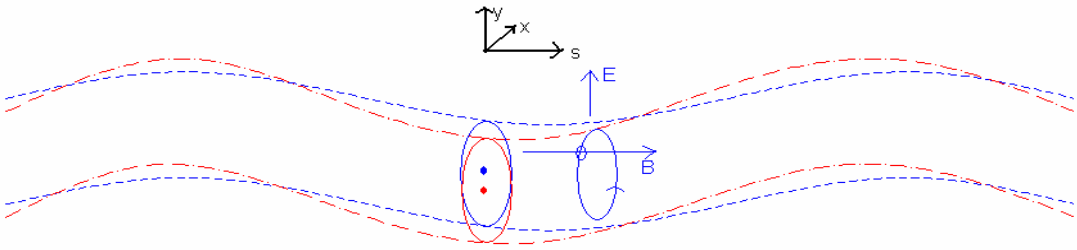


Figure 3.1 Transverse dipole oscillation in the cooling section with longitudinal magnetic field. The small blue circle crossed by the magnetic field line represents the electron Larmor oscillation orbit and the bigger circle going through it with an arrow represents the drift motion orbit.

## *3.1 Transversal Coupling in Presence of Solenoid Field*

For magnetized cooling, a solenoid with strong longitudinal magnetic field has to be included in the cooling section[6, 10]. For RHIC electron cooler, one option is to include a 30 meter long $B_{//} = 5T$ solenoid to enhance the cooling force. The Larmor frequencies in the beam commoving frame for the ions and electrons are

$$\omega_{ce} = \frac{eB_{//}}{m_e} = 8.79 \times 10^{11} s^{-1}, \tag{3.1}$$

$$\omega_{ci} = \frac{Z_i e B_{//}}{M_i} = 1.93 \times 10^8 s^{-1}. \tag{3.2}$$

Consequently, only the electrons are completely magnetized as the flight time is $10^{-9} s$. The equation of motion for each ion or electron is similar to (2.35) or (2.36) with an additional term coming from the magnetic force, i.e.

$$\frac{d^2}{dt^2}\vec{r}_e = \omega_{pe}^2(\vec{r}_e - \vec{R}_e) - \omega_{ei}^2(\vec{r}_e - \vec{R}_i) - \omega_{ce}(\frac{d}{dt}\vec{r}_e \times \hat{s}), \tag{3.3}$$

$$\frac{d^2}{dt^2}\vec{r}_i = -\omega_{ie}^2(\vec{r}_i - \vec{R}_e) + \omega_{pi}^2(\vec{r}_i - \vec{R}_i) + \omega_{ci}(\frac{d}{dt}\vec{r}_i \times \hat{s}), \tag{3.4}$$

where $\hat{s}$ is the unit vector along the longitudinal direction. Integrating (3.3) and (3.4) over the electron and ion beam transverse distribution respectively, one gets

$$\frac{d^2}{dt^2}\vec{R}_e + \omega_{ei}^2\vec{R}_e + \omega_{ce}(\frac{d}{dt}\vec{R}_e \times \hat{s}) = \omega_{ei}^2\vec{R}_i, \tag{3.5}$$

$$\frac{d^2}{dt^2}\vec{R}_i + \omega_{ie}^2\vec{R}_i - \omega_{ce}(\frac{d}{dt}\vec{R}_i \times \hat{s}) = \omega_{ie}^2\vec{R}_e. \tag{3.6}$$

With the following definition,

$$Z_e \equiv X_e + iY_e, \tag{3.7}$$

$$Z_i \equiv X_i + iY_i, \tag{3.8}$$

where X and Y are the transversal components of R, equation (3.5) and (3.6) can be rewritten as

$$\frac{d}{dt}\overline{Z_e} + i\Lambda\overline{Z_e} = i\Lambda Z_i, \tag{3.9}$$

$$\frac{d^2}{dt^2}Z_i + \omega_{ie}^2 Z_i + i\omega_{ci}\frac{d}{dt}Z_i = \omega_{ie}^2\overline{Z_e}, \tag{3.10}$$

where

$$\Lambda = \frac{\omega_{ei}^2}{\omega_{ce}} = 7.57 \times 10^5 s^{-1}, \tag{3.11}$$

$$\overline{Z_e} = \frac{1}{T_{ce}} \int_0^{T_{ce}} Z_e(t) dt .$$

Equation (3.9) and (3.10) describe the coupling of the ion beam centroid with the guiding center of the electron beam centroid. Taking the trial solutions as the following

$$Z_i(t) = a_i e^{-i\omega t}, \tag{3.12}$$

$$\overline{Z_e}(t) = a_e e^{-i\omega t}, \tag{3.13}$$

and inserting them into (3.9) and (3.10) respectively, one gets

$$\left(-i\omega + i\Lambda\right) a_e - i\Lambda a_i = 0, \tag{3.14}$$

$$\left(-\omega^2 + \omega_{ie}^2 + \omega_{ci}\omega\right) a_i - \omega_{ie}^2 a_e = 0. \tag{3.15}$$

Thus the eigenfrequencies are[3]

$$\omega_{1,2} = \frac{1}{2}\left[\left(\omega_{ci} + \Lambda\right) \pm \sqrt{\left(\omega_{ci} + \Lambda\right)^2 + 4\left(\omega_{ie}^2 - \Lambda\omega_{ci}\right)}\right], \tag{3.16}$$

$$\omega_3 = 0. \tag{3.17}$$

Thus, the solution of (3.9) and (3.10) should be the linear combination of three modes with the eigenfrequencies $\omega_0$, $\omega_1$ and $\omega_2$ respectively, i.e.

$$Z_i(t) = \sum_{\alpha=1}^{3} a_{i\alpha} e^{-i\omega_\alpha t}, \tag{3.18}$$

$$\overline{Z_e}(t) = \sum_{\alpha=1}^{3} a_{e\alpha} e^{-i\omega_\alpha t}. \tag{3.19}$$

From equation (3.15), one gets

[3] For $B_{//} = 5T$, $n_i = 7.697 \times 10^{11} m^{-3}$ and $n_e = 7.117 \times 10^{14} m^{-3}$, $\omega_+ = 1.946 \times 10^8 s^{-1}$ $\omega_- = -1.169 \times 10^6 s^{-1}$

$$a_{e\alpha} = \left(1 - \frac{\omega_\alpha^2}{\omega_{ie}^2} + \frac{\omega_{ci}\omega_\alpha}{\omega_{ie}^2}\right) a_{i\alpha} = T_\alpha a_{i\alpha}\,, \tag{3.20}$$

where

$$T_\alpha = \left(1 - \frac{\omega_\alpha^2}{\omega_{ie}^2} + \frac{\omega_{ci}\omega_\alpha}{\omega_{ie}^2}\right). \tag{3.21}$$

By using equation (3.20), equation (3.19) can be rewritten as

$$\overline{Z_e}(t) = \sum_{\alpha=1}^{3} T_\alpha a_{i\alpha} e^{-i\omega_\alpha t}\,. \tag{3.22}$$

Taking the derivative of (3.18) with respect to t, one gets

$$\frac{d}{dt} Z_i(t) = \sum_{\alpha=1}^{3} (-i\omega_\alpha) a_{i\alpha} e^{-i\omega_\alpha t}\,. \tag{3.23}$$

At $t = 0$, equation (3.18), (3.22) and (3.23) can be used to determine the coefficient $a_{i\alpha}$ and the solution for equation (3.9) and (3.10) can be obtained as,

$$\begin{pmatrix} Z_i(t) \\ \dot{Z}_i(t) \\ \overline{Z_e}(t) \end{pmatrix} = M \begin{pmatrix} Z_i(0) \\ \dot{Z}_i(0) \\ \overline{Z_e}(0) \end{pmatrix}, \tag{3.24}$$

where

$$M = \begin{pmatrix} e^{-i\omega_1 t} & e^{-i\omega_2 t} & 1 \\ -i\omega_1 e^{-i\omega_1 t} & -i\omega_2 e^{-i\omega_2 t} & 0 \\ T_1 e^{-i\omega_1 t} & T_2 e^{-i\omega_2 t} & 1 \end{pmatrix} \begin{pmatrix} 1 & 1 & 1 \\ -i\omega_1 & -i\omega_2 & 0 \\ T_1 & T_2 & 1 \end{pmatrix}^{-1}. \tag{3.25}$$

Equation (3.17) has been taken into account to get a simpler form of $M$ in (3.25). Setting the initial condition of the electron to be $\overline{Z_e}(0) = 0$, the solution for the ion beam centroid can be expressed as a $2 \times 2$ transfer matrix, i.e.

$$\begin{pmatrix} Z_i(t) \\ \dot{Z}_i(t) \end{pmatrix} = M_{ion} \begin{pmatrix} Z_i(0) \\ \dot{Z}_i(0) \end{pmatrix}, \tag{3.26}$$

where

$$M_{ion} = \begin{pmatrix} m_{11} & m_{12} \\ m_{21} & m_{22} \end{pmatrix}, \tag{3.27}$$

The matrix elements of $M_{ion}$ are listed in Appendix2, Equation (3.26) can be rewritten into a $4 \times 4$ matrix form in Frenet-Serret coordinate system as,

$$\begin{pmatrix} X_i(t) \\ X_i'(t) \\ Y_i(t) \\ Y_i'(t) \end{pmatrix} = T_{cool}^{'} \begin{pmatrix} X_i(0) \\ X_i'(0) \\ Y_i(0) \\ Y_i'(0) \end{pmatrix}, \tag{3.28}$$

where

$$T_{cool}^{'} = \begin{pmatrix} A_{11} & A_{12}V_{//} & -B_{11} & -B_{12}V_{//} \\ \dfrac{A_{21}}{V_{//}} & A_{22} & \dfrac{-B_{21}}{V_{//}} & -B_{22} \\ B_{11} & B_{12}V_{//} & A_{11} & A_{12}V_{//} \\ \dfrac{B_{21}}{V_{//}} & B_{22} & \dfrac{A_{21}}{V_{//}} & A_{22} \end{pmatrix}. \tag{3.29}$$

The matrix elements $A_{i,j}$ and $B_{i,j}$ are listed in the Appendix 2[4]. In order to obtain the one turn betatron oscillation transfer matrix, consider the ion beam transverse motion starting from the front end of the solenoid. As the beam going through the front end, it is affected by the fringe field and the effects can be represented by the transfer matrix[5]

$$E_C = \begin{pmatrix} 1 & 0 & 0 & 0 \\ 0 & 1 & \dfrac{iZ_i eB_{//}}{2M_i \gamma V_{//}} & 0 \\ 0 & 0 & 1 & 0 \\ -\dfrac{iZ_i eB_{//}}{2M_i \gamma V_{//}} & 0 & 0 & 1 \end{pmatrix}.$$

---

[4] For $B_{//} = 5T$, $\gamma = 100$, $n_i = 7.697 \times 10^{11} m^{-3}$, $n_e = 7.117 \times 10^{14} m^{-3}$ and 60 meter long cooling section, the transfer matrix $T_{cool}^{'}$ can be calculated as shown below,

$$T_{cool}^{'} = \begin{pmatrix} 1 & 0.585 & -6.376 \times 10^{-5} & 0.115 \\ -1.618 \times 10^{-3} & 0.926 & -3.172 \times 10^{-4} & 0.377 \\ 6.376 \times 10^{-5} & -0.115 & 1 & 0.585 \\ 3.172 \times 10^{-4} & -0.377 & -1.618 \times 10^{-3} & 0.926 \end{pmatrix}.$$

[5] Reader should not confused the charge number $Z_i$ in the following expression with the complex coordinates defined in (3.39)

Then the beam need to be transferred into commoving frame since $T_{cool}^{'}$ is derived in the commoving frame. The Lorenz transfer matrix for the transverse plane is given by

$$L_{lorentz} = \begin{pmatrix} 1 & 0 & 0 & 0 \\ 0 & \gamma & 0 & 0 \\ 0 & 0 & 1 & 0 \\ 0 & 0 & 0 & \gamma \end{pmatrix}.$$

Inside the solenoid, the ion beam sees the electron beams and the longitudinal magnetic field, whose effects to the ion beam centroid have been described by the transfer matrix $T_{cool}^{'}$ defined in (3.29). At the end of the solenoid, the beam has to be transformed back to the lab frame since the edge field effects and the Twiss matrix are all given in the lab frame. As the ion beam getting out the solenoid, it sees the fringe field again but in the opposite direction, whose effects are described by $E_C^{-1}$. Since the drift effects inside the solenoid has been considered in $T_{cool}^{'}$ already, the Twiss matrix should not include it again. However, when the beam optics code calculates the betatron tune of the accelerator with a cooling section, it automatically takes the cooling section drift into account and thus it is necessary to exclude the cooling section drift from the Twiss matrix. This exclusion can be done by inserting the drift transfer matrix for negative half solenoid length

$$L_{drift}\left(-\frac{L}{2}\right) = \begin{pmatrix} 1 & -\frac{L}{2} & 0 & 0 \\ 0 & 1 & 0 & 0 \\ 0 & 0 & 1 & -\frac{L}{2} \\ 0 & 0 & 0 & 1 \end{pmatrix},$$

on both sides of the Twiss matrix and thus keeping the symmetry of the accelerator. L is the length of the solenoid and for RHIC electron cooler $L = 60 meter$. The Twiss matrix for the whole ring without considering the electron-ion beam coupling is given by

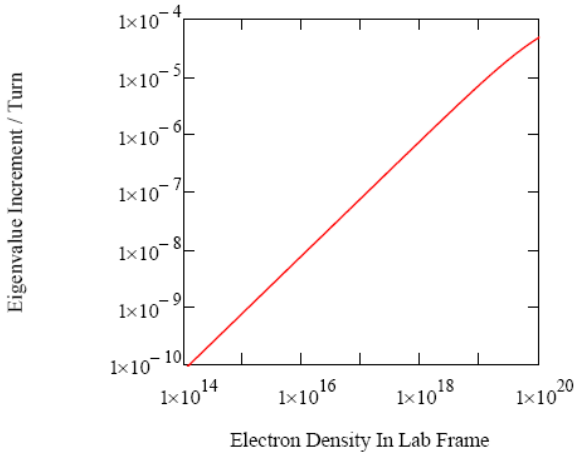


Figure 3.2 The dependence of the eigenvalue increment on the electron density for magnetized electron cooling. The abscissa is the electron density in Laboratory frame in unit of $m^{-3}$, and the ordinate is the maximum value of $|\lambda|-1$ as defined in equation (3.33)

$$R_{Twiss} = \begin{pmatrix} \cos(2\pi\nu_x) & \beta_x \sin(2\pi\nu_x) & 0 & 0 \\ -\dfrac{\sin(2\pi\nu_x)}{\beta_x} & \cos(2\pi\nu_x) & 0 & 0 \\ 0 & 0 & \cos(2\pi\nu_y) & \beta_y \sin(2\pi\nu_y) \\ 0 & 0 & -\dfrac{\sin(2\pi\nu_y)}{\beta_y} & \cos(2\pi\nu_y) \end{pmatrix},$$

where $\nu_x, \nu_y$ are the betatron tune including the cooling section drift and $\beta_x, \beta_y$ are the horizontal and vertical betatron functions at the back end of the cooling section. Thus, the one turn betatron oscillation transfer matrix is given by

$$T_{ring} = L_{drift} R_{Twiss} L_{drift} E_C{}^{-1} L_{lorentz}^{-1} T_{cool}^{'} L_{lorentz} E_C . \tag{3.30}$$

For RHIC, $\nu_x = 28.19$, $\nu_y = 29.18$ and $\beta_x = \beta_y = 60 meter$. The determinant of $T_{ring}$ for the current RHIC parameters is calculated to be[6]

$$\left|T_{ring}\right| - 1 = 7.02 \times 10^{-9}. \tag{3.31}$$

And the eigenvalues of $T_{ring}$ are

$$\lambda = \begin{pmatrix} 0.191 + 0.982i \\ 0.191 - 0.982i \\ 0.551 + 0.834i \\ 0.551 - 0.834i \end{pmatrix}. \tag{3.32}$$

The amplitudes of the eigenvalues is always slightly different from one and for the parameters listed above (3.31), they are

$$\left|\lambda\right| - 1 = \sqrt{\mathrm{Re}(\lambda)^2 + \mathrm{Im}(\lambda)^2} - 1 = \begin{pmatrix} -5.106 \times 10^{-8} \\ -5.106 \times 10^{-8} \\ 5.457 \times 10^{-8} \\ 5.457 \times 10^{-8} \end{pmatrix}. \tag{3.33}$$

The maximum eigenvalue amplitude is very close to the approximate analytical formula given by V. Parkhomchuk for short interaction time,

$$\Delta\lambda_{\max} = \sqrt{1 + \frac{1}{2}\frac{\beta_i \omega_{ie}^2 \Lambda \tau^2}{\gamma V_{//}}} - 1 = 5.476 \times 10^{-8}, \tag{3.34}$$

where $\Lambda$ is given in (3.11) and $\tau = \dfrac{l}{\gamma c}$ is the flight time in commoving frame. As shown in Fig. 3.2 and Fig. 3.3, for the considered ion beam and lattice parameters, the determinant

[6] For $B_{//} = 5T$, $\gamma = 100$, $n_i = 7.697 \times 10^{11} m^{-3}$, $n_e = 7.117 \times 10^{14} m^{-3}$ and 60 meter long solenoid, the transfer matrix $T_{ring}$ can be calculated as shown below,

$$T_{ring} = \begin{pmatrix} 0.789 & 67.748 & 0.155 & 13.271 \\ -1.544 \times 10^{-2} & -0.105 & -3.024 \times 10^{-3} & -2.052 \times 10^{-2} \\ -0.164 & -12.925 & 0.836 & 65.981 \\ 2.951 \times 10^{-3} & 7.24 \times 10^{-3} & -1.506 \times 10^{-2} & -3.696 \times 10^{-2} \end{pmatrix}.$$

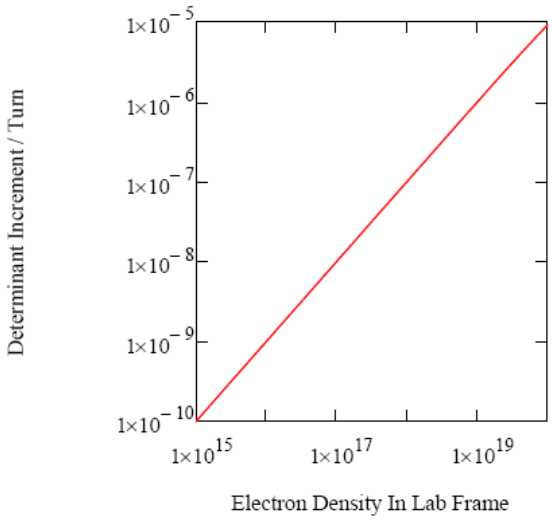


Figure 3.3 The dependence of the determinant on the electron density for magnetized electron cooling. The abscissa is the electron density in Laboratory frame in unit of $m^{-3}$. The ordinate is $|T_{ring}|-1$ as defined in equation (3.31).

of the transfer matrix and the maximum eigenvalue amplitude are always bigger than 1 which can cause the betatron oscillation amplitude increase from turn to turn. For the current parameters, the growth rate is

$$\Gamma = \frac{(|\lambda|_{\max} - 1)}{T_{rev}} = 4.3 \times 10^{-3} s^{-1}, \tag{3.35}$$

where $T_{rev}$ is the revolution frequency and $C_{rhic} = 3833.845 meter$ is the circumstance of RHIC. The growth time is thus

$$t_{rise} = \frac{1}{\Gamma} = 233 s\,. \tag{3.36}$$

Many facilities such as NAP-M, Fermi lab, Indiana, TARN II and COSY has observed the transverse coherent instability induced by the electron-ion coherent interaction and different methods have been applied against it. For the dipole instabilities, a feed back system is efficient to damp the transverse oscillation amplitude. In the Fermi

lab recycler, the instabilities stops after the machine have been decoupled for horizontal and vertical motions within the cooling section. For RHIC electron cooler, since there is no solenoid in the cooling section, this instability will not take place (Ref. Section 3.4).

## *3.2 Ion Clouds Effects to The Transverse Coherent Instability*

If the negative charge from the electron beam is bigger than the positive charge from the circulating ion beam, the ions produced from the residue gas can accumulate inside the cooling section unless the incoming beams make their motion unstable. Driven by the electron and ion beams, the accumulating ion clouds could oscillate and act back to the circulating beams. In section 3.3.1, the ion clouds motion inside a solenoid has been studied and stability condition has been shown for varies magnetic field strength. In section 3.3.2, the effects of ion clouds to the transverse coherent oscillation have been analyzed.

### 3.2.1 Ion Clouds Motion In The Cooling Section

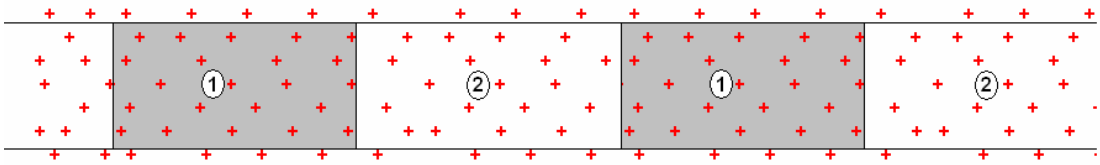


Figure 3.4 Illustration of the ion clouds inside the solenoid. The red '+' represents the ion cloud and the filled gray region marked '1' represents the incoming commoving electron and ion bunches and blank region '2' represents the space between two successive bunches.

For the first order approximation, assume the displacement of the beam centroid is small compared with the beam size and can be ignored for the moment. For simplicity, we also assume the electron bunch has the same bunch length with the ion bunch (This assumption will not make the result different from the real case since the ion motion will only depend on the total electron charge per bunch). The equation of motion for a single accumulated ion in region 1 (where the beams are present) is

$$\frac{d^2}{dt^2} z_{cl} + i\omega_{ccl} \frac{d}{dt} z_{cl} + (\omega_{cle}^2 - \omega_{cli}^2) z_{cl} = 0 , \tag{3.37}$$

where $z_{cl}$ describes single accumulated ion transverse position and defined as

$$z_{cl} \equiv x_{cl} + iy_{cl} . \tag{3.38}$$

Equation (3.37) is writing in the lab frame since the ion clouds longitudinal motion is slow. The Larmor frequency and the plasma frequencies are defined as[7]

$$\omega_{ccl} = \frac{Z_{cl} e B_{//}}{m_{cl}} = 4.82 \times 10^8 s^{-1} , \tag{3.39}$$

$$\omega_{cle} = \sqrt{\frac{Z_{cl} n_e e^2}{2\varepsilon_0 m_{cl}}} = 2.4 \times 10^8 s^{-1} , \tag{3.40}$$

[7] All the numbers given in this section are for $B_{//} = 5T$, $n_e = 6.63 \times 10^{16} m^{-3}$, $n_i = 5.30 \times 10^{14} m^{-3}$ and for hydrogen ion, i.e. $Z_{cl} = 1$, $m_{cl} = m_p$ (proton mass).

$$\omega_{cli} = \sqrt{\frac{Z_i Z_{cl} n_i e^2}{2\varepsilon_0 m_{cl}}} = 1.91\times 10^8 . \tag{3.41}$$

Setting the trial solution of (3.37) to be

$$z_{cl}(t) = a_{cl} e^{-i\omega t}, \tag{3.42}$$

and inserting (3.42) into (3.37), one get,

$$\omega^2 - \omega_{ccl}\omega - (\omega_{cle}^2 - \omega_{cli}^2) = 0 . \tag{3.43}$$

Thus, the eigenfrequencies are

$$\omega_{1,2} = \frac{1}{2}\left[\omega_{ccl} \pm \sqrt{\omega_{ccl}^2 + 4(\omega_{cle}^2 - \omega_{cli}^2)}\right] = \begin{cases} 1.01\times 10^9 s^{-1} \\ -5.33\times 10^8 s^{-1} \end{cases}. \tag{3.44}$$

There are two modes for the accumulated ion oscillation with frequency $\omega_1$ and $\omega_2$ respectively. So, (3.42) should be rewritten as the superposition of these two modes.

$$z_{cl}(t) = \sum_{\alpha=1}^{2} a_{cl,\alpha} e^{-i\omega_\alpha t} . \tag{3.45}$$

Set the initial condition at $t = 0$ to be

$$z_{cl} = z_{cl}(0), \tag{3.46}$$

$$\dot{z}_{cl} = \dot{z}_{cl}(0) . \tag{3.47}$$

From equation (3.45)-(3.47), one gets

$$\begin{pmatrix} z_{cl}(t) \\ \dot{z}_{cl}(t) \end{pmatrix} = M_{focus} \begin{pmatrix} z_{cl}(0) \\ \dot{z}_{cl}(0) \end{pmatrix}, \tag{3.48}$$

where $M_{focus}$ is the transfer matrix for the effects of the beams acting on the accumulating ion clouds and is defined as

$$M_{focus} = \frac{1}{\omega_1 - \omega_2}\begin{pmatrix} \omega_1 e^{-i\omega_2 t} - \omega_2 e^{-i\omega_1 t} & -i(e^{-i\omega_2 t} - e^{-i\omega_1 t}) \\ -i\omega_1\omega_2(e^{-i\omega_2 t} - e^{-i\omega_1 t}) & \omega_1 e^{-i\omega_1 t} - \omega_2 e^{-i\omega_2 t} \end{pmatrix}. \qquad (3.49)$$

In region 2 (the space between two successive bunches), ignoring self field interaction, the accumulated ions only see the longitudinal magnetic field and thus their equation of motion is

$$\frac{d^2}{dt^2} z_{cl} + i\omega_{ccl}\frac{d}{dt} z_{cl} = 0. \qquad (3.50)$$

Integrating equation (3.50), one gets

$$\frac{dz_{cl}(t)}{dt} = -i\omega_{ccl}\left[ z_{cl}(t) + i\frac{\dot{z}_{cl}(0)}{\omega_{ccl}} - z_{cl}(0) \right], \qquad (3.51)$$

and

$$z_{cl}(t) = i\frac{\dot{z}_{cl}(0)}{\omega_{ccl}} e^{-i\omega_{ccl} t} - i\frac{\dot{z}_{cl}(0)}{\omega_{ccl}} + z_{cl}(0). \qquad (3.52)$$

Taking the derivative of equation (3.52) with respect to $t$, the velocity of the accumulated ion is

$$\dot{z}_{cl}(t) = \dot{z}_{cl}(0) e^{-i\omega_{ccl} t}. \qquad (3.53)$$

From (3.52) and (3.53), the motion of the accumulated ion can be written into the following matrix form,

$$\begin{pmatrix} z_{cl}(t) \\ \dot{z}_{cl}(t) \end{pmatrix} = M_{Larmor}\begin{pmatrix} z_{cl}(0) \\ \dot{z}_{cl}(0) \end{pmatrix}, \qquad (3.54)$$

where $M_{lamour}$ is the transfer matrix for the Larmor oscillation when the accumulated ion sitting between two bunches and defined as

$$M_{Larmor} = \begin{pmatrix} 1 & i\dfrac{e^{-i\omega_{ccl} t} - 1}{\omega_{ccl}} \\ 0 & e^{-i\omega_{ccl} t} \end{pmatrix}. \qquad (3.55)$$

From equation (3.48) and (3.55), the transfer matrix for one whole bunch period (the time interval for two successive bunches passing by) is

$$\begin{aligned} M_{fl} &= M_{focus}(t_1) M_{Larmor}(t_2) \\ &= \begin{pmatrix} m_{11} & m_{12} \\ m_{21} & m_{22} \end{pmatrix} \end{aligned} \quad , \tag{3.56}$$

where $t_1$ and $t_2$ are the bunch length and the spacing between bunches respectively. The elements of $M_{fl}$ are defined in Appendix 2. The determinant of the transfer matrix is

$$\left| M_{fl} \right| = e^{-i(\omega_1 t_1 + \omega_2 t_1 + \omega_{ccl} t_2)} . \tag{3.57}$$

Matrix $M_{fl}$ can be rewritten into the complex form,

$$M_{fl} = A + iB . \tag{3.58}$$

The matrix elements of $A$ and $B$ are given in Appendix 2. Similar with what we did for equation (3.28), the $4 \times 4$ transfer matrix for the horizontal and vertical motion of the accumulated ions can be written as

$$\begin{pmatrix} X_{cl}(t) \\ \dot{X}_{cl}(t) \\ Y_{cl}(t) \\ \dot{Y}_{cl}(t) \end{pmatrix} = \begin{pmatrix} A_{11} & A_{12} & -B_{11} & -B_{12} \\ A_{21} & A_{22} & -B_{21} & -B_{22} \\ B_{11} & B_{12} & A_{11} & A_{12} \\ B_{21} & B_{22} & A_{21} & A_{22} \end{pmatrix} \begin{pmatrix} X_{cl}(0) \\ \dot{X}_{cl}(0) \\ Y_{cl}(0) \\ \dot{Y}_{cl}(0) \end{pmatrix} = T_{fl} \begin{pmatrix} X_{cl}(0) \\ \dot{X}_{cl}(0) \\ Y_{cl}(0) \\ \dot{Y}_{cl}(0) \end{pmatrix} . \tag{3.59}$$

Setting the initial condition for the ion cloud to be (1,0,0,0) and multiplying it by $T_{fl}$ for 20 meters bunch spacing, 0.3 meters bunch length with parameter given below (3.105), the orbit of the accumulated ion can be obtained as what shown in Fig. 3.5. As shown in Fig.14 the ion cloud motion is composed of two parts, the Larmor oscillation and the drift of the Larmor circle. In order to obtain the drift frequency, consider equation (3.101). It has the same form as (3.40) with zero $Z_i$ to the RHS. Following the procedures from

(3.42) to (3.48), the equation of motion for the Larmor circle guiding center can be derived as

$$\frac{d}{dt}\overline{z_{cl}} - \frac{i(\omega_{cle}^2 - \omega_{cli}^2)}{\omega_{ccl}}\overline{z_{cl}} = 0\,, \tag{3.60}$$

where $\overline{z_{cl}}$ describes the guiding center and is defined as

$$\overline{Z_{cl}} = \frac{1}{T_{ccl}}\int_0^{T_{ccl}} Z_{cl}(t)dt\,, \tag{3.61}$$

where $T_{ccl} = \dfrac{2\pi}{\omega_{ccl}}$ is the Larmor period. The solution of (3.60) for each bunch period $t_1 + t_2$ is

$$\overline{z_{cl}}(t_1) = \overline{z_{cl}}(0)e^{\frac{i(\omega_{cle}^2 - \omega_{cli}^2)}{\omega_{ccl}}t_1}\,, \tag{3.62}$$

where

$$t_1 = \frac{0.3}{c} = 10^{-9}s^{-1}. \tag{3.63}$$

From equation (3.39) to (3.41), one gets

$$\omega_{drift} = \frac{\omega_{cle}^2 - \omega_{cli}^2}{\omega_{ccl}} = 4.41\times10^7 s^{-1}\,. \tag{3.64}$$

The guiding center drift phase advance for each bunch period $t_1 + t_2$ is

$$\Delta\psi_{drift} = \omega_{drift}t_1 = 0.044 \text{ rad}\,. \tag{3.65}$$

For one period of guiding center drift oscillation, the number of bunches needed to pass by the ion cloud is

$$N = \frac{2\pi}{\Delta\psi_{drift}} \approx 142\,. \tag{3.66}$$

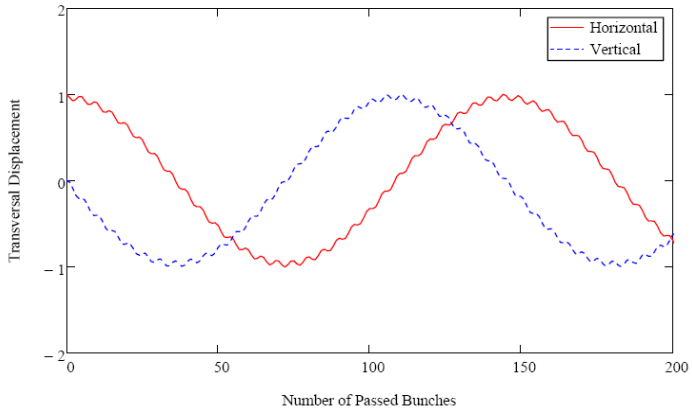


Figure 3.5 The orbit of the accumulated ion in the cooling section. The abscissa shows the number of bunches passing by and the ordinate shows the transverse position of the ion. The red solid curve is for the horizontal position and the blue dot curve is for the vertical position.

This result is consistent with the turn by turn data plotting shown in Fig.1. Since the drift motion only happens when the bunches passing by the cloud ($t_1$ out of one bunch period $t_1 + t_2$), the average angular drift frequency will be given by the inverse of the time needed for one drift oscillation multiplied by $2\pi$, i.e.

$$\Omega_{drift} = \frac{2\pi}{N(t_1 + t_2)} = 6.5 \times 10^5 s^{-1}, \tag{3.67}$$

where

$$t_1 + t_2 = 6.77 \times 10^{-8} s. \tag{3.68}$$

The stability condition for ion clouds motion is that the maximal amplitude of the eigenvalues of $T_{fl}$ must be equal or smaller than 1, i.e.

$$|\lambda_{\max}| = \sqrt{\mathrm{Re}(\lambda_{\max})^2 + \mathrm{Im}(\lambda_{\max})^2}. \tag{3.69}$$

Here we calculate the eigenvalues numerically and the results have been plotted in Fig. 3.6 and Fig. 3.7. As shown in Fig. 3.6, for a zero magnetic field, a gap of 180 ns is enough to clear the ion clouds out of the cooling section. However, as the magnetic field

increases, the stable region increases as well and when the magnetic field is around a few Tesla, it is not likely that the ion clouds can be cleared out by simply making a gap for the circulating beams. One more efficient way could be adjusting the strength of the magnetic field to the unstable region as shown in Fig. 3.7. For instance, when there is no magnetic field, bunch spacing of 20 meters will make the ion accumulate inside the cooling section but if a longitudinal magnetic field of 0.79-0.98 is applied, the ion clouds can be cleared out by the first resonance shown in Fig.3.7. It is also clear from Fig. 3.7, a bunch spacing of 60 meters can not clear out the ion clouds if the magnetic field sitting at any region where the maximal amplitude of the eigenvalues is one. Although the electrostatic force coming from the ion clouds itself has been ignored in the above discussion, it can be included into the equation of motion (3.37) and (3.50) easily as shown in the following,

$$\frac{d^2}{dt^2} z_{cl} + i\omega_{ccl} \frac{d}{dt} z_{cl} - \omega_{pcl}^2 z_{cl} = 0 , \tag{3.70}$$

$$\frac{d^2}{dt^2} z_{cl} + i\omega_{ccl} \frac{d}{dt} z_{cl} + (\omega_{cle}^2 - \omega_{cli}^2 - \omega_{pcl}^2) z_{cl} = 0 . \tag{3.71}$$

where

$$\omega_{pcl} = \sqrt{\frac{Z_{cl}^2 n_{cl} e^2}{2\varepsilon_0 m_{cl}}} . \tag{3.72}$$

The ion cloud density is usually expressed into the neutralization factor $\eta$ defined as the following,

$$\eta = \frac{n_{cl}}{n_e} . \tag{3.73}$$

So equation (3.72) can be rewritten as

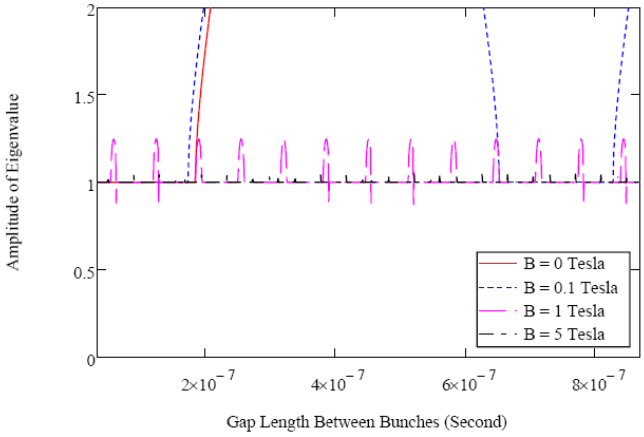


Figure 3.6 The dependence of the maximal amplitude of the eigenvalues on the bunch spacing for various of magnetic field. The abscissa is the spacing between two successive bunches in unit of second and the ordinate is the amplitude of the maximal eigenvalue. The interval between two successive resonances is approximately equal to the Lamoure oscillation period of the ion clouds. The bunch length is taken as 0.3 meters.

$$\omega_{pcl} = \sqrt{\frac{\eta Z_{cl}^2 n_e e^2}{2\varepsilon_0 m_{cl}}} = \sqrt{\eta Z_{cl}}\,\omega_{cle} \ . \tag{3.74}$$

The procedures to solve equation (3.70) and (3.71) are the same as what has been done for equation (3.37) and the transfer matrix for them are:

a). For region 1, i.e. (3.71), the transfer matrix has the same form as (3.49) except the eigenfrenquecies includes the ion clouds term now

$$M_{focus}(t_1) = \frac{1}{\omega_{f,1} - \omega_{f,2}} \begin{pmatrix} \omega_{f,1} e^{-i\omega_{f,2}t_1} - \omega_2 e^{-i\omega_{f,1}t_1} & -i(e^{-i\omega_{f,2}t_1} - e^{-i\omega_{f,1}t_1}) \\ -i\omega_1\omega_2(e^{-i\omega_2 t_1} - e^{-i\omega_{f,1}t_1}) & \omega_1 e^{-i\omega_{f,1}t_1} - \omega_2 e^{-i\omega_{f,2}t_1} \end{pmatrix}, \tag{3.75}$$

where,

$$\omega_{f1,2} = \frac{1}{2}\left[\omega_{ccl} \pm \sqrt{\omega_{ccl}^2 + 4(\omega_{cle}^2 - \omega_{cli}^2 - \omega_{clcl}^2)}\right]. \tag{3.76}$$

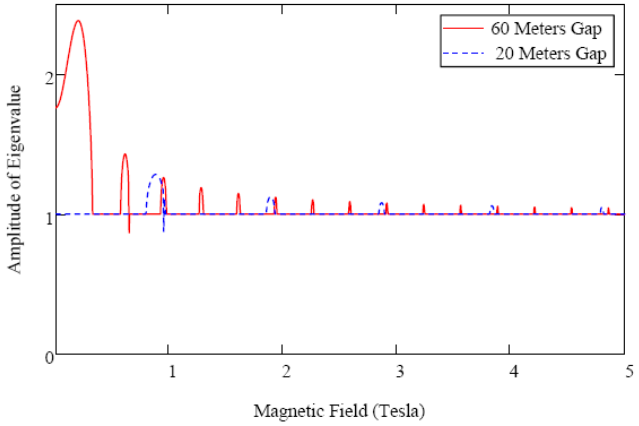


Figure 3.7. The dependence of the maximal amplitude of the eigenvalues on the field strength of the solenoid. The abscissa is the longitudinal magnetic field of the solenoid in unit of Tesla and the ordinate is the maximal amplitude of the eigenvalues. The red solid curve is for the bunch spacing equal to 60 meters (200 ns) and the blue dash curve is for the bunch spacing to be 20 meters (67 ns). The bunch length is taken as 0.3 meters.

b). For region 2, i.e. (3.70), the transfer matrix also has the similar form as (3.49) instead of (3.55) but with a different eigenfrequencies.

$$M_{defocus} = \frac{1}{\omega_{d,1} - \omega_{d,2}} \begin{pmatrix} \omega_{d,1} e^{-i\omega_{d,2}t} - \omega_{d,2} e^{-i\omega_{d,1}t} & -i(e^{-i\omega_{d,2}t} - e^{-i\omega_{d,1}t}) \\ -i\omega_{d,1}\omega_{d,2}(e^{-i\omega_{d,2}t} - e^{-i\omega_{d,1}t}) & \omega_{d,1} e^{-i\omega_{d,1}t} - \omega_2 e^{-i\omega_{d,2}t} \end{pmatrix}, \tag{3.77}$$

where

$$\omega_{d1,2} = \frac{1}{2}\left[\omega_{ccl} \pm \sqrt{\omega_{ccl}^2 - 4\omega_{clcl}^2}\right]. \tag{3.78}$$

Thus the transfer matrix for one bunch period is $M_{fd} = M_{focus} M_{defocus}$. The $4 \times 4$ transfer matrix can be obtained again as

$$T_{fd} = \begin{pmatrix} \mathrm{Re}(M_{fd}) & -\mathrm{Im}(M_{fd}) \\ \mathrm{Im}(M_{fd}) & \mathrm{Re}(M_{fd}) \end{pmatrix}. \tag{3.79}$$

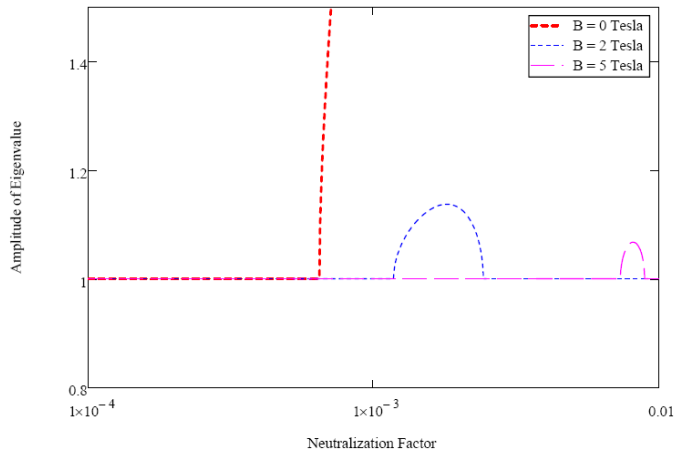


Figure 3.8 The dependence of the maximal amplitude of the eigenvalues on the neutralization factor $\eta$ for varies magnetic field. The abscissa is the neutralization factor and the ordinate is the maximal amplitude of the transfer matrix eigenvalus. The matrix is calculated from (3.79) with bunch length 0.3 meter and bunch spacing 20 meters (67ns).

By plotting the maximal eigenvalue amplitude of the transfer matrix $T_{fd}$ as the function of the neutralization factor $\eta$, a limit for the ion accumulation can be given for a stable ion motion. Above the limit, the defocusing effects from the ion cloud itself will stop further ion accumulation. As shown in Fig. 3.8, the limit is around $\eta = 0.0074$ for $B_{//} = 2T$ and $\eta = 0.0011$ for $B_{//} = 5T$.

### 3.2.2 Transverse Coherent Instability In Presence Of The Ion Cloud

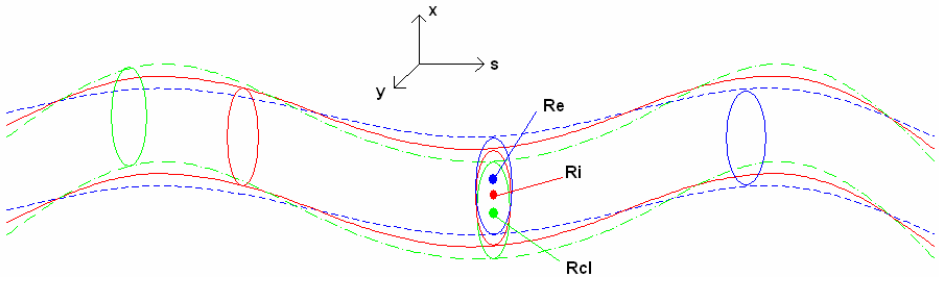


Figure 3.9. Illustration of the cooling section commoving beams and the ion cloud. The blue dash curve represents the electron beams, the red solid curve represents circulating ion beam and the green dot-dash curve represents the accumulated ion cloud from the residue gas ionization. The solid spots represents their centroids respectively according to the colors and the solid ellipses represent their cross section.

In section 3.1, the coherent two stream instability has been studied and a growth rate of $2.8\times10^{-7}$ per turn has been calculated due to the dipole mode centroid oscillation. One may ask what will happen to the two stream interaction in the cooling section if the ion cloud from the ionization of the residue gas is not completely cleared out. In this section, the effects of the ion cloud to the electron-ion beam long range transverse interaction will be studied.

Comparing with the situation for section 3.1, one more term due to the ion cloud has to be added into equation (3.3) and (3.4). Thus the equations of motion for a single circulating ion or a single electron in the lab frame are

$$\frac{d^2}{dt'^2}\vec{r}_e = \omega'^2_{pe}(\vec{r}_e-\vec{R}_e)-\omega'^2_{ei}(\vec{r}_e-\vec{R}_i)-\omega'_{ce}(\frac{d}{dt}\vec{r}_e\times\hat{s})-\omega'^2_{ecl}(\vec{r}_e-\vec{R}_{cl}), \tag{3.80}$$

$$\frac{d^2}{dt'^2}\vec{r}_i = -\omega'^2_{ie}(\vec{r}_i-\vec{R}_e)+\omega'^2_{pi}(\vec{r}_i-\vec{R}_i)+\omega'_{ci}(\frac{d}{dt}\vec{r}_i\times\hat{s})+\omega'^2_{icl}(\vec{r}_i-\vec{R}_{cl}), \tag{3.81}$$

where the subscribe ‘cl’ stands for ‘cloud’. For consistence with the previous chapter, we are going to use primed variables such as $t', \omega'$ for the quantities in lab frame and the non-primed variables such as $t, \omega$ for the quantities in the beam frame**.** The equation of motion for a trapped ion is

$$\frac{d^2}{dt'^2}\vec{r}_{cl} = -\omega'^2_{cle}(\vec{r}_{cl} - \vec{R}_e) + \omega'^2_{pcl}(\vec{r}_{cl} - \vec{R}_{cl}) + \omega'_{ccl}(\frac{d}{dt'}\vec{r}_{cl} \times \hat{s}) + \omega'^2_{cli}(\vec{r}_{cl} - \vec{R}_i) - \Gamma'\frac{d}{dt'}\vec{r}_{cl}\,,$$

(3.82)

where $\Gamma'$ can appear, for example, because of non-linearity of "external" electrical fields created by electrons and other kinds of ions. It can be considered as free parameter. Typically damping time is about 10-20 periods of the ion coherent perpendicular oscillations. Equation (3.80)-(3.82) are written in the lab frame and the plasma frequencies are defined as the following, (All the numbers here and later in this section are given for the lab frame densities $n'_i = 5.3\times10^{14} m^{-3}$, $n'_e = 3.3\times10^{17} m^{-3}$ and the hydrogen ion cloud, i.e. $Z_{cl} = 1$ and $m_{cl} = m_p$ )

$$\omega'_{pe} = \sqrt{\frac{n'_e e^2}{2m_e\varepsilon_0\gamma^3}} = 2.295\times10^7 s^{-1}, \qquad \omega'_{pi} = \sqrt{\frac{Z_i^2 n'_i e^2}{2M_i\varepsilon_0\gamma^3}} = 1.21\times10^5 s^{-1},$$

$$\omega'_{ie} = \sqrt{\frac{Z_i n'_e e^2}{2M_i\varepsilon_0\gamma^3}} = 3.4\times10^5 s^{-1}, \qquad \omega'_{ei} = \sqrt{\frac{Z_i n'_i e^2}{2m_e\varepsilon_0\gamma^3}} = 8.16\times10^6 s^{-1},$$

$$\omega'_{icl} = \sqrt{\frac{Z_i Z_{cl} n'_{cl} e^2}{2M_i\varepsilon_0\gamma}} = 3.4\sqrt{\eta}\times10^7 s^{-1}, \qquad \omega'_{ecl} = \sqrt{\frac{Z_{cl} n'_{cl} e^2}{2m_e\varepsilon_0\gamma}} = 2.295\sqrt{\eta}\times10^9 s^{-1},$$

$$\omega'_{cle} = \sqrt{\frac{Z_{cl} n'_e e^2}{2m_{cl}\varepsilon_0}} = 5.37\times10^8 s^{-1}\,, \qquad \omega'_{cli} = \sqrt{\frac{Z_i Z_{cl} n'_i e^2}{2m_{cl}\varepsilon_0}} = 1.91\times10^8 s^{-1}\,,$$

(3.83)

where

$$n'_e = \gamma n_e = 3.3\times10^{17}\, m^{-3},$$

$$n'_i = \gamma n_i = 5.3\times10^{14}\, m^{-3}.$$

The cyclotron frequencies are defined as

$$\omega'_{ccl} = \frac{Z_{cl} e B_{//}}{m_{cl}} = 4.82\times10^{8}\, s^{-1}, \tag{3.84}$$

$$\omega'_{ci} = \frac{Z_i e B_{//}}{m_i \gamma} = 1.93\times10^{6}\, s^{-1}, \tag{3.85}$$

$$\omega'_{ce} = \frac{e B_{//}}{m_e \gamma} = 8.79\times10^{9}\, s^{-1}. \tag{3.86}$$

Following the procedures from (3.3) to (3.10), the equations of motion for the beam centroids $R_i$, $R_e$ and the centroid of the ion cloud $R_{cl}$ can be derived as

$$\frac{d^2}{dt'^2} Z_i + i\omega'_{ci} \frac{d}{dt'} Z_i + \omega'^2_{ie} (Z_i - \overline{Z_e}) - \omega'^2_{icl} (Z_i - Z_{cl}) = 0, \tag{3.87}$$

$$\frac{d}{dt'} \overline{Z_e} + i\Lambda'_{ei} (\overline{Z_e} - Z_i) + i\Lambda'_{ecl} (\overline{Z_e} - Z_{cl}) = 0, \tag{3.88}$$

$$\frac{d^2}{dt'^2} Z_{cl} + i(\omega'_{ccl} - i\Gamma') \frac{d}{dt'} Z_{cl} + \omega'^2_{cle} (Z_{cl} - Z_e) - \omega'^2_{cli} (Z_{cl} - Z_i) = 0, \tag{3.89}$$

where

$$\Lambda'_{ei} = \frac{\omega'^2_{ei}}{\omega'_{ce}} = 7.57\times10^{3}\, s^{-1},$$

$$\Lambda'_{ecl} = \frac{\omega'^2_{ecl}}{\omega'_{ce}} = \eta \times 5.99\times10^{8}\, s^{-1}.$$

Set the ansatz to be

$$Z_{e,i,cl} = a_{e,i,cl} e^{-i(\omega' t' - k'_s s')}. \tag{3.90}$$

Equation (3.90) is written in the lab frame and the wave number is given by the periodic condition for the ion cloud,

$$k_s^{'} = \frac{n}{R}, \tag{3.91}$$

where $n$ is the harmonic number and $R$ is the radius of the ring. Inserting equation (3.90) into (3.89), one gets

$$-a_{cl}\omega'^2 + (\omega'_{ccl} - i\Gamma')\omega' a_{cl} + \omega'^2_{cle}(a_{cl} - a_e) - \omega'^2_{cli}(a_{cl} - a_i) = 0 \tag{3.92}$$

, which can be rewritten as

$$a_{cl} = T(\omega')(\omega'^2_{cle} a_e - \omega'^2_{cli} a_i), \tag{3.93}$$

where

$$T(\omega') = \frac{-1}{(\omega' - \Omega'_1)(\omega' - \Omega'_2)}, \tag{3.94}$$

and the resonant frequencies $\Omega'_{1,2}$ are defined as

$$\Omega'_{1,2} = -\frac{i}{2}\Gamma' + \frac{1}{2}\left[\omega'_{ccl} \pm \sqrt{(\omega'_{ccl} - i\Gamma')^2 + 4(\omega'^2_{cle} - \omega'^2_{cli})}\right]. \tag{3.95}$$

Inserting (3.90) into equation (3.87) and (3.88), one gets

$$(-\omega^2)a_i + \omega\omega'_{ci} a_i + \omega'^2_{ie}(a_i - a_e) - \omega'^2_{icl}(a_i - a_{cl}) = 0, \tag{3.96}$$

$$(-i\omega)a_e + i\Lambda'_{ei}(a_e - a_i) + i\Lambda'_{ecl}(a_e - a_{cl}) = 0, \tag{3.97}$$

where $\omega = \omega' - ck_s^{'}$. Inserting (3.93) into (3.96) and (3.97), one gets

$$\left[\omega^2 - \omega\omega'_{ci} + \omega'^2_{icl} - \omega'^2_{ie} + \omega'^2_{icl}\,\omega'^2_{cli}\,T(\omega')\right]a_i + \left[\omega'^2_{ie} - \omega'^2_{icl}\,\omega'^2_{cle}\,T(\omega')a_e\right]a_e = 0, \tag{3.98}$$

$$\left[\Lambda'_{ecl}\,T(\omega')\omega'^2_{cli} - \Lambda'_{ei}\right]a_i + \left[\Lambda'_{ecl} - \Lambda'_{ecl}\,T(\omega')\omega'^2_{cle} - \omega + \Lambda'_{ei}\right]a_e = 0. \tag{3.99}$$

For non-zero solution, the determinant of the coefficient matrix must be zero, which gives the dispersion equation that can be solved numerically for three eigenfrequencies

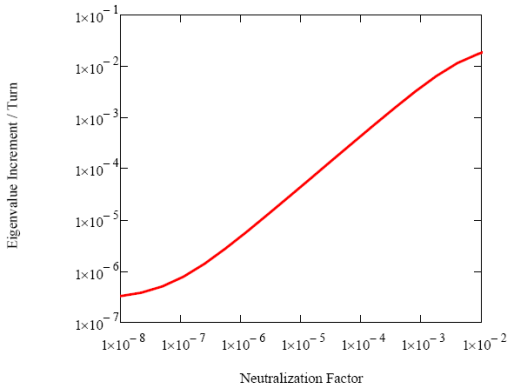


Figure 3.10. Plot of the eigenvalue increment as a function of the neutralization factor for $\Gamma' = 0.1 \times \mathrm{Re}(\Omega'_1)$ and parameters above (3.83), which shows the coherent instability strongly depends, on the neutralization factor.

and the solution of (3.87) and (3.88) can be written as

$$Z_i = \sum_{\alpha=1}^{3} a_{i,\alpha} e^{-i\omega_\alpha t'}, \tag{3.100}$$

$$\overline{Z}_e = \sum_{\alpha=1}^{3} a_{e,\alpha} e^{-i\omega_\alpha t'}. \tag{3.101}$$

For $\eta = 10^{-4}$ and $\Gamma' = 0.1 \times \mathrm{Re}(\Omega'_1)$, as an example, the eigenfrequencies are

$$\omega = \begin{cases} 1.9\times10^{6} - i3.6\times10^{4}\, s^{-1} \\ 6.4\times10^{4} - i2.3\times10^{5}\, s^{-1} \\ 7.6\times10^{3}\, s^{-1} \end{cases}. \tag{3.102}$$

Equation (3.100) and (3.101) has the same form as (3.18) and (3.19). Following the same procedures from (3.20) to (3.33), the increments of the eigenvalues can be calculated for certain ion cloud damping rate $\Gamma'$ and neutralization factor $\eta$. Fig.3.10 shows the calculation results of the instability increments for different neutralization level. From Fig. 3.8, the threshold of the neutralization lever for an unstable ion clouds transverse motion is about $7\times10^{-3}$, which corresponding an increment of $0.01$ per revolution. The

neutralization level is also limited by the vaccum quality and the geometry of the cooling section.

## *3.3 Coherent Instability in Presence of Wiggler Field*

In order to avoid particle loss due to the recombination in the cooling section, it is proposed that a transverse wiggler field should be applied to increase the relative velocity between the electron beam and the ion beam[11]. In this section, we take the wiggler field into account and study its effects to the transverse and longitudinal coherent instabilities. The formula have been applied to the designed non-magnetized electron cooling parameters of RHIC and instability thresholds have been calculated.

### 3.3.1 Transversal Dipole Coherent Instability

For the wiggler field, the magnetic field in the lab frame is

$$B_s = 0, \tag{3.103}$$

$$B_x = B_\perp \cos(\frac{2\pi s}{\lambda_w}), \tag{3.104}$$

$$B_y = B_\perp \sin(\frac{2\pi s}{\lambda_w}), \tag{3.105}$$

where $B_\perp, \lambda_w$ are the magnitude and the wavelength of the wiggler field respectively. Equation of motion for a single electron in cooling section with Wiggler field

$$\frac{d^2}{dt'^2}\vec{r}_e = \omega'^2_{pe}(\vec{r}_e - \vec{R}_e) - \omega'^2_{ei}(\vec{r}_e - \vec{R}_i) - \frac{e\beta c\vec{s} \times \vec{B}_\perp}{m_e\gamma}. \tag{3.106}$$

The centroids equations of motion in x plane are

$$\frac{d^2}{ds^2}X_e = -\Omega'^2_{ei}(X_e - X_i) + \frac{eB_\perp}{m_e\gamma c}\sin(\Omega'_w s), \tag{3.107}$$

$$\frac{d^2}{ds^2}X_i = -\Omega'^2_{ie}(X_i - X_e) - \frac{ZeB_\perp}{M_i\gamma c}\sin(\Omega'_w s), \tag{3.108}$$

where $\Omega'_{ie} = \frac{\omega'_{ie}}{c}$, $\Omega'_{ei} = \frac{\omega'_{ei}}{c}$ and $\Omega'_w = \frac{2\pi}{\lambda_w}$. Subtract (3.108) by (3.107),

$$\frac{d^2}{ds^2}X_{ie} + \Omega'^2_0 X_{ie} = \hat{f}\sin(\Omega'_w s), \tag{3.109}$$

where $\Omega'^2_0 = \Omega'^2_{ie} + \Omega'^2_{ei}$, $\hat{f} = -\frac{eB_\perp}{m_e\gamma c}\left(1 + \frac{Zm_e}{M_i}\right)$ and $X_{ie} = X_i - X_e$. Equation (3.109) is a forced hamornic oscillator and makes the trial solution to be

$$X_{ie} = A\sin(\Omega'_w s). \tag{3.110}$$

Inserting (3.110) into (3.109), one gets

$$A = \frac{\hat{f}}{\Omega'^2_0 - \Omega'^2_w}.$$

Thus one of the particular solutions of (3.109) is

$$X^p_{ie} = \frac{\hat{f}}{\Omega'^2_0 - \Omega'^2_w}\sin(\Omega'_w s).$$

The general solution of the homogenous equation of (3.109) is

$$X_{ie}^{g} = A(z)\cos(\Omega'_0 s + \varphi(z)).$$

Thus the overall solution of (3.109) is

$$X_{ie} = A(z)\cos(\Omega'_0 s + \varphi(z)) + \frac{\hat{f}}{\Omega'^2_0 - \Omega'^2_w}\sin(\Omega'_w s). \tag{3.111}$$

Set the initial condition to be $X_e(z,0) = \frac{d}{dt}X_e(z,0) = 0$. Thus the equation of motion for the ion center is

$$\begin{aligned}\frac{d^2}{ds^2}X_i = -\Omega'^2_{ie}\left[\cos(\Omega'_0 s)X_i(0) + \frac{\sin(\Omega'_0 s)}{\Omega'_0}(X'_i(z,0) - \frac{\hat{f}}{\Omega'^2_0 - \Omega'^2_w}\Omega'_w)\right] \\ -\left[\frac{\Omega'^2_{ie}}{\Omega'^2_0 - \Omega'^2_w}\hat{f} + \frac{ZeB_\perp}{M_i\gamma c}\right]\sin(\Omega'_w s)\end{aligned}. \tag{3.113}$$

Integrate equation (3.113), one gets

$$\begin{pmatrix} X_i \\ X'_i \\ 1 \end{pmatrix}_s = M_{transverse}\begin{pmatrix} X_i \\ X'_i \\ 1 \end{pmatrix}_0, \tag{3.114}$$

where

$$M_{transverse} = \begin{pmatrix} 1+\xi'(\cos(\Omega'_0 s)-1) & \frac{1}{\Omega'_0}\left[\Omega'_0 s(1-\xi') + \xi'\sin(\Omega'_0 s)\right] & a(s) \\ -\xi'\Omega'_0\sin(\Omega'_0 s) & 1+\xi'(\cos(\Omega'_0 s)-1) & a'(s) \\ 0 & 0 & 1 \end{pmatrix}, \tag{3.115}$$

$$a(s) = -\frac{\hat{f}\xi'\xi'_w}{1-\xi'_w}\frac{(\sin(\Omega'_0 s) - \Omega'_0 s)}{\Omega'_0\Omega'_w} - \left[\frac{\xi'}{1-\xi'_w}\hat{f} + \frac{ZeB_\perp}{M_i\gamma c}\right]\frac{(\sin(\Omega'_w s) - \Omega'_w s)}{\Omega'^2_w}, \tag{3.116}$$

$\xi'_w = \frac{\Omega'^2_w}{\Omega'^2_0}$ and $\xi' = \frac{\Omega'^2_{ie}}{\Omega'^2_0}$. The transfer matrix for the ring is

$$M_{ring} = R_x L_{drift} M_{transverse} L_{drift}, \tag{3.117}$$

| | |
|---|---|
| Wiggler field strength | $0.001\ T$ |
| Wiggler field wavelength | $0.15\,m$ |
| Cooling section length | $60\,m$ |
| Electron beam size | $2.36\ mm$ |
| Electron rms bunch length | $9\,mm$ |
| Electron beam charge | $5\,nC$ |
| Electron Density | $2.96\times10^{16}\ m^{-3}$ |
| Ion beam horizontal tune | 28.23 |
| Ion beam vertical tune | 29.23 |
| Ion beam charge | $12.64\ nC$ |
| Ion rms bunch length | $0.37\,m$ |
| Ion beam size | $2.36\ mm$ |
| Ion beam density | $2.31\times10^{13}\ m^{-3}$ |

Table 3.1. The parameters for the current non-magnetized electron cooler design.

where

$$R_x = \begin{pmatrix} \cos(2\pi\nu_x) & \beta_x \sin(2\pi\nu_x) & 0 \\ \frac{1}{\beta_x}\sin(2\pi\nu_x) & \cos(2\pi\nu_x) & 0 \\ 0 & 0 & 1 \end{pmatrix}, \tag{3.118}$$

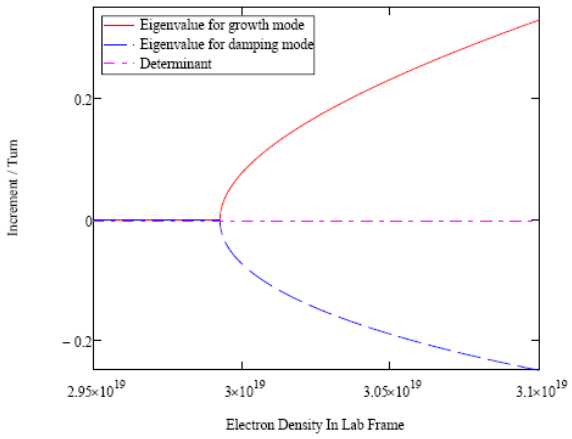


Figure 3.11 Increment of the determinant and the eigenvalues of the transversal transfer matrix for the ring in the nearby region of the transverse instability threshold. The abscissa is the electron density in the Laboratory frame in unit of $m^{-3}$.

$$L_{drift} = \begin{pmatrix} 1 & -\frac{L}{2} & 0 \\ 0 & 1 & 0 \\ 0 & 0 & 1 \end{pmatrix}. \tag{3.119}$$

For the parameters listed in table 3, the transfer matrix, its determinant increment and the eigenvalue increment for the ring are[8]

$$M_{ring} = \begin{pmatrix} 0.109 & 0.993 & 2.004\times10^{-7} \\ -0.995 & 0.107 & -1.562\times10^{-6} \\ 0 & 0 & 1 \end{pmatrix},$$

$$\left|\lambda_{transverse}\right| - 1 = -2.0\times10^{-6}, \tag{3.120}$$

$$\left|M_{transverse}\right| - 1 = -4.0\times10^{-6}. \tag{3.121}$$

[8] The plasma frequencies and the wiggler frequency for the parameters listed in Table 3.are
$\Omega'_{ie} = 3.41\times10^{-4}\,rad/m$ $\Omega'_{ei} = 5.68\times10^{-3}\,rad/m$ $\Omega'_{0} = 5.69\times10^{-3}\,rad/m$ $\Omega'_{w} = 41.89\,rad/m$ $\hat{f} = -0.0586\,m/m^2$
$\xi' = 3.58\times10^{-3}$ $\xi'_{w} = 5.43\times10^{7}$ $a(60) = 2.44\times10^{-6}\,m$ $a'(100) = 2.89\times10^{-8}\,m/m$

To obtain the threshold for the instability, the determinant and eigenvalue increment are plotted as a function of the electron beam density in Fig. 3.11, which is the same as the straight section case. Thus the threshold for transverse dipole instability is

$$n_e^{th} = 2.99 \times 10^{19} m^{-3}, \tag{3.122}$$

which is three orders of magnitude larger than the current electron density.

### 3.3.2 Longitudinal Dipole Coherent Instability

Since the wiggler field does not affect the longitudinal motion, the threshold for the instability due to Langmuir oscillation can still be determined from equation (2.19) and (2.22). As shown in Fig. 3.12, the threshold for the determinant less than one is reduced to

$$n_e^{thd} = 3.1 \times 10^{17} m^{-3}, \tag{3.123}$$

and for the eigenvalue less than one is reduced to

$$n_e^{th\lambda} = 7.7 \times 10^{16} m^{-3}. \tag{3.124}$$

After including the rest of the RHIC ring, the threshold from the eigenvalue is the same as what from the determinant limitation, which is shown in Fig. 2.5 and described in Section 2.1.2. Since the cooling section is much longer than the magnetized cooling design, the maximal growth rate is bigger than the synchrotron tune and the instability could happen before the synchrotron motion distorts the longitudinal plasma oscillation.

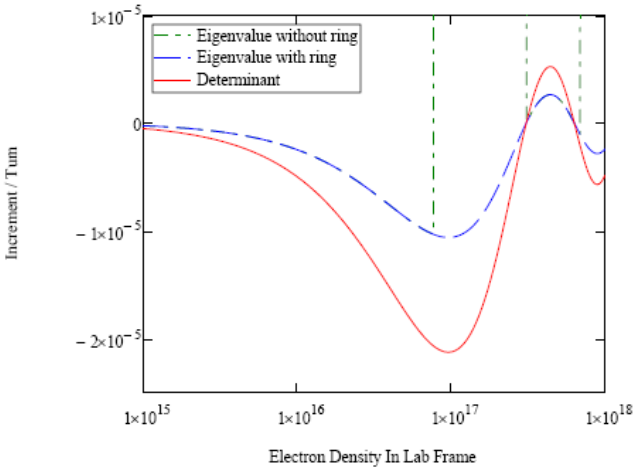


Figure 3.12 The increment of the determinant and the eigenvalue of the longitudinal transfer Matrix for parameters listed in table 3. The abscissa is the electron density in the Laboratory frame in units of $m^{-3}$. The green dash-dot curve shows the eigenvalue increment when the plasma oscillation outside the cooling section is ignored. The blue dash curve shows the result when oscillations outside the cooling section are included. The red solid curve represents the determinant increment.

The electron bunch length threshold can be estimated from equation (3.123) and Table 3 to be $l_e^{th} = 1.1cm$.

## *APPENDIX B: Equation of Motion for A Single Particle*

In this section, we get the solution for the ion beam centroid motion in the cooling section due to its interaction with electron beam. However it will be necessary to know the behavior of each single ion in the ion beam for the purpose of simulation. The equation of motion for single ion particle can be derived as the following. Consider equation (3.9)

$$\frac{d^2}{dt^2}\vec{r}_i = (\omega_{pi}^2 - \omega_{ie}^2)\vec{r}_i + \omega_{ie}^2\vec{R}_e - \omega_{pi}^2\vec{R}_i \,. \tag{B.1}$$

Since we already derived the solution for $\vec{R}_i$, we only need to find the behavior of the electron centroid to get a explicit form of the single ion equation of motion. From (3.13)

$$\vec{R}_i - \vec{R}_e = \vec{R}_i(z,0)\cos(\omega_0 t) + \frac{\sin(\omega_0 t)}{\omega_0}\dot{\vec{R}}_i(z,0) \,. \tag{B.2}$$

Thus, we get the solution for $\vec{R}_e$

$$\vec{R}_e = \vec{R}_i - \vec{R}_i(z,0)\cos(\omega_0 t) - \frac{\sin(\omega_0 t)}{\omega_0}\dot{\vec{R}}_i(z,0) \,. \tag{B.3}$$

Insert (B.3) into (B.1)

$$\frac{d^2}{dt^2}\vec{r}_i = (\omega_{pi}^2 - \omega_{ie}^2)\vec{r}_i + (\omega_{ie}^2 - \omega_{pi}^2)\vec{R}_i - \omega_{ie}^2\left[\vec{R}_i(z,0)\cos(\omega_0 t) + \frac{\sin(\omega_0 t)}{\omega_0}\dot{\vec{R}}_i(z,0)\right]. \tag{B.4}$$

Insert the definition of $\xi$ in equation (2.42) into (B.4)

$$\begin{aligned}\frac{d^2}{dt^2}\vec{r}_i - (\omega_{pi}^2 - \omega_{ie}^2)\vec{r}_i = \left(\xi(\omega_{ie}^2 - \omega_{pi}^2) - \omega_{ie}^2\right)\left[\frac{\dot{\vec{R}}_i(z,0)}{\omega_0}\sin(\omega_0 t) + \vec{R}_i(z,0)\cos(\omega_0 t)\right]. \\ + (1-\xi)(\omega_{ie}^2 - \omega_{pi}^2)\left[\dot{\vec{R}}_i(z,0)t + \vec{R}_i(z,0)\right]\end{aligned} \tag{B.5}$$

Thus, the single ion equation of motion inside the solenoid is like a driving oscillator

$$\frac{d^2}{dt^2}\vec{r}_i - (\omega_{pi}^2 - \omega_{ie}^2)\vec{r}_i = f(t) \,. \tag{B.6}$$

where $f(t)$ is the driving force and given by

$$f(t) = (\xi(\omega_{ie}^2 - \omega_{pi}^2) - \omega_{ie}^2)\left[\frac{\dot{\vec{R}}_i(z,0)}{\omega_0}\sin(\omega_0 t) + \vec{R}_i(z,0)\cos(\omega_0 t)\right] + (1-\xi)(\omega_{ie}^2 - \omega_{pi}^2)\left[\dot{\vec{R}}_i(z,0)t + \vec{R}_i(z,0)\right]. \tag{B.7}$$

Since for our case, $\xi$ is small,

$$f(t) \approx -\omega_{ie}^2 \left[ \frac{\dot{\vec{R}}_i(z,0)}{\omega_0} \sin(\omega_0 t) + \vec{R}_i(z,0)\cos(\omega_0 t) \right] + (\omega_{ie}^2 - \omega_{pi}^2)\left[\dot{\vec{R}}_i(z,0)t + \vec{R}_i(z,0)\right]. \quad \text{(B.8)}$$

In the presence of a solenoid, the single ion motion can be described by

$$\frac{d^2}{dt^2}\vec{r}_i = -\omega_{ie}^2(\vec{r}_i - \vec{R}_e) + \omega_{pi}^2(\vec{r}_i - \vec{R}_i) + \omega_{ci}(\frac{d}{dt}\vec{r}_i \times \hat{s}). \quad \text{(B.9)}$$

Write the above equation into the vertical and horizontal plane,

$$\frac{d^2}{dt^2}x_i = -\omega_{ie}^2(x_i - X_e) + \omega_{pi}^2(x_i - X_i) + \omega_{ci}\frac{d}{dt}y_i. \quad \text{(B.10)}$$

$$\frac{d^2}{dt^2}y_i = -\omega_{ie}^2(y_i - Y_e) + \omega_{pi}^2(y_i - Y_i) - \omega_{ci}\frac{d}{dt}x_i. \quad \text{(B.11)}$$

$(B.10) + i(B.11) \Rightarrow$

$$\frac{d^2}{dt^2}z_i = -\omega_{ie}^2(z_i - \overline{Z}_e) + \omega_{pi}^2(z_i - Z_i) - i\omega_{ci}\frac{d}{dt}z_i. \quad \text{(B.12)}$$

Here $z_i$ describes the single ion position and defined as

$$z_i = x_i + iy_i. \quad \text{(B.13)}$$

Equation (B.12) can be rewritten as

$$\frac{d^2}{dt^2}z_i + i\omega_{ci}\frac{d}{dt}z_i - (\omega_{pi}^2 - \omega_{ie}^2)z_i = \omega_{ie}^2\overline{Z}_e - \omega_{pi}^2 Z_i. \quad \text{(B.14)}$$

Since

$$Z_i(t) = m_{11}Z_i(0) + m_{12}\dot{Z}_i(0), \quad \text{(B.15)}$$

$$\overline{Z}_e(t) = m_{31}Z_i(0) + m_{32}\dot{Z}_i(0). \quad \text{(B.16)}$$

where $m_{11}, m_{12}$, $m_{31}$ and $m_{32}$ are defined in APPENDIX C (C.1)-(C.6). Thus the equation of motion for a single ion is

$$\frac{d^2}{dt^2} z_i + i\omega_{ci} \frac{d}{dt} z_i - (\omega_{pi}^2 - \omega_{ie}^2) z_i = f(t), \tag{B.17}$$

where the driving force $f(t)$ is defined as the following

$$f(t) = (\omega_{ie}^2 m_{31} - \omega_{pi}^2 m_{11}) Z_i(0) + (\omega_{ie}^2 m_{32} - \omega_{pi}^2 m_{12}) \dot{Z}_i(0). \tag{B.18}$$

We obtained the equation of motion of single ion and by numerically integrating the equation of motion, the beam behavior can be predicted.

## *APPENDIX C: Transverse Transfer Matrix Elements*

The matrix elements of the complex matrix $M_{ion}$ can be obtained from Equation (3.25) as the following,

$$m_{11} = \frac{\omega_2 \left(e^{-i\omega_1 t} - T_1\right) - \omega_1 \left(e^{-i\omega_2 t} - T_2\right)}{\omega_2 (1 - T_1) - \omega_1 (1 - T_2)}, \tag{C.1}$$

$$m_{12} = \frac{i(T_2 - 1)e^{-i\omega_1 t} - i(T_1 - 1)e^{-i\omega_2 t} + i(T_1 - T_2)}{\omega_2 (1 - T_1) - \omega_1 (1 - T_2)}, \tag{C.2}$$

$$m_{21} = \frac{i\omega_1 \omega_2 \left(e^{-i\omega_2 t} - e^{-i\omega_1 t}\right)}{\omega_2 (1 - T_1) - \omega_1 (1 - T_2)}, \tag{C.3}$$

$$m_{22} = \frac{\omega_2 e^{-i\omega_2 t} (1 - T_1) - \omega_1 e^{-i\omega_1 t} (1 - T_2)}{\omega_2 (1 - T_1) - \omega_1 (1 - T_2)}, \tag{C.4}$$

$$m_{31} = \frac{T_1 \omega_2 (e^{-i\omega_1 t} - 1) - T_2 \omega_1 (e^{-i\omega_2 t} - 1)}{\omega_2 (1 - T_1) - \omega_1 (1 - T_2)}, \tag{C.5}$$

$$m_{32} = \frac{iT_1(T_2 - 1)e^{-i\omega_1 t} - iT_2(T_1 - 1)e^{-i\omega_2 t} + i(T_1 - T_2)}{\omega_2 (1 - T_1) - \omega_1 (1 - T_2)}. \tag{C.6}$$

The matrix elements for the corresponding real and imaginary part of $M_{ion}$ $A_{i,j}$ and $B_{i,j}$ are

$$A_{11}=\frac{\omega_2\left(\cos(\omega_1 t)-T_1\right)-\omega_1\left(\cos(\omega_2 t)-T_2\right)}{\omega_2\left(1-T_1\right)-\omega_1\left(1-T_2\right)},\ A_{12}=\frac{\left(T_2-1\right)\sin(\omega_1 t)-\left(T_1-1\right)\sin(\omega_2 t)}{\omega_2\left(1-T_1\right)-\omega_1\left(1-T_2\right)},$$

$$A_{21}=\frac{\omega_1\omega_2\left(\sin(\omega_2 t)-\sin(\omega_1 t)\right)}{\omega_2\left(1-T_1\right)-\omega_1\left(1-T_2\right)},\qquad A_{22}=\frac{\omega_2\left(1-T_1\right)\cos(\omega_2 t)-\omega_1\left(1-T_2\right)\cos(\omega_1 t)}{\omega_2\left(1-T_1\right)-\omega_1\left(1-T_2\right)},$$

$$B_{11}=-\frac{\omega_2\left(\sin(\omega_1 t)-T_1\right)-\omega_1\left(\sin(\omega_2 t)-T_2\right)}{\omega_2\left(1-T_1\right)-\omega_1\left(1-T_2\right)},\quad B_{22}=\frac{\omega_1\left(1-T_2\right)\sin(\omega_1 t)-\omega_2\left(1-T_1\right)\sin(\omega_2 t)}{\omega_2\left(1-T_1\right)-\omega_1\left(1-T_2\right)},$$

$$B_{12}=\frac{\left(T_2-1\right)\cos(\omega_1 t)-\left(T_1-1\right)\cos(\omega_2 t)+\left(T_1-T_2\right)}{\omega_2\left(1-T_1\right)-\omega_1\left(1-T_2\right)},\ B_{21}=\frac{\omega_1\omega_2\left(\cos(\omega_2 t)-\cos(\omega_1 t)\right)}{\omega_2\left(1-T_1\right)-\omega_1\left(1-T_2\right)}.$$

The transfer matrix for the ion clouds motion within the solenoid, $M_{fl}$, has the following elements

$$m_{11}=\frac{\omega_1 e^{-i\omega_2 t_1}-\omega_2 e^{-i\omega_1 t_1}}{\omega_1-\omega_2},\qquad m_{21}=\frac{-i\omega_1\omega_2(e^{-i\omega_2 t_1}-e^{-i\omega_1 t_1})}{\omega_1-\omega_2},$$

$$m_{12}=\frac{1}{\omega_1-\omega_2}\left[i(\frac{\omega_1}{\omega_{ccl}}-1)e^{-i(\omega_2 t_1+\omega_{ccl}t_2)}-i(\frac{\omega_2}{\omega_{ccl}}-1)e^{-i(\omega_1 t_1+\omega_{ccl}t_2)}-i\frac{1}{\omega_{ccl}}(\omega_1 e^{-i\omega_2 t_1}-\omega_2 e^{-i\omega_1 t_1})\right],$$

$$m_{22}=\frac{1}{\omega_1-\omega_2}\left[\frac{\omega_2(\omega_1-\omega_{ccl})}{\omega_{ccl}}e^{-i(\omega_2 t_1+\omega_{ccl}t_2)}-\frac{\omega_1(\omega_2-\omega_{ccl})}{\omega_{ccl}}e^{-i(\omega_1 t_1+\omega_{ccl}t_2)}-\frac{\omega_1\omega_2}{\omega_{ccl}}(e^{-i\omega_2 t_1}-e^{-i\omega_1 t_1})\right].$$

Matrix $M_{fl}$ can be rewrite into a complex form,

$$M_{fl}=A+iB, \tag{C.8}$$

where,

$$A=\begin{pmatrix}A_{11} & A_{12}\\ A_{21} & A_{22}\end{pmatrix}, \tag{C.9}$$

$$B = \begin{pmatrix} B_{11} & B_{12} \\ B_{21} & B_{22} \end{pmatrix}, \tag{C.10}$$

and the matrix elements are given as the following,

$$A_{11} = \frac{\omega_1 \cos(\omega_2 t_1) - \omega_2 \cos(\omega_1 t_1)}{\omega_1 - \omega_2}, \qquad B_{11} = \frac{\omega_2 \sin(\omega_1 t_1) - \omega_1 \sin(\omega_2 t_1)}{\omega_1 - \omega_2},$$

$$A_{12} = \frac{(\omega_1 - \omega_{ccl}) \sin(\omega_2 t_1 + \omega_{ccl} t_2) - (\omega_2 - \omega_{ccl}) \sin(\omega_1 t_1 + \omega_{ccl} t_2) - \omega_1 \sin(\omega_2 t_1) + \omega_2 \sin(\omega_1 t_1)}{\omega_{ccl}(\omega_1 - \omega_2)},$$

$$B_{12} = \frac{(\omega_1 - \omega_{ccl}) \cos(\omega_2 t_1 + \omega_{ccl} t_2) - (\omega_2 - \omega_{ccl}) \cos(\omega_1 t_1 + \omega_{ccl} t_2) - \omega_1 \cos(\omega_2 t_1) + \omega_2 \cos(\omega_1 t_1)}{\omega_{ccl}(\omega_1 - \omega_2)},$$

$$A_{21} = \frac{\omega_1 \omega_2}{\omega_1 - \omega_2} (\sin(\omega_1 t_1) - \sin(\omega_2 t_1)), \qquad B_{21} = \frac{\omega_1 \omega_2}{\omega_1 - \omega_2} (\cos(\omega_1 t_1) - \cos(\omega_2 t_1)),$$

$$A_{22} = \frac{\omega_2(\omega_1 - \omega_{ccl}) \cos(\omega_2 t_1 + \omega_{ccl} t_2) - \omega_1(\omega_2 - \omega_{ccl}) \cos(\omega_1 t_1 + \omega_{ccl} t_2) - \omega_1 \omega_2 (\cos(\omega_2 t_1) - \cos(\omega_1 t_1))}{\omega_{ccl}(\omega_1 - \omega_2)},$$

$$B_{22} = \frac{-\omega_2(\omega_1 - \omega_{ccl}) \sin(\omega_2 t_1 + \omega_{ccl} t_2) + \omega_1(\omega_2 - \omega_{ccl}) \sin(\omega_1 t_1 + \omega_{ccl} t_2) + \omega_1 \omega_2 (\sin(\omega_2 t_1) - \sin(\omega_1 t_1))}{\omega_{ccl}(\omega_1 - \omega_2)}.$$

# CHAPTER 4. MONOPOLE AND QUADRUPOLE INSTABILITIES

Although the dipole type instabilities usually have lower density thresholds compared to higher order instabilities, they are relatively easy to be cured by the feed-back system. In circumstance where the dipole type instabilities are suppressed by diagnostic systems, the envelope oscillations become dominant which can deteriorate the beam quality and cause instabilities. In this chapter, we study what the electron beam does to the envelope oscillations and estimate the instabilities thresholds of these oscillations. In subsection 4.1, the transverse quadruple type envelope oscillation is studied and applied to the parameters of Fermi Lab Recycler Ring and RHIC. In subsection 4.2, the monopole type envelope oscillation is studied.

## *4.1 Quadruple Instability Due to Envelope Oscillation*

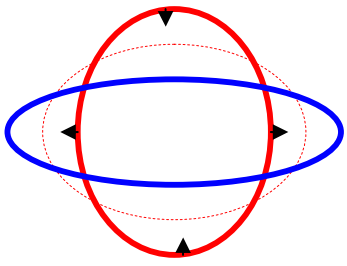

Figure 4.1 Quadrupole oscillation of the Ion beam for $B = 0$

In the presence of the electron beam inside the cooling section, except for the coherent dipole oscillation, the envelope oscillation of the ion beam could also be affected [12] by the electron beam as shown in Fig. 4.1. The purpose of subsection is to study this effects and find out what is the electron beam density threshold for the quadruple instability to happen. This subsection is following the paper written by V.Reva but the drift approximation for the electron beam is not used since the current electron cooler design has no solenoid within the cooling section. As shown in V.Reva's paper, the Vlasov equation inside a solenoid is

$$\frac{\partial f}{\partial t} + v_{\perp}\frac{\partial f}{\partial r_{\perp}} - K\left[r_{\perp}\frac{\partial f}{\partial v_{\perp}}\right] + \frac{e}{\gamma m}\left[E_{\perp}\frac{\partial f}{\partial v_{\perp}}\right] + \omega_{He}\left[v_{\perp}\times\hat{s}\right]\cdot\frac{\partial f}{\partial v_{\perp}} = 0. \tag{4.1}$$

With the following definition,

$$\xi = x + iz\,, \tag{4.2}$$

$$\eta = x - iz\,,$$

one gets

$$v_{\perp}\cdot\frac{\partial f}{\partial r_{\perp}} = v_{\xi}\frac{\partial f}{\partial \xi} + v_{\eta}\frac{\partial f}{\partial \eta}\,, \tag{4.3}$$

$$\left[v_{\perp}\times\hat{s}\right]\cdot\frac{\partial f}{\partial v_{\perp}} = -iv_{\xi}\frac{\partial f}{\partial v_{\xi}} + iv_{\eta}\frac{\partial f}{\partial v_{\eta}}\,, \tag{4.4}$$

$$E_{\perp}\cdot\frac{\partial f}{\partial v_{\perp}} = E_{+}\frac{\partial f}{\partial v_{\xi}} + E_{-}\frac{\partial f}{\partial v_{\eta}}\,. \tag{4.5}$$

As a result, the Vlasov equation can be written into the following form

$$\frac{\partial f}{\partial t} + v_{\xi}\frac{\partial f}{\partial \xi} + v_{\eta}\frac{\partial f}{\partial \eta} - K\left[\xi\frac{\partial f}{\partial v_{\xi}} + \eta\frac{\partial f}{\partial v_{\eta}}\right] + \frac{e}{\gamma m}\left[E_{+}\frac{\partial f}{\partial v_{\xi}} + E_{-}\frac{\partial f}{\partial v_{\eta}}\right] - i\omega_{He}\left[v_{\xi}\frac{\partial f}{\partial v_{\xi}} - v_{\eta}\frac{\partial f}{\partial v_{\eta}}\right] = 0. \tag{4.6}$$

Integrating this equation over the whole transverse phase space $\xi, \eta, v_\xi$ and $v_\eta$, one can obtain the following equations,

$$\begin{aligned}
&\frac{\partial\langle\xi_i^2\rangle}{\partial s} - 2\langle\xi_i\xi_i'\rangle = 0, \\
&\frac{\partial\langle\xi_i\xi_i'\rangle}{\partial s} - \langle\xi_i'^2\rangle - \frac{Z_i e}{\gamma m_i \beta^2 c^2}\langle\xi_i E_+\rangle = 0, \\
&\frac{\partial\langle\xi_i'^2\rangle}{\partial s} - \frac{2Z_i e}{\gamma m_i \beta^2 c^2}\langle\xi_i' E_+\rangle = 0.
\end{aligned} \tag{4.7}$$

The electron beam has the similar Vlasov equation as the ion beam and thus it has the following equations of motion

$$\begin{aligned}
&\frac{\partial\langle\xi_e^2\rangle}{\partial s} - 2\langle\xi_e\xi_e'\rangle = 0, \\
&\frac{\partial\langle\xi_e\xi_e'\rangle}{\partial s} - \langle\xi_e'^2\rangle + \frac{e}{\gamma m_e \beta^2 c^2}\langle\xi_e E_+\rangle = 0, \\
&\frac{\partial\langle\xi_e'^2\rangle}{\partial s} + \frac{2e}{\gamma m_e \beta^2 c^2}\langle\xi_e' E_+\rangle = 0.
\end{aligned} \tag{4.8}$$

In (7) and (8), we consider a long straight cooling section without any external field, i.e. $k_\perp = 0$. The space charge can be divided into two parts, the unperturbed dipole part and the perturbation coming from the distortion of the beam envelope from an initial round beam. Thus, one can write the space charge field into the following form,

$$\vec{E} = \vec{E}_{e,0} + \vec{E}_{e,1} + \vec{E}_{i,0} + \vec{E}_{i,1}.$$

The dipole part of the space charge is well known. In order to obtain the quadruple part of the space charge from the envelop distortion as shown in Fig. 4.2, one can rotate the

reference frame so that the ellipse is upright. For an upright elliptical beam, the transversal space charge is[9],

$$\vec{E}(x',y') = \frac{2Ne}{2\pi\varepsilon_0}\left[\frac{x'}{a(a+b)}\hat{i}' + \frac{y'}{b(a+b)}\hat{j}'\right]. \tag{4.9}$$

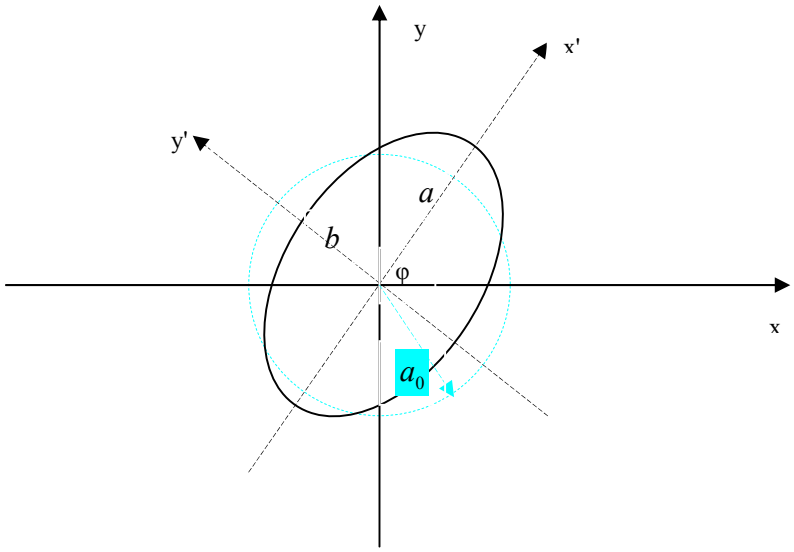


Figure 4.2 Illustration Of The Envelope Distortion and Coordinates System.

where N is the particle number per unit length and e is the charge of the particle. Since,

$$E_x = E_x^{'}\cos(\varphi) - E_y^{'}\sin(\varphi),$$

$$E_y = E_y^{'}\cos(\varphi) + E_x^{'}\sin(\varphi), \tag{4.10}$$

the transverse space charge electric fields in the un-rotated system are

$$E_x = \frac{2Ne}{2\pi\varepsilon_0}\frac{x\cos^2(\varphi) + y\sin(\varphi)\cos(\varphi)}{a(a+b)} + \frac{2Ne}{2\pi\varepsilon_0}\frac{x\sin^2(\varphi) - y\sin(\varphi)\cos(\varphi)}{b(a+b)},$$

[9] S.Y.Lee, 'Accelerator Physics', second edition, World Scientific Publishing Co.Pte.Ltd, p.69

$$E_y = \frac{2Ne}{2\pi\varepsilon_0}\frac{-x\sin(\varphi)\cos(\varphi)+y\cos^2(\varphi)}{a(a+b)} + \frac{2Ne}{2\pi\varepsilon_0}\frac{x\sin(\varphi)\cos(\varphi)+y\sin^2(\varphi)}{b(a+b)}.$$

Thus the electric fields due to the envelope distortion are obtained as

$$\begin{aligned} E_{1x} &= E_x - \frac{2Ne}{2\pi\varepsilon_0}\frac{x\cos^2(\varphi)+y\sin(\varphi)\cos(\varphi)}{2a_0^2} - \frac{2Ne}{2\pi\varepsilon_0}\frac{x\sin^2(\varphi)-y\sin(\varphi)\cos(\varphi)}{2a_0^2} \\ &\approx \frac{2Ne}{2\pi\varepsilon_0}\frac{x\cos(2\varphi)+y\sin(2\varphi)}{8a_0^4}(b^2-a^2) \end{aligned}, \qquad (4.11)$$

$$\begin{aligned} E_{1y} &= E_y - \frac{2Ne}{2\pi\varepsilon_0}\frac{-x\sin(\varphi)\cos(\varphi)+y\cos^2(\varphi)}{2a_0^2} - \frac{2Ne}{2\pi\varepsilon_0}\frac{x\sin(\varphi)\cos(\varphi)+y\sin^2(\varphi)}{2a_0^2} \\ &\approx \frac{2Ne}{2\pi\varepsilon_0}\frac{x\sin(2\varphi)-y\cos(2\varphi)}{8a_0^4}(b^2-a^2) \end{aligned}.$$

The components of the transverse electric field can be rewritten into the complex combination forms defined as the following,

$$E_{1+} \equiv E_{1x} + iE_{1y} = \frac{2Ne}{2\pi\varepsilon_0}\frac{\cos(2\varphi)+i\sin(2\varphi)}{8a_0^4}(b^2-a^2)\eta, \qquad (4.12)$$

$$E_{1-} \equiv E_{1x} - iE_{1y} = \frac{2Ne}{2\pi\varepsilon_0}\frac{\cos(2\varphi)-i\sin(2\varphi)}{8a_0^4}(b^2-a^2)\xi. \qquad (4.13)$$

Since the secondary moments of the beam can be expressed into the geometric parameters, i.e. $\langle x'^2\rangle = a^2$, $\langle y'^2\rangle = b^2$ and $\langle x'y'\rangle = 0$, equation (4.12) and (4.13) can be rewritten into

$$E_{1+} = -\frac{2\pi n_e e}{4\pi\varepsilon_0}\frac{1}{(d_0)^2}\langle\xi^2\rangle\eta, \qquad (4.14)$$

$$E_{1-} = -\frac{2\pi n_e e}{4\pi\varepsilon_0}\frac{1}{(d_0)^2}\langle\eta^2\rangle\xi. \qquad (4.15)$$

where $d_0 = 2a_0$ is the diameter of the beam and $n_e$ is the charge density. As dipole space charge field is

$$E_{0+} = \frac{2\pi Z_i e n_i}{\gamma^2}\xi - \frac{2\pi e n_e}{\gamma^2}\xi,$$

$$E_{0-} = \frac{2\pi Z_i e n_i}{\gamma^2}\eta - \frac{2\pi e n_e}{\gamma^2}\eta,$$

one can obtain the following results,

$$\left\langle E_+ \xi_i \right\rangle = -\frac{\pi Z_i e n_i}{\gamma^2}\left\langle \xi_i^2 \right\rangle + \frac{\pi e n_e}{\gamma^2}\left\langle \xi_e^2 \right\rangle + \frac{2\pi Z_i e n_i}{\gamma^2}\left\langle \xi_i^2 \right\rangle - \frac{2\pi e n_e}{\gamma^2}\left\langle \xi_i^2 \right\rangle,$$

$$\left\langle E_+ \xi_i' \right\rangle = -\frac{i\pi Z_i e n_i}{2\lambda_{Hi}\gamma^2}\left\langle \xi_i^2 \right\rangle + \frac{i\pi e n_e}{2\lambda_{Hi}\gamma^2}\left\langle \xi_e^2 \right\rangle + \frac{2\pi Z_i e n_i}{\gamma^2}\left\langle \xi_i' \xi_i \right\rangle - \frac{2\pi e n_e}{\gamma^2}\left\langle \xi_i' \xi_i \right\rangle.$$

Thus equation (4.7) can be written as

$$\frac{\partial\langle \xi_i \xi_i' \rangle}{\partial s} - \left\langle \xi_i'^2 \right\rangle - \frac{1}{\lambda_{pi}^2}\left\langle \xi_i^2 \right\rangle + \frac{2}{\lambda_{ie}^2}\left\langle \xi_i^2 \right\rangle = \frac{1}{\lambda_{ie}^2}\left\langle \xi_e^2 \right\rangle,$$

where $\lambda_{pi}^2 = \dfrac{\gamma^3 m_i \beta^2 c^2}{\pi Z_i^2 e^2 n_i} = \dfrac{2\beta^2 c^2}{\omega_{pi}^2}$ and $\lambda_{ie}^2 = \dfrac{\gamma^3 m_i \beta^2 c^2}{\pi Z_i e^2 n_e} = \dfrac{2\beta^2 c^2}{\omega_{ie}^2}$. For $B = 0$, the equations of motion are

$$\frac{\partial\left\langle \xi_i^2 \right\rangle}{\partial s} - 2\langle \xi_i \xi_i' \rangle = 0, \tag{4.16a}$$

$$\frac{\partial\langle \xi_i \xi_i' \rangle}{\partial s} - \left\langle \xi_i'^2 \right\rangle + \left(\frac{2}{\lambda_{ie}^2} - \frac{1}{\lambda_{pi}^2}\right)\left\langle \xi_i^2 \right\rangle = \frac{1}{\lambda_{ie}^2}\left\langle \xi_e^2 \right\rangle, \tag{4.16b}$$

$$\frac{\partial\left\langle \xi_i'^2 \right\rangle}{\partial s} + 4\left(\frac{1}{\lambda_{ie}^2} - \frac{1}{\lambda_{pi}^2}\right)\left\langle \xi_i' \xi_i \right\rangle = 0. \tag{4.16c}$$

Similarly, the equation of motion for electron beam envelop are

$$\frac{\partial\left\langle \xi_e^2 \right\rangle}{\partial s} - 2\langle \xi_e \xi_e' \rangle = 0, \tag{4.17a}$$

$$\frac{\partial\langle\xi_e\xi_e'\rangle}{\partial s}-\langle\xi_e'^2\rangle+\left(\frac{2}{\lambda_{ei}^2}-\frac{1}{\lambda_{pe}^2}\right)\langle\xi_e^2\rangle=\frac{1}{\lambda_{ei}^2}\langle\xi_i^2\rangle, \tag{4.17b}$$

$$\frac{\partial\langle\xi_e'^2\rangle}{\partial s}+4\left(\frac{1}{\lambda_{ei}^2}-\frac{1}{\lambda_{pe}^2}\right)\langle\xi_e'\xi_e\rangle=0. \tag{4.17c}$$

Combining (4.16a) and (4.16b) and integrating the equation over the longitudinal location s, one gets

$$\langle\xi_i'^2\rangle+2\left(\frac{1}{\lambda_{ie}^2}-\frac{1}{\lambda_{pi}^2}\right)\langle\xi_i^2\rangle=C_{1i}, \tag{4.18}$$

where $C_{1i}$ is the integration constant to be determined by the initial condition. Similar equation can also be obtained for the electron beam,

$$\langle\xi_e'^2\rangle+2\left(\frac{1}{\lambda_{ei}^2}-\frac{1}{\lambda_{pe}^2}\right)\langle\xi_e^2\rangle=C_{1e}. \tag{4.19}$$

Thus, equation (4.7) and (4.8) are reduced to the following forms

$$\frac{\partial^2}{\partial t^2}\begin{pmatrix}\langle\xi_i^2\rangle\\ \langle\xi_e^2\rangle\end{pmatrix}=\begin{pmatrix}3\omega_{pi}^2-4\omega_{ie}^2 & \omega_{ie}^2\\ \omega_{ei}^2 & 3\omega_{pe}^2-4\omega_{ei}^2\end{pmatrix}\begin{pmatrix}\langle\xi_i^2\rangle\\ \langle\xi_e^2\rangle\end{pmatrix}+\begin{pmatrix}2C_{1i}\\ 2C_{1e}\end{pmatrix}(\beta c)^2. \tag{4.22}$$

Suppose matrix M can diagonalize the above square matrix, i.e.

$$\frac{\partial^2}{\partial t^2}M\begin{pmatrix}\langle\xi_i^2\rangle\\ \langle\xi_e^2\rangle\end{pmatrix}=\begin{pmatrix}-\omega_1^2 & 0\\ 0 & -\omega_2^2\end{pmatrix}M\begin{pmatrix}\langle\xi_i^2\rangle\\ \langle\xi_e^2\rangle\end{pmatrix}+M\begin{pmatrix}2C_{1i}\\ 2C_{1e}\end{pmatrix}(\beta c)^2. \tag{4.23}$$

With the following definition,

$$\begin{pmatrix}\langle\xi_1^2\rangle\\ \langle\xi_2^2\rangle\end{pmatrix}\equiv M\begin{pmatrix}\langle\xi_i^2\rangle\\ \langle\xi_e^2\rangle\end{pmatrix},\qquad \begin{pmatrix}C_1\\ C_2\end{pmatrix}\equiv M\begin{pmatrix}2C_{1i}\\ 2C_{1e}\end{pmatrix}(\beta c)^2. \tag{4.24}$$

one can rewrite equation (4.23) as

$$\frac{\partial^2}{\partial t^2}\langle\xi_1^2\rangle=-\omega_1^2\langle\xi_1^2\rangle+C_1, \tag{4.25}$$

$$\frac{\partial^2}{\partial t^2}\left\langle \xi_2^2 \right\rangle = -\omega_2^2 \left\langle \xi_2^2 \right\rangle + C_2 , \tag{4.26}$$

where

$$C_1 \equiv 2m_{11}\left[\left\langle \dot{\xi}_i^2 \right\rangle_0 + \left(\omega_{ie}^2 - \omega_{pi}^2\right)\left\langle \xi_i^2 \right\rangle_0\right] + 2m_{12}\left[\left\langle \dot{\xi}_e^2 \right\rangle_0 + \left(\omega_{ei}^2 - \omega_{pe}^2\right)\left\langle \xi_e^2 \right\rangle_0\right], \tag{4.29}$$

$$C_2 \equiv 2m_{21}\left[\left\langle \dot{\xi}_i^2 \right\rangle_0 + \left(\omega_{ie}^2 - \omega_{pi}^2\right)\left\langle \xi_i^2 \right\rangle_0\right] + 2m_{22}\left[\left\langle \dot{\xi}_e^2 \right\rangle_0 + \left(\omega_{ei}^2 - \omega_{pe}^2\right)\left\langle \xi_e^2 \right\rangle_0\right]. \tag{4.30}$$

Setting the electron beam initial condition to be $\left\langle \xi_e'^2 \right\rangle_0 = \left\langle \xi_e^2 \right\rangle_0 = 0$, the solution is derived to be

$$\left\langle \xi_1^2 \right\rangle = A_1 \cos(\omega_1 t + \varphi_1) + \frac{2m_{11}\left[\left\langle \xi_i'^2 \right\rangle_0 + \left(\omega_{ie}^2 - \omega_{pi}^2\right)\left\langle \xi_i^2 \right\rangle_0\right]}{\omega_1^2}. \tag{4.31}$$

By (4.12a), one gets

$$\frac{\partial\left\langle \xi_i^2 \right\rangle_0}{\partial t} = 2\left\langle \xi_i \dot{\xi}_i \right\rangle_0 , \tag{4.32}$$

which combining with equation (4.24) produce the following initial conditions

$$\frac{\partial\left\langle \xi_1^2 \right\rangle_0}{\partial t} = 2m_{11}\left\langle \xi_i \dot{\xi}_i \right\rangle_0 + 2m_{12}\left\langle \xi_e \dot{\xi}_e \right\rangle_0 = 2m_{11}\left\langle \xi_i \dot{\xi}_i \right\rangle_0 , \tag{4.33}$$

where we have used the electron beam initial condition, $\left\langle \xi_e \dot{\xi}_e \right\rangle_0 = 0$. From (4.31) and (4.33), one gets

$$A_1 \cos(\varphi_1) = \left\langle \xi_1^2 \right\rangle_0 - \frac{2m_{11}\left[\left\langle \dot{\xi}_i^2 \right\rangle_0 + \left(\omega_{ie}^2 - \omega_{pi}^2\right)\left\langle \xi_i^2 \right\rangle_0\right]}{\omega_1^2}, \tag{4.34}$$

$$A_1 \sin(\varphi_1) = -\frac{2m_{11}\left\langle \xi_i \dot{\xi}_i \right\rangle_0}{\omega_1}. \tag{4.35}$$

Thus one can rewrite the solution (4.31) as

$$\left\langle \xi_1^2 \right\rangle = m_{11}\left[\left(\cos(\omega_1 t) + \frac{2\left(\omega_{ie}^2 - \omega_{pi}^2\right)}{\omega_1^2}(1-\cos(\omega_1 t))\right)\left\langle \xi_i^2 \right\rangle_0 + \frac{2\sin(\omega_1 t)}{\omega_1}\left\langle \xi_i \dot{\xi}_i \right\rangle_0 + \frac{2}{\omega_1^2}(1-\cos(\omega_1 t))\left\langle \dot{\xi}_i^2 \right\rangle_0\right]. \quad (4.36)$$

Similar procedures produce the solution for $\left\langle \xi_2^2 \right\rangle$ as

$$\left\langle \xi_2^2 \right\rangle = m_{21}\left[\left(\cos(\omega_2 t) + \frac{2\left(\omega_{ie}^2 - \omega_{pi}^2\right)}{\omega_2^2}(1-\cos(\omega_2 t))\right)\left\langle \xi_i^2 \right\rangle_0 + \frac{2\sin(\omega_2 t)}{\omega_2}\left\langle \xi_i \dot{\xi}_i \right\rangle_0 + \frac{2}{\omega_2^2}(1-\cos(\omega_2 t))\left\langle \dot{\xi}_i^2 \right\rangle\right]. \quad (4.37)$$

The solutions can then be inverted according to the following formula,

$$\begin{pmatrix} \left\langle \xi_i^2 \right\rangle \\ \left\langle \xi_e^2 \right\rangle \end{pmatrix} = M^{-1}\begin{pmatrix} \left\langle \xi_1^2 \right\rangle \\ \left\langle \xi_2^2 \right\rangle \end{pmatrix} = \frac{1}{\det(M)}\begin{pmatrix} m_{22} & -m_{12} \\ -m_{21} & m_{11} \end{pmatrix}\begin{pmatrix} \left\langle \xi_1^2 \right\rangle \\ \left\langle \xi_2^2 \right\rangle \end{pmatrix}. \quad (4.38)$$

From equation (4.38), the second order moments of the electron and the ion beam can thus be expressed into the following matrix form

$$\begin{pmatrix} \left\langle \xi_i^2 \right\rangle \\ \left\langle \xi_i \xi_i' \right\rangle \\ \left\langle \xi_i'^2 \right\rangle \end{pmatrix} = M_{cool}\begin{pmatrix} \left\langle \xi_i^2 \right\rangle_0 \\ \left\langle \xi_i \xi_i' \right\rangle_0 \\ \left\langle \xi_i'^2 \right\rangle_0 \end{pmatrix} = \begin{pmatrix} A_{11} & A_{12}(\beta c) & A_{13}(\beta c)^2 \\ \frac{A_{21}}{(\beta c)} & A_{22} & A_{23}(\beta c) \\ \frac{A_{31}}{(\beta c)^2} & \frac{A_{32}}{(\beta c)} & A_{33} \end{pmatrix}\begin{pmatrix} \left\langle \xi_i^2 \right\rangle_0 \\ \left\langle \xi_i \xi_i' \right\rangle_0 \\ \left\langle \xi_i'^2 \right\rangle_0 \end{pmatrix}, \quad (4.39)$$

where

$$A_{11} = \frac{m_{11}m_{22}}{|M|}\left(\cos(\omega_1 t) + \frac{2\left(\omega_{ie}^2 - \omega_{pi}^2\right)}{\omega_1^2}(1-\cos(\omega_1 t))\right) - \frac{m_{12}m_{21}}{|M|}\left(\cos(\omega_2 t) + \frac{2\left(\omega_{ie}^2 - \omega_{pi}^2\right)}{\omega_2^2}(1-\cos(\omega_2 t))\right),$$

$$A_{12} = \frac{2m_{11}m_{22}\sin(\omega_1 t)}{|M|\omega_1} - \frac{2m_{12}m_{21}\sin(\omega_2 t)}{|M|\omega_2}, \qquad A_{13} = \frac{2m_{11}m_{22}}{|M|\omega_1^2}(1-\cos(\omega_1 t)) - \frac{2m_{12}m_{21}}{|M|\omega_2^2}(1-\cos(\omega_2 t)),$$

$$A_{21} = \frac{1}{2|M|}\left[m_{11}m_{22}\left(\frac{2\left(\omega_{ie}^2 - \omega_{pi}^2\right)}{\omega_1}\sin(\omega_1 t) - \omega_1\sin(\omega_1 t)\right) - m_{12}m_{21}\left(\frac{2\left(\omega_{ie}^2 - \omega_{pi}^2\right)}{\omega_2}\sin(\omega_2 t) - \omega_2\sin(\omega_2 t)\right)\right],$$

$$A_{22} = \frac{\left[m_{11}m_{22}\cos(\omega_1 t) - m_{12}m_{21}\cos(\omega_2 t)\right]}{|M|}, \quad A_{23} = \frac{1}{|M|}\left(\frac{m_{11}m_{22}}{\omega_1}\sin(\omega_1 t) - \frac{m_{12}m_{21}}{\omega_2}\sin(\omega_2 t)\right).$$

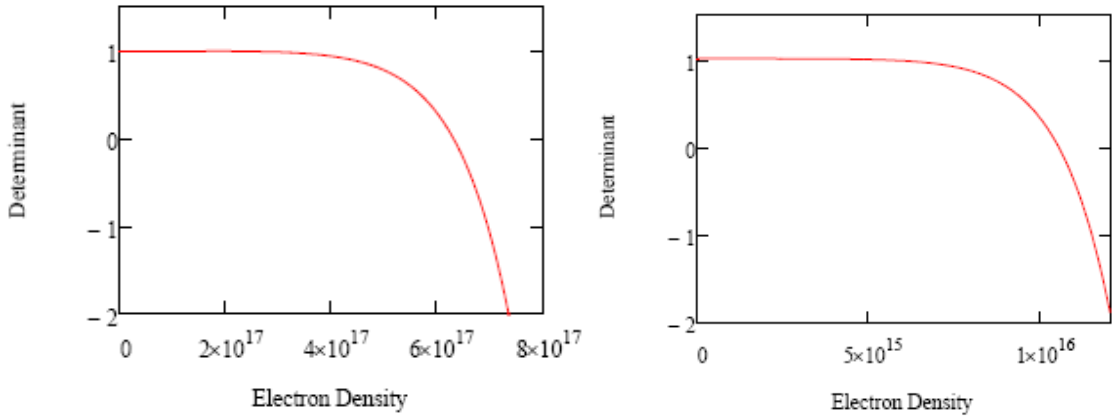


(a) (b)

Figure 4.3 Growth rate due to envelope oscillation for RHIC Gold Ion beam and Fermilab Recycler Ring Proton Beam. The abscissa is the electron density in the lab frame in unit of $m^{-3}$ and the ordinate is the determinant of the one turn transfer matrix.. (a) is calculated for RHIC parameters and (b) is for Fermilab Recycler Ring.

$$A_{31} = (1 - A_{11})\left(\omega_{ie}^2 - \omega_{pi}^2\right), \qquad A_{32} = -\left(\omega_{ie}^2 - \omega_{pi}^2\right)A_{12}, \qquad A_{33} = 1 - \left(\omega_{ie}^2 - \omega_{pi}^2\right)A_{13}.$$

To include the rest part of the ring, the transfer matrix for the drift space and Twiss matrix are given as the following,

$$M_{twiss} = \begin{pmatrix} \frac{1}{2}(1+\cos(4\pi\nu)) & \beta_\perp \sin(4\pi\nu) & \frac{\beta_\perp^2}{2}(1-\cos(4\pi\nu)) \\ -\frac{1}{2\beta_\perp}\sin(4\pi\nu) & \cos(4\pi\nu) & \frac{\beta_\perp}{2}\sin(4\pi\nu) \\ \frac{1}{2\beta_\perp^2}(1-\cos(4\pi\nu)) & -\frac{1}{\beta_\perp}\sin(4\pi\nu) & \frac{1}{2}(1+\cos(4\pi\nu)) \end{pmatrix}, \qquad (4.40)$$

$$M_{drift}(L) = \begin{pmatrix} 1 & 2L & L^2 \\ 0 & 1 & L \\ 0 & 0 & 1 \end{pmatrix}. \qquad (4.40)$$

The one turn transfer matrix for the ring is

$$M_{ring} = M_{drift}(-\frac{L}{2})M_{twiss}M_{drift}(-\frac{L}{2})M_{cool}\,. \tag{4.41}$$

The instability happens when the determinant or the eigenvalues are greater than 1. Fig. 4.3 shows the calculated determinant and eigenvalues for designed RHIC Electron-cooler and Fermilab's Recycler electron cooling system. The designed electron beam density for RHIC ecooling beam is $n_{e,RHIC} = 2.97 \times 10^{16} m^{-3}$ and that for FNAL Recycler is $n_{e,FNAL} = 1.64 \times 10^{14} m^{-3}$. Since both of them are orders of magnitude smaller than the instability threshold as shown in Fig. 4.3, the quadruple type envelope oscillation due to the interaction with electron beam should not happen.

### *4.2 Monopole Mode Envelope Oscillation*

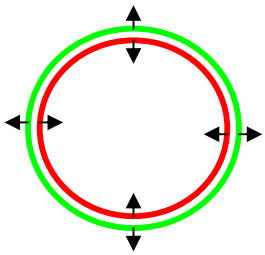

Figure 4.4 Illustration of Breathing Mode Envelope Oscillation.

Due to space charge interaction, the envelope oscillation is generally composed of the quadruple oscillation where the area of the beam density does not change and the monopole type oscillation where the beam density does change. The monopole type oscillation is also known as the envelope oscillation of the breathing mode which can be described by the well established envelope equation. In this section, we are going to derive the instability threshold from the envelope equations of the ion and electron beam. Consider both electron beam and ion beam have K-V distribution, the space charge potential is

$$\phi(x,y) = -\frac{\lambda_i}{2\pi\varepsilon_0}\left[\frac{x^2}{(R_{i,x}+R_{i.y})R_{i,x}} + \frac{y^2}{(R_{i,x}+R_{i.y})R_{i,y}}\right] + \frac{\lambda_e}{2\pi\varepsilon_0}\left[\frac{x^2}{(R_{e,x}+R_{e.y})R_{e,x}} + \frac{y^2}{(R_{e,x}+R_{e.y})R_{e,y}}\right]. \tag{4.42}$$

Single particle transversal equations of motion are given by

$$x_i'' - \left[\frac{2Q_{pi}}{(R_{i,x}+R_{i.y})R_{i,x}} - \frac{2Q_{ie}}{(R_{e,x}+R_{e.y})R_{e,x}}\right]x_i = 0, \tag{4.43}$$

$$x_e'' - \left[\frac{2Q_{pe}}{(R_{e,x}+R_{e.y})R_{e,x}} - \frac{2Q_{ei}}{(R_{i,x}+R_{i.y})R_{i,x}}\right]x_e = 0, \tag{4.44}$$

where the space charge space charge perveances are defined as

$$Q_{pi} \equiv \frac{Z_i e\lambda_i}{2\pi\varepsilon_0\gamma^3\beta^2c^2m_i}, \qquad Q_{ie} \equiv \frac{Z_i e\lambda_e}{2\pi\varepsilon_0\gamma^3\beta^2c^2m_i},$$

$$Q_{pe} \equiv \frac{e\lambda_e}{2\pi\varepsilon_0\gamma^3\beta^2c^2m_e}, \qquad Q_{ei} \equiv \frac{e\lambda_i}{2\pi\varepsilon_0\gamma^3\beta^2c^2m_e}. \tag{4.45}$$

and the RMS transverse beam size is defined as

$$R_{i,x}^2 = 4\langle x_i^2\rangle, \qquad R_{i,y}^2 = 4\langle y_i^2\rangle,$$

$$R_{e,x}^2 = 4\langle x_e^2\rangle, \qquad R_{e,y}^2 = 4\langle y_e^2\rangle. \tag{4.46}$$

Then, let's derive the envelope equation from the single particle equation of motion. Since the distribution function only depends on the Courant-Snyder invariant which is a constant of particle motion, it satisfies[10]

$$\frac{\partial}{\partial s} f(G) = 0,$$

where

$$G = \frac{1}{\varepsilon_x}\left[\frac{x^2}{w_x^2} + (w_x x' - w_x' x)^2\right] + \frac{1}{\varepsilon_y}\left[\frac{y^2}{w_y^2} + (w_y y' - w_y' y)^2\right],$$

and for K-V distribution[11] $f(G) = f_0 \delta(G-1)$ and $R_{i,x} = 2\sqrt{\langle x_i^2 \rangle}$. Taking the second order derivative of R, one gets

$$R_{i,x}'' = \frac{16\left(\langle x_i'^2 \rangle \langle x_i^2 \rangle - \langle x_i x_i' \rangle^2\right)}{R_{i,x}^3} + \frac{4\langle x_i x_i'' \rangle}{R_{i,x}}. \tag{4.47}$$

The definition of the transverse emittance is

$$\varepsilon_{i,x} \equiv 4\left(\langle x_i'^2 \rangle \langle x_i^2 \rangle - \langle x_i x_i' \rangle^2\right)^{\frac{1}{2}}. \tag{4.48}$$

Inserting equation (4.48) and (4.43) into (4.47), one gets

$$R_{i,x}'' - \frac{\varepsilon_{i,x}^2}{R_{i,x}^3} - \frac{2Q_{pi}}{R_{i,x} + R_{i.y}} + \frac{2Q_{ie}R_{i,x}}{(R_{e,x} + R_{e.y})R_{e,x}} = 0. \tag{4.49}$$

Similarly, one can get the envelope equation of the electron beam as below

$$R_{e,x}'' - \frac{\varepsilon_{e,x}^2}{R_{e,x}^3} - \frac{2Q_{pe}}{R_{e,x} + R_{e.y}} + \frac{2Q_{ei}R_{e,x}}{(R_{i,x} + R_{i.y})R_{i,x}} = 0. \tag{4.50}$$

[10] Martin Reiser, 'Theory and design of charged particle beams', Wiley Series In Beam Physics And Accelerator Technology, P.343.
[11] Actually other beam distribution can have a similar envelope equation due to equivalent concept. Refer to M.Reiser, P.362.

Considering the beam having a matched envelope plus a small perturbation, one can write the beam radius as $R = R_m + \delta R$. Since the matched beam envelopes satisfy the envelope equation (4.49) and (4.50), the linearized equations of motion for the perturbation are

$$\delta R_{i,x}'' + \frac{3\varepsilon_i^2}{R_{im}^4}\delta R_{i,x} + \frac{Q_{pi}}{2R_{im}^2}(\delta R_{i,x} + \delta R_{i,y}) + \frac{Q_{ie}\delta R_{i,x}}{R_{em}^2} - \frac{Q_{ie}R_{im}}{R_{em}^3}\delta R_{e,x} - \frac{Q_{ie}R_{im}(\delta R_{e,x} + \delta R_{e,y})}{2R_{em}^3} = 0, \quad (4.51)$$

$$\delta R_{i,y}'' + \frac{3\varepsilon_i^2}{R_{im}^4}\delta R_{i,y} + \frac{Q_{pi}}{2R_{im}^2}(\delta R_{i,x} + \delta R_{i,y}) + \frac{Q_{ie}\delta R_{i,y}}{R_{em}^2} - \frac{Q_{ie}R_{im}}{R_{em}^3}\delta R_{e,y} - \frac{Q_{ie}R_{im}(\delta R_{e,x} + \delta R_{e,y})}{2R_{em}^3} = 0, \quad (4.52)$$

where the following assumptions have been made

$$R_{im,x} = R_{im,y} = R_{im}, \quad (4.53a)$$

$$R_{em,x} = R_{em,y} = R_{em}, \quad (4.53b)$$

$$\varepsilon_{i,x} = \varepsilon_{i,y} = \varepsilon_i, \quad (4.53c)$$

$$\varepsilon_{e,x} = \varepsilon_{e,y} = \varepsilon_e. \quad (4.53d)$$

In order to obtain the equation for breathing mode, we define,

$$\delta R_i = \delta R_{i,x} + \delta R_{i,y},$$

$$\delta R_e = \delta R_{e,x} + \delta R_{e,y}.$$

Summing up (4.51) and (4.52), one gets

$$\delta R_i'' + \left(\frac{3\varepsilon_i^2}{R_{im}^4} + \frac{Q_{pi}}{2R_{im}^2} + \frac{Q_{ie}}{R_{em}^2}\right)\delta R_i - \frac{2Q_{ie}R_{im}}{R_{em}^3}\delta R_e = 0. \quad (4.54)$$

Similarly, for the electron beam, one can get

$$\delta R_e'' + \left(\frac{3\varepsilon_e^2}{R_{em}^4} + \frac{Q_{pe}}{2R_{em}^2} + \frac{Q_{ei}}{R_{im}^2}\right)\delta R_e - \frac{2Q_{ei}R_{em}}{R_{im}^3}\delta R_i = 0. \quad (4.55)$$

Equation (4.54) and (4.55) can be written into the following matrix forms

$$\frac{\partial^2}{\partial s^2}\begin{pmatrix}\delta R_i\\ \delta R_e\end{pmatrix}=\begin{pmatrix}-\left(\frac{3\varepsilon_i^2}{R_{im}^4}+\frac{Q_{pi}}{2R_{im}^2}+\frac{Q_{ie}}{R_{em}^2}\right) & \frac{2Q_{ie}R_{im}}{R_{em}^3}\\ \frac{2Q_{ei}R_{em}}{R_{im}^3} & -\left(\frac{3\varepsilon_e^2}{R_{em}^4}+\frac{Q_{pe}}{2R_{em}^2}+\frac{Q_{ei}}{R_{im}^2}\right)\end{pmatrix}\begin{pmatrix}\delta R_i\\ \delta R_e\end{pmatrix}. \tag{4.56}$$

Assuming matrix M can diagonalize the above square matrix, i.e.

$$\frac{\partial^2}{\partial s^2}M\begin{pmatrix}\delta R_i\\ \delta R_e\end{pmatrix}=\begin{pmatrix}-k_1^2 & 0\\ 0 & -k_2^2\end{pmatrix}M\begin{pmatrix}\delta R_i\\ \delta R_e\end{pmatrix}, \tag{4.57}$$

equation (4.57) can be rewritten as

$$\frac{\partial^2}{\partial s^2}\begin{pmatrix}\delta R_1\\ \delta R_2\end{pmatrix}=\begin{pmatrix}-k_1^2 & 0\\ 0 & -k_2^2\end{pmatrix}\begin{pmatrix}\delta R_1\\ \delta R_2\end{pmatrix}, \tag{4.58}$$

where

$$\begin{pmatrix}\delta R_1\\ \delta R_2\end{pmatrix}\equiv M\begin{pmatrix}\delta R_i\\ \delta R_e\end{pmatrix}. \tag{4.59}$$

The solution of (4.58) is

$$\delta R_1 = A_1\cos(k_1 s+\varphi_1), \tag{4.60}$$

$$\delta R_2 = A_2\cos(k_2 s+\varphi_2). \tag{4.61}$$

Appling the initial condition for electron beam

$$\delta R_e(0)=\frac{-m_{21}\delta R_1(0)+m_{11}\delta R_2(0)}{\det(M)}=0, \tag{4.62a}$$

$$\delta R_e'(0)=\frac{-m_{21}\delta R_1'(0)+m_{11}\delta R_2'(0)}{\det(M)}=0, \tag{4.62b}$$

$$\delta R_i(0)=\frac{m_{22}\delta R_1(0)-m_{12}\delta R_2(0)}{\det(M)}, \tag{4.62c}$$

$$\delta R_i'(0)=\frac{m_{22}\delta R_1'(0)-m_{12}\delta R_2'(0)}{\det(M)}, \tag{4.62d}$$

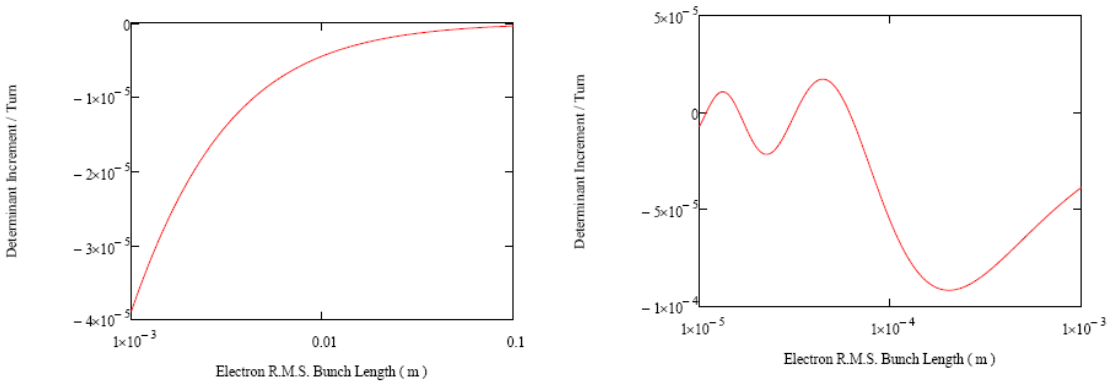


(a) (b)

Figure 4.5 The growth rate of breathing mode envelope oscillation within cooling section as a function of the electron rms bunch length for 5 nC total electron beam charge. The abscissa represents the rms electron bunch length in units of meter. (a) and (b) are for different range of bunch lengthes.

and using the inversion of equation (4.59)

$$\begin{pmatrix} \delta R_i \\ \delta R_e \end{pmatrix} \equiv M^{-1} \begin{pmatrix} \delta R_1 \\ \delta R_2 \end{pmatrix} = \frac{1}{\det(M)} \begin{pmatrix} m_{22} & -m_{12} \\ -m_{21} & m_{11} \end{pmatrix} \begin{pmatrix} \delta R_1 \\ \delta R_2 \end{pmatrix}, \tag{4.63}$$

the solution of (4.56) can be expressed into the following matrix form,

$$\begin{pmatrix} \delta R_i \\ \delta R_i' \end{pmatrix} = \begin{pmatrix} A_{11} & A_{12} \\ A_{21} & A_{22} \end{pmatrix} \begin{pmatrix} \delta R_i(0) \\ \delta R_i'(0) \end{pmatrix}, \tag{4.64}$$

where

$$A_{11} = \frac{1}{\det(M)} \left( m_{11} m_{22} \cos(k_1 s) - m_{12} m_{21} \cos(k_2 s) \right),$$

$$A_{12} = \frac{1}{\det(M)} \left( m_{11} m_{22} \frac{\sin(k_1 s)}{k_1} - m_{12} m_{21} \frac{\sin(k_2 s)}{k_2} \right),$$

$$A_{21} = \frac{1}{\det(M)}\left(m_{12}m_{21}k_2 \sin(k_2 s) - m_{11}m_{22}k_1 \sin(k_1 s)\right),$$

$$A_{22} = \frac{1}{\det(M)}\left(m_{11}m_{22} \cos(k_1 s) - m_{12}m_{21} \cos(k_2 s)\right).$$

Thus the growth rate for the breathing mode coming from the determinant increment is

$$\Gamma_{\det} = \frac{-m_{11}m_{22}m_{12}m_{21}\left(2\cos(k_1 s)\cos(k_2 s) + \frac{k_2^2 + k_1^2}{k_1 k_2}\sin(k_1 s)\sin(k_2 s) - 2\right)}{\det(M)^2}. \quad (4.65)$$

As an example, Fig. 4.5 shows the results of (4.65) calculated for the designed RHIC Electron Cooler parameters. It is shown that for the current electron beam design, the electron rms bunch length is 1cm which corresponds to a damping rate $\Gamma = -4.5 \times 10^{-6}$ which corresponds to a damping time of 2.8 seconds.

# CHAPTER 5. SIMULATIONS OF RHIC INSTABILITY IN PRESENCE OF ECOOLING

Although the major task of RHIC-II electron cooling is to compensate the transverse emittance growth due to IBS, the longitudinal cooling could also happen for certain cooling schemes[13]. As a result, the energy spread of the ion beam decreases with the cooling process and may eventually destroy the Landau damping. Depending on the specific impedances of the machine, either longitudinal or transverse coherent instabilities will take place and thus cause emittance deterioration or beam loss. On the other hand, the electron beam itself can also coherently interact with the ion beam and thus affect the instability threshold and growth rate. A tracking code, TRAFT, is used to study the coherent instability of the RHIC ion beam with the coherent effects of the electron cooling being taken into account. In section 5.1, we describe the simulation algorithm and the impedances used for the RHIC simulation. In section 5.2, the simulation results are shown and the energy spread threshold for the instability is compared with analytic formula derived from the coasting beam dispersion relation. For the current $10^9$ ions per bunch, when the chromaticity is set to a slightly positive value at the top energy, the longitudinal instability happens before the transverse instability as the energy spread decreasing. However this is not true for a longer bunch with the same longitudinal phase space density. For fixed bunch length and increasing particle numbers, the transverse head-tail instability happens before the longitudinal instability but its

growth can be suppressed by the coherent damping effect of the electron beam, which is shown in section 5.3. We make conclusion in section 5.4.

### *5.1 Tracking Codes Description*

The FORTRAN program TRANFT simulates coherent instability in circular machine by using FFT logarithms. Each ion bunch is represented by $10^4 \sim 10^5$ macro particles, which are updated every turn according to the following equations[14]

$$\varepsilon_{n+1} = \varepsilon_n + \frac{q}{mc^2}\left[V_{rf}(\tau_n) - V_{s,n}(\tau_n)\right], \tag{5.1}$$

$$\tau_{n+1} = \tau_n + \frac{T_0\eta}{\beta^2\gamma_0}\varepsilon_{n+1}, \tag{5.2}$$

$$\begin{pmatrix} x \\ p_x \end{pmatrix}_{n+1} = M_{ecool} M_{wake} M_{TWISS} \begin{pmatrix} x \\ p_x \end{pmatrix}_n, \tag{5.3}$$

where $\varepsilon$ is the energy deviation in units of $\gamma_0$ and $\tau$ is the arrival time of the particle with respect of the synchronous particle. $V_{s,n}$ is the longitudinal voltage due to the Wakefield and is calculated by convolving the beam current with the Wakefield.

$$V_s(t) = -\int_{-\tau_b}^{\tau_b} W_s(\tau) I(t-\tau) d\tau . \tag{5.4}$$

Equation (5.5.3) is a short hand expression for three different transverse effects. $M_{TWISS}$ is the effect due to external focusing, which can be written as

$$M_{TWISS}\begin{pmatrix} x \\ p_x \end{pmatrix}_n = \begin{pmatrix} \cos(2\pi\nu_x) & \beta_{avg}\sin(2\pi\nu_x) \\ -\dfrac{\sin(2\pi\nu_x)}{\beta_{avg}} & \cos(2\pi\nu_x) \end{pmatrix}\begin{pmatrix} x-\delta_n D_x \\ p_x \end{pmatrix}_n + \delta_{n+1}\begin{pmatrix} D_x \\ 0 \end{pmatrix} \qquad (5.5)$$

, where $\delta_n = \dfrac{\varepsilon_n}{\gamma_0 - \gamma_0^{-1}}$ and $\nu_x = \nu_{x,0} + \xi_x\delta_n$. $M_{wake}$ is the transverse kick due to Wakefield and can be calculated by convolving the dipole momentum of the beam with the transverse Wakefield.

$$M_{wake}\begin{pmatrix} x \\ p_x \end{pmatrix} = \begin{pmatrix} x \\ p_x + \Delta p_x \end{pmatrix}, \qquad (5.6)$$

$$\Delta p_x = -\int_{-\tau_b}^{\tau_b} W_x(\tau)D(t-\tau)d\tau\,. \qquad (5.7)$$

The dipole momentum is defined as $D(t) \equiv I(t)\langle x(t)\rangle$. In principal, one can directly apply equation (5.5.4) and (5.5.7) to sum up the contribution from each macro-particle. However the amount of calculations can be greatly reduced by placing the macro-particles in an evenly distributed grids and use FFT technique to calculate the longitudinal and transverse voltages. Since the convolution in time domain is equivalent to multiply in the frequency domain, the Wakefield is transformed into Impedance, multiplied by the Fourier component of the current and then transformed back to the time domain to get the voltages for each grid point. In order to obtain the kicks for each macro-particle, linear interpolation is applied between the grids. The resistive wall impedance was estimated by the low frequency formula

$$Z_{\perp}(\omega) = [1 - i\,\mathrm{sgn}(\omega)]\frac{Z_0 R\delta_{skin}}{b^3}\,, \qquad (5.8)$$

$$Z_{//}(\omega) = [1 - i\,\mathrm{sgn}(\omega)]\frac{Z_0\delta_{skin}}{2b}\frac{\omega}{\omega_0} \qquad (5.9)$$

, where $\delta_{skin} \equiv \sqrt{\frac{c}{Z_0 \sigma \omega}}$, $b \approx 3cm$ and $\sigma \approx 1.39 \times 10^6 \Omega^{-1} m^{-1}$ are the skin depth, radius and conductivity of the wall respectively. $Z_0 \equiv 377\Omega$ is the impedance of the free space, $R \approx 610m$ is the average radius of RHIC. The transverse space charge impedance was calculated by the following formula

$$Z_{\perp sc} = \frac{Z_0 R}{\beta^2 \gamma^2 a^2} \tag{5.10}$$

, where $a = 2\sigma_b$ is the radius of equivalent uniform beam. The impedance due to bellows and abort kicker are approximated by RLC resonant circuits model[15].

$$Z_{\perp BB} = \frac{R_{sh}}{1 + iQ\left(\frac{\omega_r}{\omega} - \frac{\omega}{\omega_r}\right)} \frac{\tilde{\omega}}{\omega} \tag{5.11}$$

, where $\tilde{\omega} = \omega_r \sqrt{1 - \frac{1}{4Q^2}}$ is the oscillation frequency of the wake field. The parameters of the considered broad band impedances are listed in Table 4. The inductive longitudinal impedance of

| | $Q$ | $R_{sh}(M\Omega \cdot m^{-1})$ | $f_r\ (MHz)$ |
|---|---|---|---|
| Bellows | 1.74 | 1.00 | $5.2 \times 10^3$ |
| Abort Kicker | 0.66 | 1.05 | 46.3 |

Table 5.1. Parameters for Transverse Broad Band Impedance

RHIC was measured to be $\frac{Z_{//}}{n} = 3j\Omega$[14]. In order to implement it into the simulation, longitudinal resonant model was assumed with test parameters $Q = 2$ and $f_r = 2GHz$.

$$Z_{//BB} = \frac{R_{sh}}{1 + iQ\left(\frac{\omega_r}{\omega} - \frac{\omega}{\omega_r}\right)}. \tag{5.12}$$

The shunt impedance is determined by requiring equation (5.5.12) giving the measured $3\,j\Omega$ at the low frequency limit.

$$R_{sh} = iQ\frac{Z_{//}}{n}\frac{\omega_r}{\omega_{rev}} \approx 1.53\times 10^5\,\Omega. \tag{5.13}$$

Since the beam distribution in the frequency domain is below $0.5GHz$, the simulation was not sensitive to the test parameters. The impedance from the BPMs are approximated by the following form

$$Z_{\perp bpm}(\omega) = \frac{R_{sh}}{i\frac{\omega}{\alpha_r} - 1} \tag{5.14}$$

, where $R_{sh} = 9.17\times 10^5\,\Omega\cdot m^{-1}$ and $\alpha_r = 6.54\times 10^8\,s^{-1}$. It corresponds to an exponentially decay wake in the time domain and gives a smoother impedance in the frequency domain as shown in Figure 5.1 (a). The longitudinal and transverse impedance are plotted in Figure 5.1. $M_{ecool}$ in equation (5.5.3) is due to the long range interaction with the electron cooling beam. For non-magnetized electron cooling[16],

$$\begin{aligned} M_{ecool}\begin{pmatrix} x \\ p_x \end{pmatrix} = &\begin{pmatrix} \xi_{ie}(\cos\psi_{coh} - 1) + 1 & \frac{1}{k_{coh}}\left[\xi_{ie}\sin\psi_{coh} + (1-\xi_{ie})\psi_{coh}\right] \\ -\xi_{ie}k_{coh}\sin\psi_{coh} & \xi_{ie}(\cos\psi_{coh} - 1) + 1 \end{pmatrix}\begin{pmatrix} \langle x\rangle \\ \langle p_x\rangle \end{pmatrix} \\ &+\begin{pmatrix} \cos\psi_{inc} & \frac{1}{k_{inc}}\sin\psi_{inc} \\ -k_{inc}\sin\psi_{inc} & \cos\psi_{inc} \end{pmatrix}\begin{pmatrix} x - \langle x\rangle \\ p_x - \langle p_x\rangle \end{pmatrix} \end{aligned} \tag{5.15}$$

, where $\xi_{ie} \equiv \left(\frac{k_{inc}}{k_{coh}}\right)^2$. The coherent and incoherent wave number of the interaction are defined as

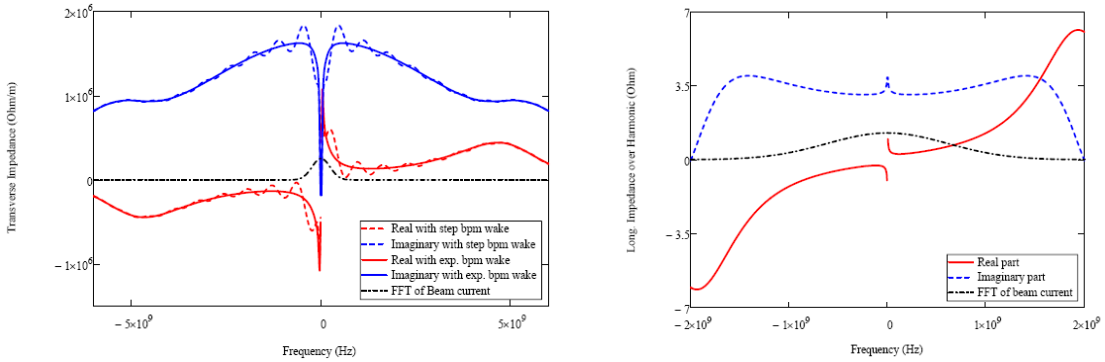


(a) (b)

Figure 5.1 Impedance Used for RHIC Instability Simulation. (a) Transverse Impedance used for RHIC simulation. The red solid curve is the real part of the transverse impedance and the solid blue curve is the imaginary part of the transverse impedance. The dot blue and dot red shows the impedance when step form for BPMs wake being applied. The black dash-dot curve shows the beam distribution. (b) Longitudinal Impedance used in RHIC simulation. The red solid curve and the blue dash curve are the real and imaginary parts of the longitudinal impedance over n respectively. The brown dash-dot curve shows the equivalent Gaussian beam distribution in the frequency domain.

$$k_{inc} = \frac{1}{\beta c}\sqrt{\frac{Z_i e^2}{2\varepsilon_0 \gamma^3}\frac{n_e}{M_i}}, \tag{5.16}$$

$$k_{coh} = \frac{1}{\beta c}\sqrt{\frac{Z_i e^2}{2\varepsilon_0 \gamma^3}\left(\frac{n_e}{M_i}+\frac{n_i}{m_e}\right)}. \tag{5.17}$$

Accordingly, the coherent and incoherent phases advance over the cooling section are given by $\psi_{coh} \equiv k_{coh} l_{cool}$ and $\psi_{inc} \equiv k_{inc} l_{cool}$.

### *5.2 Simulation Results*

Since the rf voltage and harmonic number were kept the same for all simulations, the momentum spread was always proportional to the bunch length. In order to investigate the momentum spread threshold of overcooling, the initial bunch length was gradually reduced from its current operational value $\sigma_s \approx 20cm$ until either longitudinal or transverse instability was observed. Table 5 shows the beam parameters we used for the simulation. About $10^5$ macro-particles were tracked during the simulation. The initial longitudinal distribution was parabolic and the initial rf voltage was linear. The beam was

| | |
|---|---|
| Beam Energy $\gamma$ | 100 |
| Beam Particle | $Au^{79+}$ |
| Transverse rms Emittance $\varepsilon_x (\pi \cdot mm \cdot mrad)$ | 4.2 |
| Bunch Population | $10^9$ |
| RF Voltage (MV) | 3 |
| RF Harmonic number | 2520 |
| Chromaticity $\xi_x$ | 2 |

Table 5.2 Parameters for RHIC coherent instability simulation

adiabatically matched to a sinusoidal rf voltage within 1000 turns. As shown in Figure 5.2 (a), for initial $\delta p / p \le 1.4 \times 10^{-4}$ the longitudinal emittance started to grow rapidly. After a few hundreds turns, the momentum spread increased well above the stability threshold and the growth was suppressed as the beam reached to its new equilibrium. Figure 5.2 (b) shows the longitudinal beam profile after 5000 turns. As one can see the

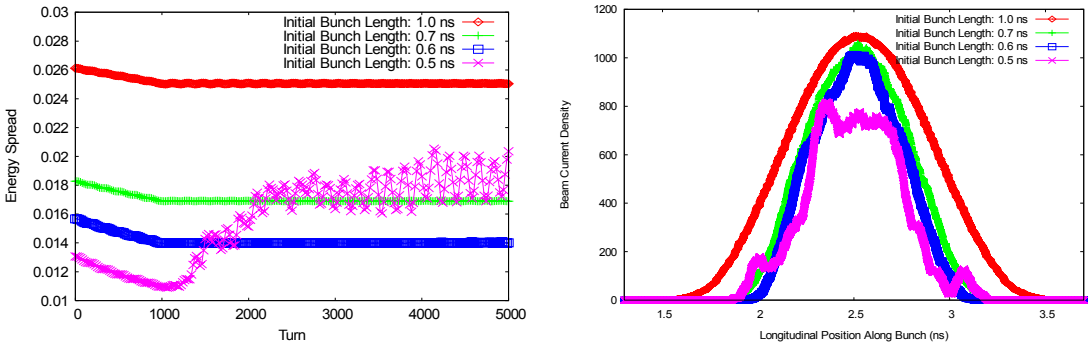


(a) (b)

Figure 5.2 (a) Momentum spread evolution for chromaticity $\xi_x = 2$. The abscissa is the number of turns being simulated and the ordinate is the momentum spread $\delta p / p$ in unit of $\gamma$. The decreasing before 1000 turn is due to the mismatch of the longitudinal phase space. Each curve has different initial bunch length and momentum spread as shown; (b) Longitudinal beam profiles after 5000 turns. Each curve shows the longitudinal beam profile for corresponding curve in Figure 5.2(a). The abscissa is longitudinal position along the bunch and the ordinate is the macro-particle density.

coherent oscillation was still pretty strong although it was not growing anymore. There were no transverse coherent oscillation growths observed for $10^9$ ions per bunch and $\xi_x = 2$ as shown in Figure 5.3. The coherence of a bunch is defined as the following

$$coherence = \frac{\int I(t)\left(\langle x \rangle^2 + \langle p_x \rangle^2\right) dt}{\int I(t) dt} \tag{5.18}$$

, where $\langle x \rangle$ and $\langle p_x \rangle$ are the average position and transverse angle for the slice $[t, t+dt]$ and the integration is over the whole bunch. From Figure 5.2 and Figure 5.3, we see that the longitudinal microwave instability happens before the transverse instability for the current operational parameters. The instability threshold was found to be $\sigma_{p,sim} \approx 1.4 \times 10^{-4}$, which is a factor of 3 smaller than the current momentum spread.

During the simulation, the longitudinal oscillation built up very fast (less than 100 turns) and the wavelengths of the perturbation were usually smaller than the bunch length. Since the synchrotron oscillation was slower than the coherent oscillation growth rate, the dispersion relation for a coasting beam should be able to estimate the instability threshold. For the parabolic distributed beam, the dispersion relation is[17]

$$\frac{Z_{//}(\omega)}{n} = \left[ i\Lambda_{//} \int_{-1}^{1} \frac{x}{x + x_1} dx \right]^{-1} \tag{5.19}$$

, where $\Lambda_{//} = \frac{3Z_i e I_{peak}}{2\pi\eta m_i c^2 \gamma_0 \beta_0^2 (\delta p / p)^2_{FWHH}}$ and $x_1 = \frac{\sqrt{2}\Delta\omega_{//}}{n\omega_0 |\eta| (\delta p / p)_{FWHH}}$. $(\delta p / p)_{FWHH}$ is the full width half height of the momentum spread which is related to the rms momentum spread by $\sigma_p = \frac{(\delta p / p)_{FWHH}}{2\sqrt{2\ln 2}}$ and $\Delta\omega_{//}$ is the complex coherent tune shift. The solution of Equation (5.19) is plotted into the impedance plane as shown in Figure 5.4. The instability threshold can be determined by the Keil-Schnell criteria

$$\sigma_{p,th} = \sqrt{\frac{(Z_{//}/n) I_{peak} Z_i e}{(2\ln 2) m_i c^2 \gamma_0 \beta_0^2 |\eta|}} = 1.5 \times 10^{-4}. \tag{5.20}$$

In the calculation of Equation (5.20), we used the peak current directly obtained from the simulation, $I_{peak} \approx 18A$. Comparing Equation (5.20) with the simulation results, we see that the agreement is within 10%. Since the chromaticity was set to 2, the rigid head-tail mode ($\mu = 0$) was damped. As we can see from Fig. 5.3 (a), when the chromaticity was set to negative, the head-tail instability took place and the growth rate was proportional to the absolute value of the chromaticity as expected from theory. Because of the non-linear

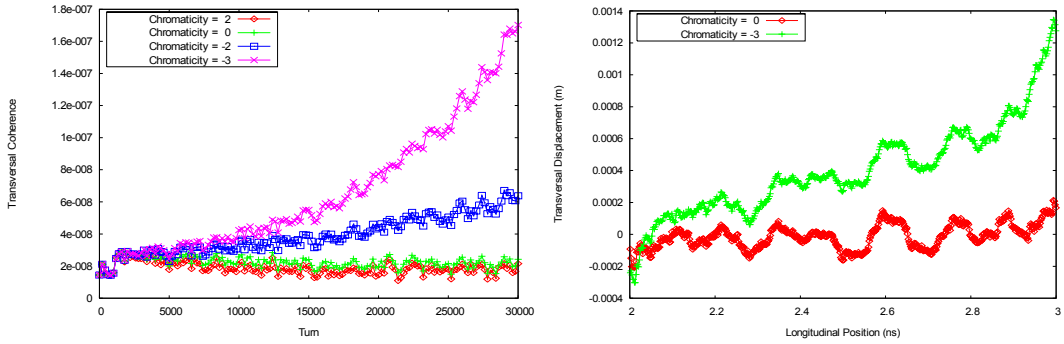


(a) (b)

Figure 5.3 (a) The transverse coherence evolution for varies chromaticity. The red and green curves are for $\xi_x = 0, 2$ respectively. The blue and purple curves are for $\xi_x = -2$ and $\xi_x = -3$. The abscissa is the simulation time in unit of turns and the ordinate is the coherence as defined in equation (5.18); (b) The side view of the beam after 5000 turns. The abscissa is the longitudinal position along the beam in unit of seconds and the ordinate is the transverse displacement in units of meter. The red curve is for $\xi_x = 0$ and the green curve is for $\xi_x = -3$.

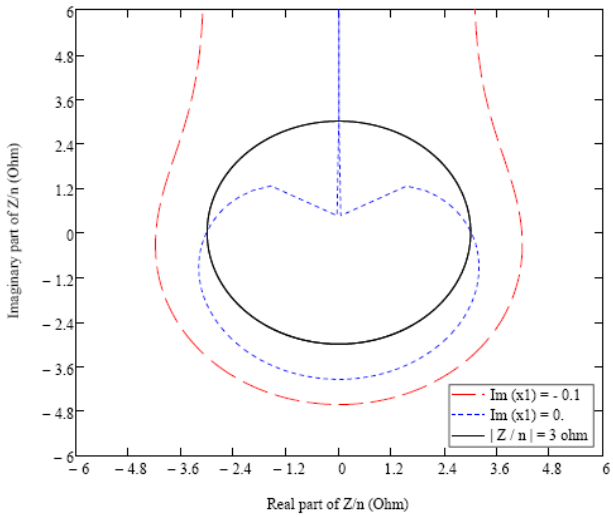


Figure 5.4 The growth rate contour in the normalized impedance plane for $\sigma_p = 1.7 \times 10^{-4}$. The abscissa and ordinate are $\mathrm{Re}(Z_{//}/n)$ and $\mathrm{Im}(Z_{//}/n)$ respectively. The red dash curve is the contour for $\mathrm{Im}(x_1) = -0.1$ and the blue dot line is the instability threshold contour. The black solid circle is for $|Z_{//}/n| = 3ohm$.

component of the rf voltage and the wake field, the higher order head-tail modes were actually landau damped by the synchrotron tune spread. As the number of particle inside the bunch increasing, the landau damping would eventually cease and for weak coupling and short bunch, the threshold can be estimated by the following dispersion relation[18]

$$Z_{eff} = \left[ i \frac{ecI_{av}}{2E\omega_y} \left( \frac{1}{2^{|\mu|}|\mu|!} \right)^{2|\mu|} \left( \frac{2\eta}{\beta_0^2 E_0} \right)^{|\mu|} \int_0^\infty dH_s \left( \frac{H_s}{\nu_s(H_s)^2} \right)^{|\mu|} \frac{\psi_0(H_s)}{(Q_R - \mu\nu_s(H_s) + iQ_I)} \right]^{-1} \quad (5.21)$$

, where $Q \equiv Q_R + iQ_I = \frac{\Omega + \omega_y}{\omega_0}$ is the coherent tune shift and the longitudinal synchrotron oscillation Hamiltonian is defined as

$$H_s \equiv \frac{1}{2} \left( \frac{e\omega_0 \left| V_{rf} \cos(\varphi_s) \right|}{2\pi E_0 \beta_0^2} (\varphi - \varphi_s)^2 + h\omega_0 \eta \delta^2 \right) \cdot \frac{E_0 \beta_0^2}{h\omega_0}. \quad (5.22)$$

The effective impedance $Z_{eff}$ is defined as

$$Z_{eff} \equiv \sum_{n=-\infty}^{\infty} \left( n - Q_y + \frac{\xi_x}{\eta} Q_y \right)^{2|\mu|} Z(n\omega_0 - \omega_y + \mu\omega_{s0}). \quad (5.23)$$

The simulation result for $\xi_x = 2$ is shown in Fig. 5.5. As the bunch population going beyond $5 \times 10^9$, the transverse motion became unstable and the growth rates were in order of $10^{-5}$ per turn, which is consistent with the solution of dispersion relation as shown in Figure 5.6 (a). Figure 5.5 indicates that the unstable mode is for $m = 1, \mu = 1$ head-tail mode and the threshold for the instability should be between $n_p = 4 \times 10^9$ and $n_p = 5 \times 10^9$. Numerical solutions of the dispersion relation, equation (5.21), are shown in Figure 5.6 (a). As shown in Figure 5.6 (b), the instability threshold prediction from the dispersion relation is $n_p \approx 3.5 \times 10^9$, which agrees with the simulation result within 30%. When the

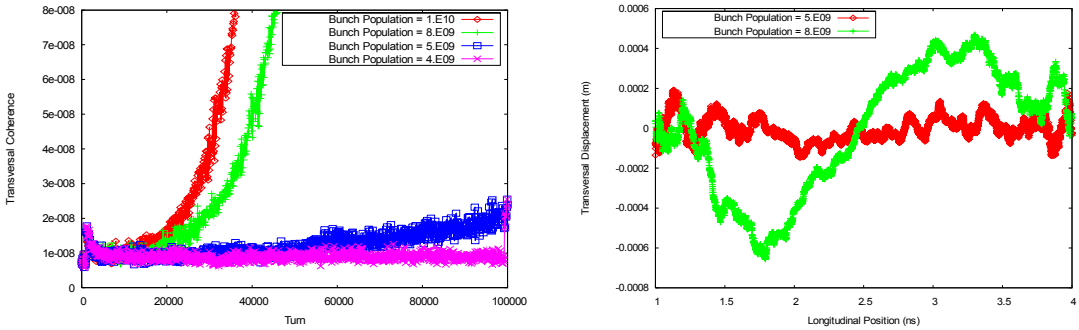


(a) (b)

Figure 5.5 (a) The transverse coherence evolution for $\mu = 1$ Head-tail mode. The abscissa is simulation time in unit of turns and the ordinate is the coherence as defined in Equation (5.18). The red green blue and purple curve are for bunch population of $10^{10}, 8\times10^{9}, 5\times10^{9}$ and $4\times10^{9}$ respectively. (b) A snapshot of the transverse displacement along the bunch. The red and green curves are for $8\times10^{9}$ and $5\times10^{9}$ ions per bunch. The green curve is taken after $10^{5}$ turns and red is taken after $5\times10^{4}$ turns.

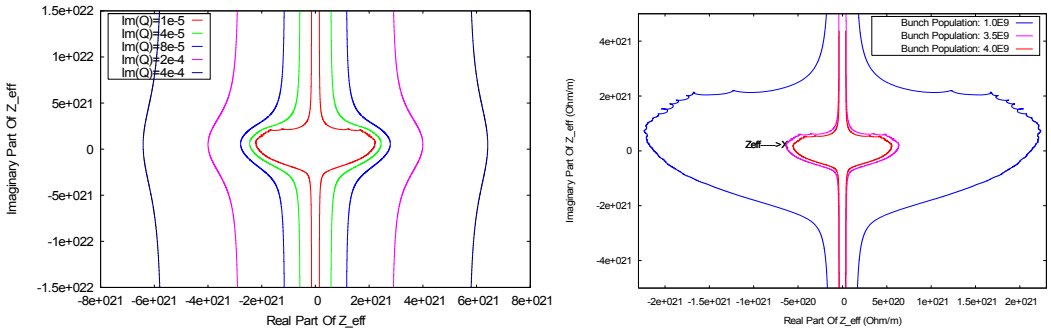


(a) (b)

Figure 5.6 (a) Coherent tune shift contours for $\mu = 1$ Head-tail mode. The abscissa and the ordinate are the real and imaginary part of the effective impedance in Equation (5.5.22). The bunch population is $5\times10^{9}$ and each curve corresponds to a specific growth rate; (b) Stability threshold contours for $\mu = 1$ Head-tail mode. The blue, purple and red curve are the stability threshold contours for bunch population of, $10^{9}, 3.5\times10^{9}$ and $4\times10^{9}$ respectively. The 'X' marks the value calculated directly from the definition, Equation (5.5.23), using the impedance shown in Figure 4.6.

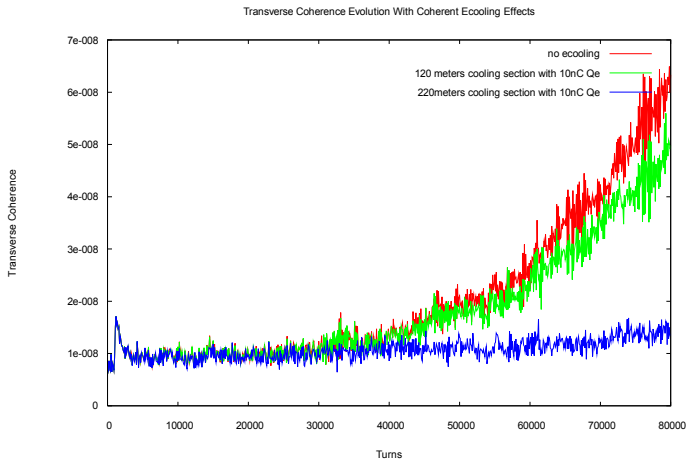


(a)

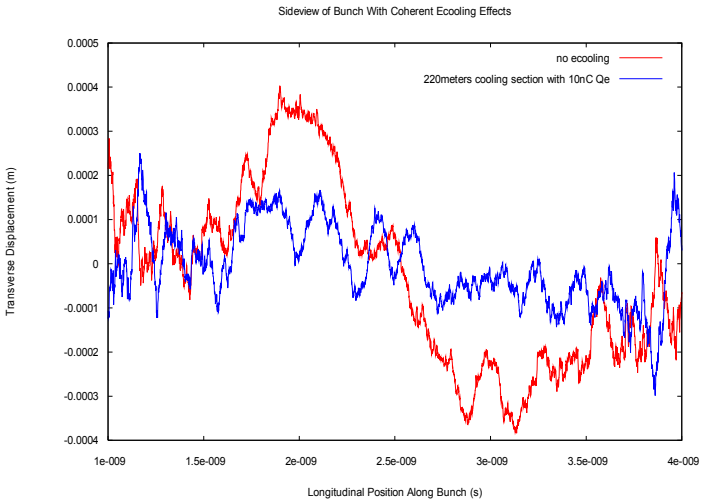


( b)

Figure 5.7 (a) The Transverse Coherence Evolution With Varies E-cooling Parameters. The bunch population is $6\times10^9$ and the chromaticity is 2. (b) The Side View of The Bunch After $8\times10^4$ turns. The abscissa is the coherent transverse angle multiplied by the average Beta function and the ordinate is the longitudinal position along the bunch.

beam is stable, the usually weak coherent interaction between electron cooling beam and ion beam does not play any role except for a tiny coherent tune shift. However, the slow

higher order head-tail instability growth could be suppressed by the coherent force exerted by the electron beam. As shown in Figure 5.7, the coherent damping effect of the electron beam is small for the current electron cooler design but can be increased dramatically by increase the cooling section length since the damping rate is proportional to $l_{ecool}^{4}$. In addition to the stability problems, having more particles within the bunch would increase the IBS rate and thus cause the emittance deterioration, which also require higher electron charge and longer cooling section.

### *5.3 Conclusion*

The single bunch simulation shows that the longitudinal microwave instability threshold can be accurately estimated by the coasting beam formula and for the current operational beam parameters, the threshold was found to be $\delta p / p \approx 1.5 \times 10^{-4}$. The transverse motion is stable for $\xi_x = 2$ and $n_p \le 4 \times 10^9$. High order head tail instability will occur if the bunch population is beyond the Landau damping threshold determined by the synchrotron frequency spread. The growth rate of $\mu = 1$ head tail mode is in the order of $10^{-5} \sim 10^{-4}$. This slow growth can be suppressed by the coherent force exerted by the cooling electron beam and in order to increase the head-tail threshold substantially, the length of the cooling section has to be at least 200 meters.

# CHAPTER 6. COHERENT ELECTRON COOLING

## *6.1 Basic Concept of CEC*

The coherent electron cooling is to use the electron beam as both the picking up and kicker devices to cool the ion beam stochastically[7]. Similar to the traditional stochastic cooling, the CEC can be described as correcting the beam center schottky noise or equivalently correct each individual ion. As shown in Fig 6.1 (a), the schottky noise of the ion beam center will modulate the electron beam density through the space charge field in the modulation section. Then the electron beam density variations are amplified by going through a section where the longitudinal beam instability taking place. Finally, the amplified electron beam field interacts with the ion beam and the ion beam center is corrected. Since

$$E\left(\langle \Delta p \rangle^2\right) = \frac{\langle \Delta p^2 \rangle}{N_s},$$

the energy spread is decreased as the beam center is corrected turn by turn. This process can also be understood from the point view of a single ion as shown in Fig 6.1 (b). Considering an ion moving inside the electron beam, the electrons will rearrange themselves and forms an electron cloud around the ion. The electron cloud density is then amplified through the amplification section and meets the same ion in the correction

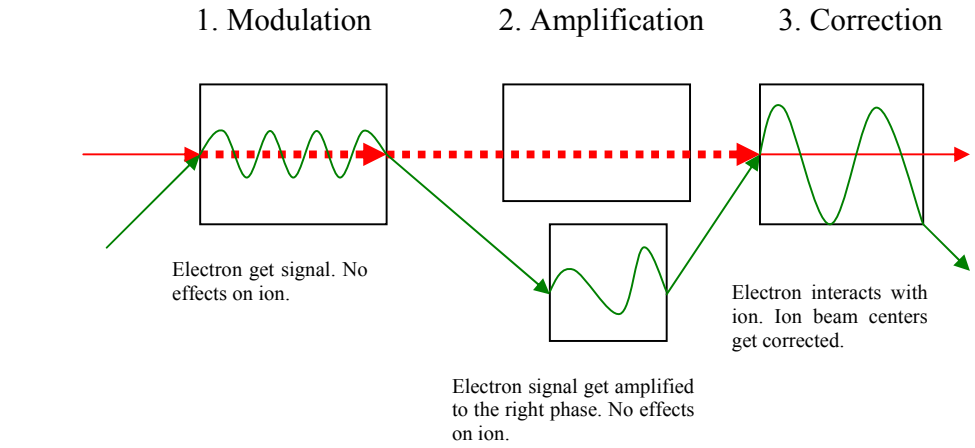


(a)

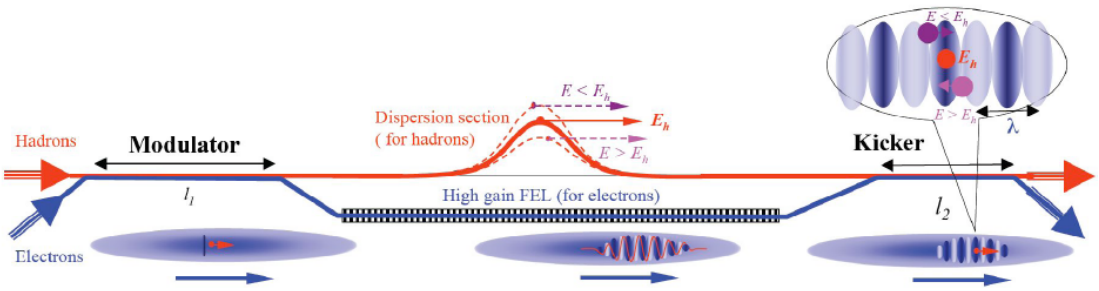


(b)

Figure 6.1 (a) Schematic demonstration of the CEC set up: Schottky signal description. (b) Schematic demonstration of the CEC set up: particle description (Taken from [19]).

section. The location of the ion with respect to the electron cloud can be adjusted according to its energy through a dispersive section such that the electron cloud always corrects its energy in the right direction. The effect from the electron cloud induced by the ion itself added coherently while the effects from the electron clouds induced by other

ions added incoherently. As a result, the ion's energy is corrected after many turns and the energy spread of the beam is reduced.

The content of this chapter is arranged as the following. In section 6.2, the modulation process is studied analytically for various electron velocity distributions. It is shown that analytic formula can be found for electron beam thermal distributions being Lorentzian. For the Gaussian distribution, numerical solution is presented and compared with the analytic solution. Section 6.3 shows an analytical approach of describing the amplification process using the 1D FEL theories and Lorentzian energy distribution. Both the energy spread and the space charge are naturally included into the formulation and their effects are shown.

### *6.2 Ion Shielding In An Anisotropic Electron Plasma*

Being an elementary subject of plasma physics as early as 1960s', the shielding effects of anisotropic plasma to moving ions become more interesting recently due to the new concept of beam cooling, the Coherent Electron Cooling. As an effective way of significantly increasing the luminosity of modern accelerators, CEC was proposed by Ya. S. Derbenev in 1980 [7] and has recently been discussed by V. N. Litvinenko[8]. The first process of CEC, modulating the electron beam, is realized by ion shielding, i.e. the electron density response to moving ions. A few facts make the well established asymptotic theory for slow moving ions [20-22] inapplicable to the process. Firstly, since

the proposed interaction time of the modulation is only $1/4$ of the plasma oscillation, the transient effects could not be sufficiently Landau damped and hence the system has not reached its equilibrium yet. Secondly, the electron beam has very different longitudinal and transversal thermal temperatures which make it an anisotropic system. Lastly, as the thermal velocity of the ions is comparable to that of the electrons, the solution should also apply to ions with $v_i \approx \sqrt{\langle v_e^2 \rangle}$. As a result, a more generally applicable dynamical description of the ion shielding in anisotropic non-equilibrium plasma is needed to understand the physics of the modulation and estimate its efficiency. By solving the self-consistent Vlasov-Poisson equations in the time domain, the exact analytic solution is found for the Lorenzian plasma[12]. For a rest ion, the analytic solution reduces to the well known Debye screening formula at $t \to \infty$. In order to investigate the validity of the analytic formula, the thermal assumption is then investigated by being compared with the numerical solution of the Maxwellian plasma.

The content is organized as the following. In section 6.4.1, it is shown that the linear Vlasov-Poisson equations are equivalent to an integral equation in time domain. In section 6.4.2, the analytic solution is derived for two different types of thermal distributions, the 2nd power and 3rd power of Lorenzian distribution. In section 6.4.3, the numerical solution for the Maxellian plasma is presented and compared with the analytic solutions. It is shown that the 3rd power of Lorenzian distribution agrees better with the numerical result and gives qualitatively correct dependence of damping rate and plasma frequency on wavelength, especially at long wavelength region. We will also show that

[12] The Lorenzian plasma refers to plasma with powers of Lorenzian form thermal distributions.

the response of anisotropic plasma to a rest ion decays exponentially with distance as long as the thermal distribution of the plasma has elliptical symmetry. The summary is made in section 6.4.4.

### 6.2.1 Vlasov-Poisson Equations

The dynamics of collisionless electron plasma is described by the Vlasov equation and Maxwell equations. If the variation of the plasma density is small compared to its equilibrium background, one may ignore the higher order terms and describe the system with linearized Vlasov equation.

$$\frac{\partial}{\partial t} f_1(\vec{x},\vec{v},t) + \vec{v} \cdot \frac{\partial}{\partial \vec{x}} f_1(\vec{x},\vec{v},t) - \frac{e\vec{E}}{m_e} \frac{\partial}{\partial \vec{v}} f_0(\vec{v}) = 0, \tag{6.1}$$

where $f_1(\vec{x},\vec{v},t)$ is the perturbation of electron density in the phase space and $f_0(\vec{v})$ is the thermal velocity distribution of the background which has uniform spatial distribution. Assuming the thermal velocity of the electrons and ions are small compared with the speed of light, the magnetic field may also be ignored, which reduces the Maxwell equations to Poisson equation

$$\vec{\nabla} \cdot \vec{E} = \frac{\rho_{ind}(\vec{x},t) + \rho_{ext}(\vec{x},t)}{\varepsilon_o}. \tag{6.2}$$

Considering the external electric field is caused by a moving ion with velocity $\vec{v}_0$, the charge density in equation (6.2) is given by

$$\rho(\vec{x},t) = Ze\delta(\vec{x}) - \tilde{n}_1 e(\vec{x},t), \tag{6.3}$$

where $\tilde{n}_1(\vec{x},t) \equiv \int f_1(\vec{x},\vec{v},t)d\vec{v}$ . Equation (6.1)-(6.3) form a self-consistent description of the electron plasma driven by a moving ion, which are then Fourier transformed into the wave vector space as

$$\frac{\partial}{\partial t} f_1(\vec{k},\vec{v},t) + i\vec{k}\cdot\vec{v} f_1(\vec{x},\vec{v},t) + i\frac{e}{m_e}\Phi(\vec{k},t)\cdot\left(\vec{k}\cdot\frac{\partial}{\partial\vec{v}} f_0(\vec{v})\right) = 0 \tag{6.4}$$

,

where

$$\Phi(\vec{k},t) = \frac{e}{\varepsilon_o k^2}\left[Z_i - \tilde{n}_1(\vec{k},t)\right] \tag{6.5}$$

is the Fourier component of the electric potential. Integrating (6.4) over the 3 dimension electron velocities and assuming the zero initial conditions of the electron density perturbation, $\tilde{f}_1(\vec{k},0) = 0$ and $\frac{d}{dt}\tilde{f}_1(\vec{k},0) = 0$, one finally gets an integral equation in the wave vector space[23, 24]

$$\tilde{n}_1(\vec{k},t) = \omega_p^2 \int_0^t \left[\tilde{n}_1(\vec{k},t_1) - Z_i\right](t_1 - t) g\left(\vec{k}(t_1 - t)\right) dt_1, \tag{6.6}$$

where

$$g(\vec{u}) = \frac{1}{n_0}\int f_0(\vec{x},\vec{v},t) e^{i\vec{u}\cdot(\vec{v}_0 - \vec{v})} d^3v . \tag{6.7}$$

In order to make any further analytical progresses, specific choices of the electron thermal distribution have to be made such that equation (6.6) is analytically solvable.

### 6.2.2 The 2nd Power of Lorenzian Distribution

Considering the electron plasma having the following thermal velocity distribution,

$$f_0(\vec{v}) = \frac{n_0}{\pi^2 \beta_x \beta_y \beta_z} \left( 1 + \frac{(v_x + v_{0x})^2}{\beta_x^2} + \frac{(v_y + v_{0y})^2}{\beta_y^2} + \frac{(v_z + v_{0z})^2}{\beta_z^2} \right)^{-2}, \tag{6.8}$$

where $\beta_{x,y,z}$ are the parameters describing the 3 dimensional temperatures of the plasma and $\vec{v}_0$ is the ion's velocity with respect to the electron plasma. The distribution (6.8) is normalized to unity and is essentially the 2nd power of Lorenzian distribution. Its Fourier transformation is given by

$$g(\vec{u}) = e^{i\vec{u}\cdot\vec{v}_0 - \sqrt{(u_x\beta_x)^2 + (u_y\beta_y)^2 + (u_z\beta_z)^2}}. \tag{6.9}$$

Inserting (6.9) into (6.6) and multiply both sides of the equation by a common factor $e^{-\lambda(\vec{k})t}$, one gets

$$\tilde{H}_1(\vec{k},t) = \omega_p^2 \int_0^t (t_1 - t) \left[ \tilde{H}_1(\vec{k},t_1) - Z_i e^{-\lambda(\vec{k})t_1} \right] dt_1, \tag{6.10}$$

where

$$\lambda(\vec{k}) \equiv i\vec{k}\cdot\vec{v}_0 - \sqrt{(k_x\beta_x)^2 + (k_y\beta_y)^2 + (k_z\beta_z)^2}, \tag{6.11}$$

and

$$\tilde{H}_1(\vec{k},t) \equiv \tilde{n}_1(\vec{k},t) e^{-\lambda(\vec{k})t}. \tag{6.12}$$

Taking secondary time derivative for both sides of (6.10), one gets the following inhomogeneous secondary ODE with constant coefficients

$$\ddot{\tilde{H}}_1(\vec{k},t) = -\omega_p^2 \tilde{H}_1(\vec{k},t) + \omega_p^2 Z_i e^{-\lambda(\vec{k})t}. \tag{6.13}$$

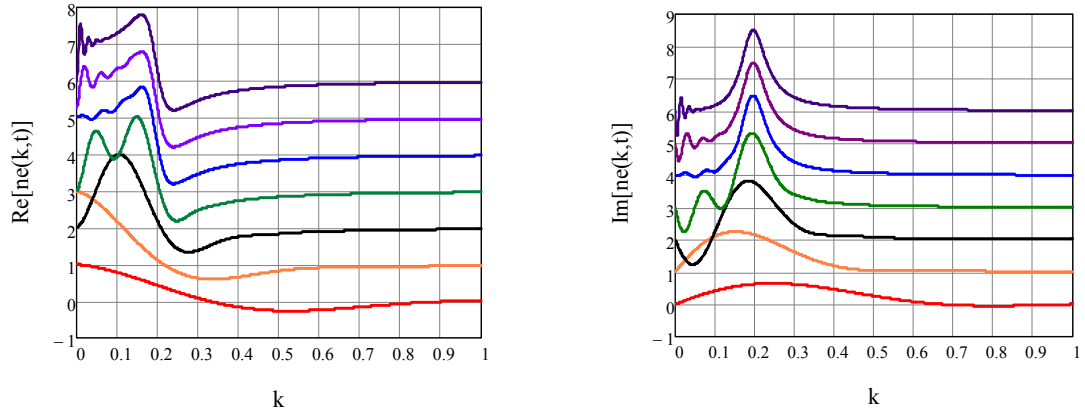


Figure 6.2 Mountain Range Plot for the electron response $\tilde{n}_e(\vec{k},t)$ as a function of the wavelength and time. The graph is for the ion velocity along the wave vector $\vec{k}$ .

The solution of (6.13) is composed of the homogeneous oscillation parts and the exponential part from the inhomogeneous term. After considering the zero initial conditions, $\tilde{n}_1(\vec{k},0)=0$ and $\dot{\tilde{n}}_1(\vec{k},0)=0$, the solution for $\tilde{n}_1(\vec{k},t)$ is ready to be obtained as

$$\tilde{n}_1(\vec{k},t)=\frac{\omega_p^2 Z_i}{\omega_p^2+\lambda(\vec{k})^2}\left\{1-e^{\lambda(\vec{k})t}\cdot\left[\cos(\omega_p t)-\frac{\lambda(\vec{k})}{\omega_p}\cdot\sin(\omega_p t)\right]\right\}. \qquad (6.14)$$

The second term in the bracket shows the transient plasma oscillation induced by the presence of the ion. The oscillation is Landau damped after a few plasma oscillations and only those with very long wavelength stays oscillating as shown in Fig. 6.2. The first derivative of (14) reads,

$$\dot{\tilde{n}}_1(\vec{k},t)=Z_i\omega_p\sin(\omega_p t)\exp(\lambda(\vec{k})\cdot t). \qquad (6.15)$$

Fourier inversion of (6.15) gives the time derivative of the electron density variation.

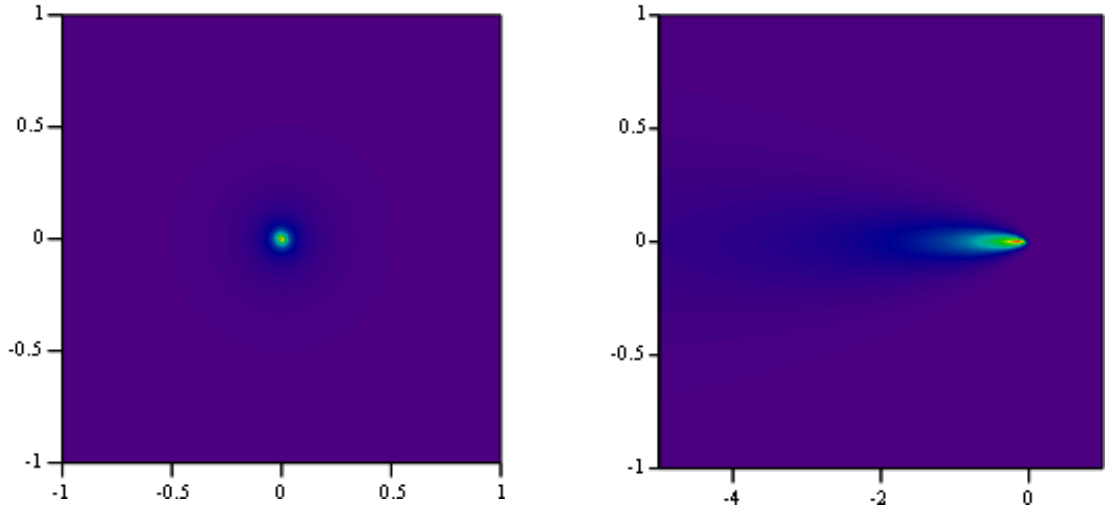


Figure 6.3 The Response of the 2nd Lorenzian plasma to an ion. The abscissa and ordinate is for normalized spatial x and y coordinates in units of their Debye radius. The left graph is for an rest ion and the right graph is for an ion with velocity $10\beta_z$. The snapshot is taken at $\psi = \pi$

$$\dot{\tilde{n}}_1(\vec{x},t) = \frac{Z_i}{\pi^2 r_{Dx} r_{Dy} r_{Dz}} \frac{\psi \sin(\psi) d\psi}{\left(\psi^2 + \left(\bar{x} + \bar{v}_{0x}\psi\right)^2 + \left(\bar{y} + \bar{v}_{0y}\psi\right)^2 + \left(\bar{z} + \bar{v}_{0z}\psi\right)^2\right)^2}, \qquad (6.16)$$

where the normalized variable are defined as $\psi = \omega_p t$, $r_{D,i} = \beta_i / \omega_p$, $\bar{x}_i = x_i / r_{D,i}$ and $\bar{v}_{0i} = v_{0i} / \beta_i$. Integrating (6.16) over time and taking into account the initial condition, one gets the electron density variation as the following

$$\tilde{n}_1(\vec{x},t) = \frac{Z_i}{\pi^2 r_{Dx} r_{Dy} r_{Dz}} \int_0^{\psi_1} \frac{\psi \sin(\psi) d\psi}{\left(\psi^2 + \left(\bar{x} + \bar{v}_{0x}\psi\right)^2 + \left(\bar{y} + \bar{v}_{0y}\psi\right)^2 + \left(\bar{z} + \bar{v}_{0z}\psi\right)^2\right)^2}. \qquad (6.17)$$

Equation (6.17) is essentially sum of a few sinusoidal integrals and no further significant simplification can be made analytically. Fig. 6.3 and Fig. 6.4 show the numerical integration result for (6.17). In Fig. 6.3, snapshots at $\psi = \pi$ are shown for a rest ion and a moving ion with $v_z = 10\beta_z$. In Fig. 6.4, a mountain range plot is shown for a moving ion

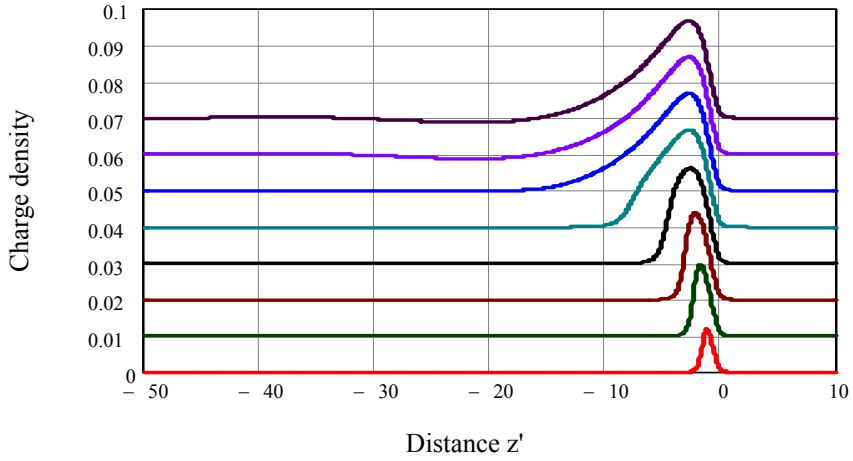


Figure 6.4. Mountain Range Plot for the electron response $\tilde{n}_e(\vec{x},t)$ as a function of the longitudinal location and time. The graph is taken at the transverse location $x = y = 0.3r_D$.

with $v_z = 5\beta_z$. In case of $\vec{v}_0 = 0$, and $t \to \infty$, equation (6.17) reduces to the following equilibrium solution,

$$\begin{aligned} \tilde{n}_1(\vec{x},t) &= \frac{Z_i}{\pi^2 r_{D,x} r_{D,y} r_{D,z}} \int_0^\infty \frac{\psi \sin(\psi) d\psi}{\left(\psi^2 + \bar{r}^2\right)^2} \\ &= \frac{Z_i}{4\pi r_{D,x} r_{D,y} r_{D,z}} \cdot \frac{1}{\bar{r}} \exp(-\bar{r}) \end{aligned}, \tag{6.18}$$

where $\bar{r} \equiv \sqrt{\left(x/r_{D,x}\right)^2 + \left(y/r_{D,y}\right)^2 + \left(z/r_{D,z}\right)^2}$. Equation (6.18) predicts that the electron response decays exponentially with distance. When the 3 temperatures in each direction are the same, equation (6.18) reproduces the well known Debye screening formula.

Figure 6.3(b) suggests that the charge distribution tends to concentrate in a smaller cone as the ion velocity gets bigger. This effect can be shown by integrating equation (6.17) over certain solid angle and radius as shown in Figure 6.5. The integration can be carried out analytically and expressed into the following form,

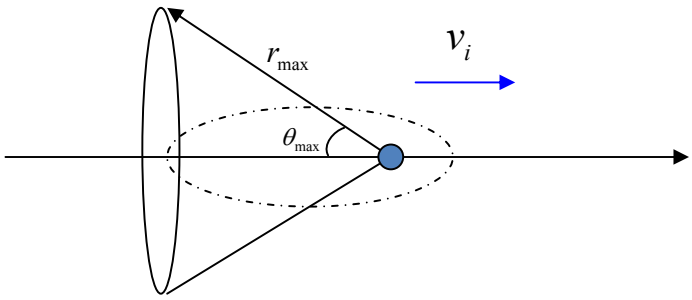


Figure 6.5. Integration volume (backward cone) of equation (6.19).

$$\begin{aligned}\widetilde{N}_1(\theta_{\max},\bar{r}_{\max},t) &= \iiint_{V_{cone}} \widetilde{n}_1(\vec{x},t)dxdydz \\ &= \frac{-2Z_i}{\pi r_{Dx}r_{Dy}r_{Dz}} \int_0^{\psi_1} \psi\sin(\psi)\left[I(\theta_{\max},\bar{r}_{\max},t) - I(0,\bar{r}_{\max},t)\right]d\psi\end{aligned} \tag{6.19}$$

, where

$$I(\theta_{\max},\bar{r}_{\max},t) \equiv \frac{i}{4\psi^2\bar{v}_{0z}\sqrt{1+\bar{v}_{0z}^2\sin^2\theta_{\max}}}\left[\bar{r}_- \ln\left(1-\frac{\bar{r}_{\max}}{\bar{r}_-}\right) - \bar{r}_+ \ln\left(1-\frac{\bar{r}_{\max}}{\bar{r}_+}\right)\right],$$

and

$$\bar{r}_\pm(\theta_{\max},t) \equiv \psi\left[\bar{v}_{0z}\cos\theta_{\max} \pm i\sqrt{1+\bar{v}_{0z}^2\sin^2\theta_{\max}}\right].$$

Figure 6.6 shows the numerical integration results of (6.19). In Figure 6.6(a) the total electron charge induced by an ion moving with velocity $v_i = \beta_e$ inside a sphere with radius $\bar{r}_{\max} = 2$ is plotted as a function of time. Reaching its maximum after $1/4 \sim 1/2$ plasma oscillations, the total induced charge around the ion almost keeps constant. The velocity effects to the charge distribution are plotted in Figure 6.6(b). For example, as the velocity increases to $5\beta_e$, 80% of the total induced charge are concentrated in the backward cone with $\theta_{\max} = \pi/5$

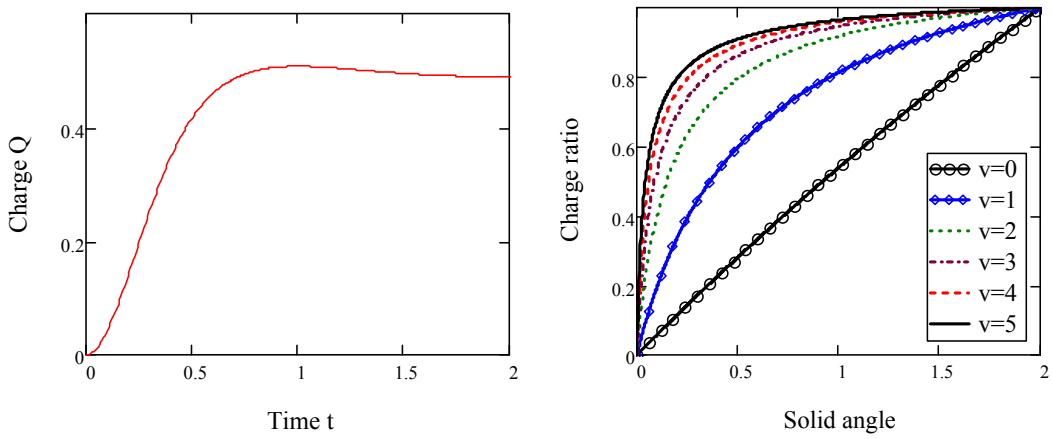


(a) (b)

Figure 6.6 Integrated electron charge induced by a moving ion inside certain solid angle and radius. (a) Total induced electron charge inside a sphere with radius $\bar{r}_{\max} = 2$ as a function of time; (b) Angular charge distribution. The abscissa is $\cos(\pi - \theta_{\max})$ and the ordinate is $\zeta(\theta_{\max}) \equiv \frac{\tilde{N}_1(\theta_{\max})}{\tilde{N}_1(\pi)}$ where the radial cutoff is $\bar{r}_{\max} = 5$ and the snapshot are taken at $\psi = 2\pi$.

One may notice that there are some drawbacks of the distribution (6.8). Although the plasma oscillation and Landau damping is described in eq.(6.14), the wavelength dependence of them are quite different from that of the Maxwellian plasma. Actually the distribution (6.8) does not even define the rms velocity spread. In order to obtain analytic results more realistic and closer to the Maxwellian plasma, the 3rd power of Lorenzian distribution is considered.

### 6.2.3 The 3rd Power of Lorenzian Distribution

The normalized velocity distribution of the 3rd power Lorenzian distribution reads

$$f(\vec{v}) = \frac{4n_0}{\pi^2 \beta_x \beta_y \beta_z} \left( 1 + \frac{(v_x + v_{0x})^2}{\beta_x^2} + \frac{(v_y + v_{0y})^2}{\beta_y^2} + \frac{(v_z + v_{0z})^2}{\beta_z^2} \right)^{-3}. \tag{6.20}$$

The Fourier transformation of (6.20) is

$$g(\vec{u}) = (1 + R(\vec{u}))\exp(-R(\vec{u})), \tag{6.21}$$

where $R(\vec{u}) = \sqrt{(u_x\beta_x)^2 + (u_y\beta_y)^2 + (u_z\beta_z)^2}$. Following the similar steps of the previous section, one obtains the following 3rd order ODE with constant coefficients

$$\tilde{H}_1'''(\psi) + \tilde{H}_1'(\psi) + 2\bar{k} \cdot \tilde{H}_1(\psi) = Z_i \bar{k}(3 - i\chi \cdot \bar{v}_0)\exp\left[(1 - i\chi \cdot \bar{v}_0)\bar{k} \cdot \psi\right], \tag{6.22}$$

where $\bar{k} = \sqrt{(k_x r_{D,x})^2 + (k_y r_{D,y})^2 + (k_z r_{D,z})^2}$, $\bar{v}_0 = \sqrt{(v_{0,x}/\beta_x)^2 + (v_{0,y}/\beta_y)^2 + (v_{0,z}/\beta_z)^2}$ and $\chi \equiv \vec{k} \cdot \vec{v}_0 / (\bar{k}\bar{v}_0)$.

In help of the initial conditions, $\tilde{H}(0) = \tilde{H}'(0) = 0$ and $\tilde{H}''(0) = Z_i$, equation (6.22) can be analytically solved and the electron density response in wave vector domain is

$$\tilde{n}_1(\vec{k}, t) = \frac{Z_i}{1 + \eta\lambda^2} \left\{ 1 + \tilde{c}_1 e^{-(\lambda + \gamma_0)\psi} - e^{-\left(\lambda - \frac{\gamma_0}{2}\right)\psi} \cdot \left[ (1 + \tilde{c}_1) \cdot \cos(\gamma_1 \psi) + \frac{\lambda}{\gamma_1} \left( 1 - \frac{\gamma_0}{2\lambda}(1 + 3\tilde{c}_1) \right) \cdot \sin(\gamma_1 \psi) \right] \right\}, \tag{6.23}$$

where $\lambda$ is defined in (6.11) and $\eta, \gamma_0, \gamma_1, \tilde{c}_1$ are functions of the wave vector defined as

$$\gamma_0(\bar{k}) \equiv (\sqrt{\bar{k}^2 + 1/27} + \bar{k})^{\frac{1}{3}} - (\sqrt{\bar{k}^2 + 1/27} - \bar{k})^{\frac{1}{3}},$$

$$\gamma_1(\bar{k}) \equiv \frac{\sqrt{3}}{2}[(\sqrt{\bar{k}^2 + 1/27} + \bar{k})^{\frac{1}{3}} + (\sqrt{\bar{k}^2 + 1/27} - \bar{k})^{\frac{1}{3}}],$$

$$\eta(\chi) \equiv 1 - \frac{2}{3 - i\chi \cdot \bar{v}_0}, \qquad \tilde{c}_1(\vec{k}) \equiv \frac{-\lambda^2 \cdot (1-\eta) - \gamma_0^2}{3 \cdot \gamma_0^2 + 1}.$$

Equation (6.23) has a few major differences compared with equation (6.14). Firstly, the plasma oscillation frequency is now a function of the wavelength. Secondly, the Landau damping rate is reduced especially at long wavelength since $\gamma_0$ is always a positive number and behaves as $\bar{k}^{1/3}$ at large $k$ while $\lambda(\vec{k})$ linearly depends on $k$. Thirdly, the factor $\eta$ appears in the factor outside the bracket, which is $1/3$ for $v_0 = 0$. This factor is important when one want to compare the results of different thermal distributions. Lastly, there is a fast damping term appears in the bracket and its damping is much faster compared to the Landau damping of the plasma oscillation. Fourier inversion of (6.23) is too complicated to be conducted analytically by hand. The numerical results will be shown in the following section where it is compared with the Maxwellian plasma and 2nd power Lorenzian plasma.

### 6.2.4 Numerical Result for Maxwellian Plasma and Comparison

Maxwellian plasma is the most considered and more realistic plasma compared to the Lorenzian plasma. The thermal velocity distribution of Maxwellian electron plasma is

$$f(\vec{v}) = \frac{n_0}{(2\pi)^{\frac{3}{2}} \sigma_x \sigma_y \sigma_z} \exp\left( -\frac{(v_x + v_{0x})^2}{2\sigma_x^2} - \frac{(v_y + v_{0y})^2}{2\sigma_y^2} - \frac{(v_z + v_{0z})^2}{2\sigma_z^2} \right). \tag{6.24}$$

Unlike Lorenzian plasma, it defines average value for any power of velocities and is naturally reached through collision process. Unfortunately, analytic approach for Maxwellian plasma dynamics is usually difficult. The solution of the integral equation (6.6) has to be found numerically. Since equation (6.6) has no singularity at $t = t_1$, the numerical solution is straightforward. After inserting equation (6.24) and carrying out the integral for the inhomogeneous part, equation (6.6) can be written as

$$\tilde{H}_1(\vec{k},\psi) = \int_0^{\psi} \tilde{H}_1(\vec{k},\tau)\cdot W(\psi-\tau)d\tau + g(\psi), \tag{6.25}$$

where

$$\tilde{H}_1(\vec{k},t) \equiv \tilde{n}_1(\vec{k},t)\exp(-i\vec{k}\cdot\vec{v}_0 t),$$

$$W(\tau) \equiv -\tau\cdot\exp\left(-\frac{1}{2}\bar{k}^2\cdot\tau^2\right),$$

and

$$g(\psi) = \frac{Z_i}{\bar{k}^2}\left\{e^{-i\bar{k}\bar{v}_0\chi\psi}\left(1+i\sqrt{\frac{\pi}{2}}\bar{v}_0\chi\cdot w\left(\frac{\bar{v}_0\chi}{\sqrt{2}}\right)\right) - e^{-\frac{1}{2}\bar{k}^2\psi^2}\left(1+i\sqrt{\frac{\pi}{2}}\bar{v}_0\chi\cdot w\left(i\sqrt{2}\bar{k}\psi+\frac{\bar{v}_0\chi}{\sqrt{2}}\right)\right)\right\}.$$

The variable $\chi$, $\bar{k}$ and $\bar{v}_0$ are already defined in equation (6.22) and $w(z)$ is the Faddeeva function defined as $w(z) = e^{-z^2}erfc(-iz)$. Equation (6.24) is the Volterra Equation of the second type which can be solved simply by iteration. Fig. 6.7 shows the responses of the 2nd Lorenzian, 3rd Lorenzian and Maxwellian plasma to an ion moving with velocities $\nu_0 = 0$, $\nu_0 = 0.5\sigma_e$, $\nu_0 = \sigma_s$ and $\nu_0 = 3\sigma_s$. It is clear that they exactly overlap with each other for $\nu_0 = 0$. Since the normalized variables are used in the calculations, Fig. 6.7 also describes the anisotropic plasmas. As shown in equation (6.18), the analytic black curve in Fig. 6.7 (a) is exponential decay, which suggests that the responses of the other

two plasmas to a rest ion also exponentially decay regardless of being isotropic or not. Actually as long as the thermal velocity distribution has elliptical symmetry, the response of the electron plasma to a rest ion always exponentially decays with the distance. This can be shown as the following. By making Laplace transformation of equation (6.4), the electron density response in $(\vec{k}, p)$ space can be written as

$$\tilde{n}_1\left(\vec{k}, p\right) = -i\frac{Z_i}{p}\cdot\frac{\frac{\omega_p^2}{k^2}\int\frac{\vec{k}\cdot\frac{\partial}{\partial\vec{v}}f_0\left(\vec{v}\right)}{p+i\vec{k}\cdot\vec{v}}d^3v}{1-i\frac{\omega_p^2}{k^2}\cdot\int\frac{\vec{k}\cdot\frac{\partial}{\partial\vec{v}}f_0\left(\vec{v}\right)}{p+i\vec{k}\cdot\vec{v}}d^3v}, \tag{6.26}$$

where

$$\tilde{n}_1(\vec{k}, p) = \int_0^\infty \tilde{n}_1(\vec{k}, t)e^{-pt}dt\ .$$

The electron response in the time domain is then given by inverse transforming (6.26) according to the following formula

$$\tilde{n}_1(\vec{k}, t) = \frac{1}{2\pi i}\int_{-i\infty+\sigma}^{i\infty+\sigma}\tilde{n}_1(\vec{k}, p)e^{pt}dp\ . \tag{6.27}$$

The integral in equation (6.27) is calculated by summing up all the residues at poles of $\tilde{n}_1(\vec{k}, p)$. All poles obtained from solving the dispersion relation

$$1-i\frac{\omega_p^2}{k^2}\cdot\int\frac{\vec{k}\cdot\frac{\partial}{\partial\vec{v}}f_0\left(\vec{v}\right)}{p+i\vec{k}\cdot\vec{v}}d^3v = 0\ , \tag{6.28}$$

go to zero with $t\to\infty$ and only the pole at $p=0$ survives at equilibrium. As a result, the electron response at equilibrium can be obtained by only calculating the residue at $p=0$.

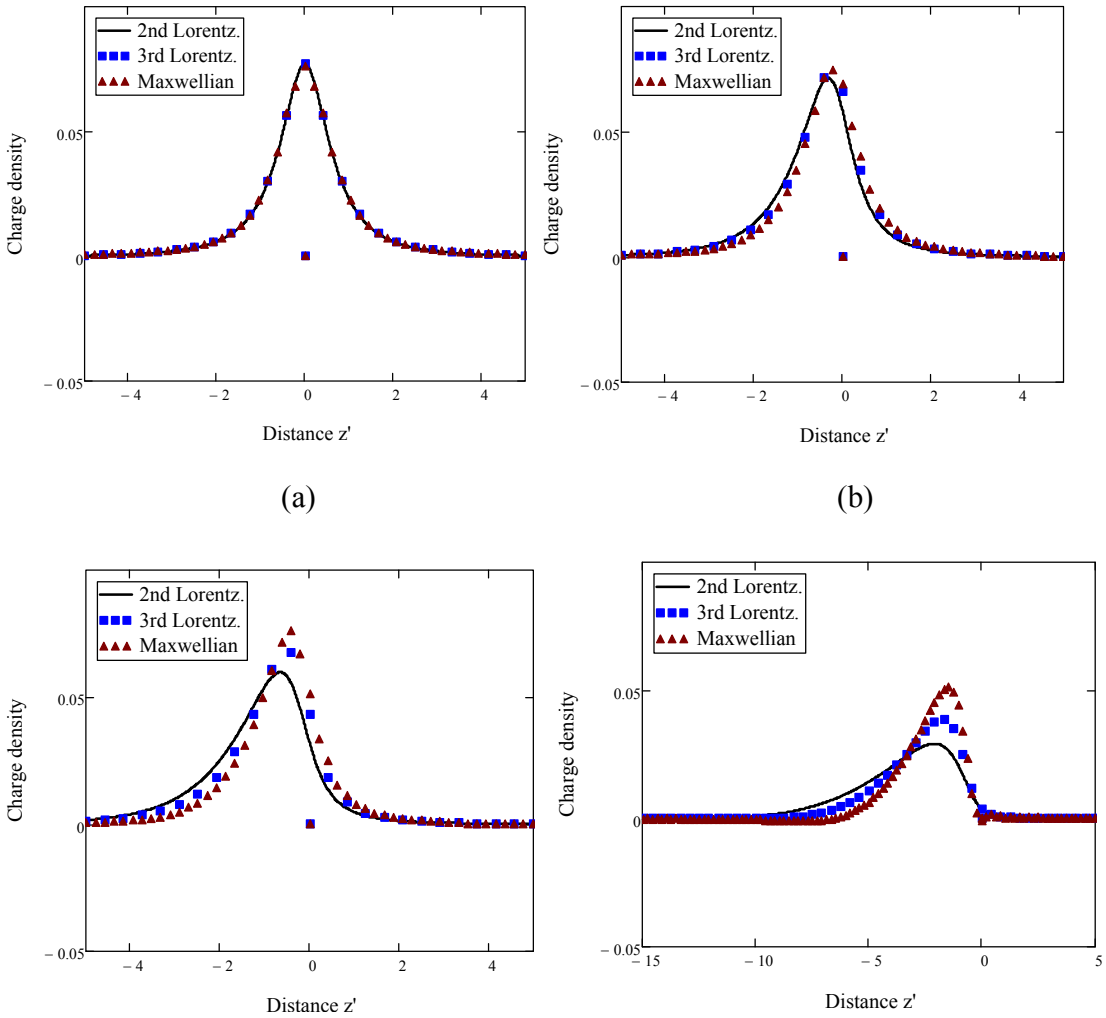


Figure 6.7 The Responses of Electron Plasmas to An Ion with Various Velocities. The abscissa is the longitudinal distance from the rest ion in units of longitudinal Debye radius and the ordinate is the electron density response multiplied by the Debye volume. The black solid curve is for the analytic solution of the 2nd Lorenzian plasma. The red triangles are for the 3rd Lorenzian plasma response and the blue crosses are for the Maxwellian plasma. The snapshot is taken at $\omega_p t = \pi$ .

Assuming the thermal velocity distribution of the electron plasma has elliptical symmetry, i.e.

$$f_0(\vec{v}) = f_0(\bar{v}),$$

where $\bar{v} = \left( \frac{v_x^2}{\beta_x^2} + \frac{v_y^2}{\beta_y^2} + \frac{v_z^2}{\beta_z^2} \right)^{1/2}$, the integral in equation (6.26) for $p = 0$ can be simplified to

$$\frac{\omega_p^2}{k^2} \int \frac{\vec{k} \cdot \frac{\partial}{\partial \vec{v}} f_0(\vec{v})}{i\vec{k} \cdot \vec{v}} d^3v = -\frac{4\pi\beta_x\beta_y\beta_z}{i\bar{k}^2} \int_0^\infty f_0(\bar{v}) d\bar{v} \,. \tag{6.29}$$

Inserting (6.29) into (6.26), one gets

$$\tilde{n}_1(\vec{k}, t \to \infty) = Z_i \cdot \frac{1}{1 + \eta \cdot \bar{k}^2}, \tag{6.30}$$

where $\eta \equiv \left( 4\pi\beta_x\beta_y\beta_z \int_0^\infty f_0(V) dV \right)^{-1}$. The inverse Fourier transformation of (6.30) generates

$$\tilde{n}_1(\vec{x}, t) = \frac{Z_i}{4\pi R_{D,x} R_{D,y} R_{D,z} \bar{R}} \exp(-\bar{R}), \tag{6.31}$$

where $R_{D,i} = \frac{\sqrt{\eta} \cdot \beta_i}{\omega_p}$ and $\bar{R} = \left( \frac{x^2}{R_{D,x}^2} + \frac{y^2}{R_{D,y}^2} + \frac{z^2}{R_{D,z}^2} \right)^{1/2}$. By calculating $\eta$ for all three thermal distributions and comparing the results with equation (6.14) and (6.23), it is verified that the formula of (6.30) is consistent with the previous calculations. Fig. 6.5 also suggests that for $v_0 \le \sigma_e$, both the 2nd power Lorenzian plasma and the 3rd power Lorenzian plasma behave similar to the Maxwellian plasma but the 3rd power Lorenzian plasma is apparently better than the 2nd power Lorenzian plasma. For $v_0$ being a few $\sigma_e$, the response of the Maxwellian plasma is more localized than the Lorenzian plasmas which can also be seen from Fig. 6.8. Although the response of the Maxwellian plasma to an ion is difficult to be obtained analytically, asymptotic formula were derived both in

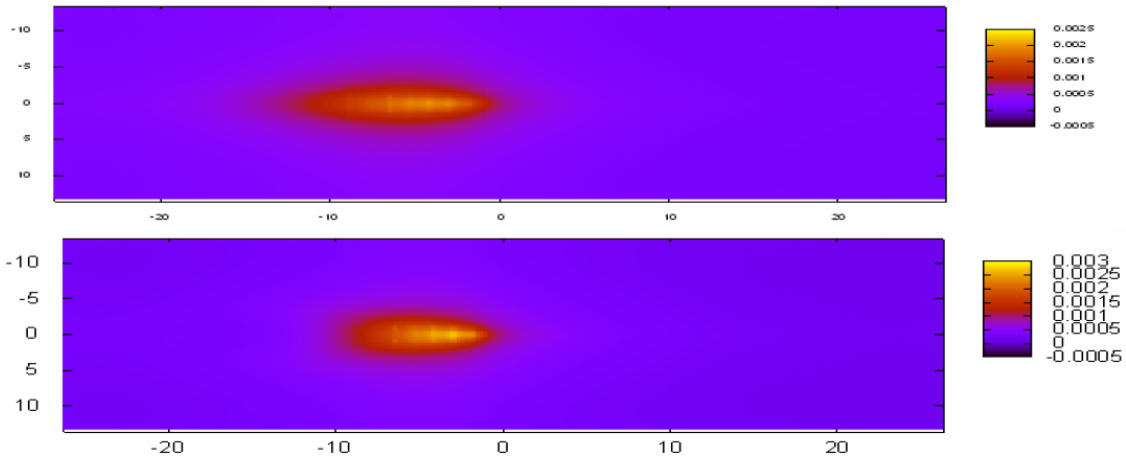


Figure 6.8 Responses of the electron plasma to a fast ion: 2D Contour Map. The abscissa is the longitudinal distance in units of Longitudinal Debye radius and the ordinate is the transverse distance in units of transverse Debye radius. The top graph is for the 2nd power Lorenzian plasma and the bottom graph is for the Maxwellian plasma**.** The ion is moving with velocity $5\sigma_e$ and the snapshot is taken at $\omega_p t = \pi$ **.**

space domain and in the wave vector domain. It had been derived by Landau and other authors in 1940s that the dependence of the plasma frequency and Landau damping rate on the wavelength are

$$\omega = \omega_p \sqrt{1 + \frac{3}{2} k^2 r_D^2}\,, \tag{6.32}$$

$$\gamma = \omega_p \sqrt{\frac{\pi}{8}} \frac{1}{(kr_D)^3} \exp\left( -\frac{1}{2 \cdot (kr_D)^2} - \frac{3}{2} \right),$$

for the isotropic Maxwellian plasma at limit $kr_D << 1$. Fig. 6.9 shows the plasma frequency and Landau damping rates for all three distributions at long wavelength limit. The 3rd Lorenzian plasma is clearly much closer to the Maxwellian plasma at this limit. At the short wavelength limit $kr_D >> 1$, the plasma frequency and Landau damping rate are given by

$$\omega = \frac{\pi \cdot \bar{k}}{\xi\left(\vec{k}\right)} \omega_p , \tag{6.33}$$

$$\gamma = \bar{k}\xi\left(\vec{k}\right)\omega_p , \tag{6.34}$$

where $\xi\left(\vec{k}\right)$ is implicitly determined by the following equation

$$\xi \exp\left(\xi^2 / 2\right) = \frac{1}{\sqrt{2\pi}} \bar{k}^2 . \tag{6.35}$$

Since $\xi\left(\vec{k}\right)$ is a slow varying function, both the Landau damping rate and the plasma frequency growth linearly with $\bar{k}$. As shown in Fig. 6.9 (c) and (d), although the behavior of the Lorenzian plasmas are very different from the Maxwellian plasma at short wavelength, the 3rd power Lorenzian distribution is still closer than the 2nd power Lorenzian distribution.

In space domain, the numerical solutions of the stationary electrostatic potential for the Maxwellian plasma have been calculated by various authors[25-27]. In order to compare our results with the previous numerical solutions, the electric potential must be calculated. By combining equation (6.5) and equation (6.15), the time derivative of the electric potential in $\vec{k}$ space is

$$\dot{\Phi}\left(\vec{k}, t\right) = -\frac{Z_i \omega_p e}{\varepsilon_0 k^2} \sin\left(\omega_p t\right) \exp\left(\lambda\left(\vec{k}\right) \cdot t\right). \tag{6.36}$$

By Fourier transforming equation (6.36) and taking into account the initial condition $\Phi\left(\vec{x}, 0\right) = \frac{Z_i e}{4\pi\varepsilon_0 \left|\vec{x}\right|}$, the electric potential induced by an moving ion in the second power Lorentzian plasma is obtained as

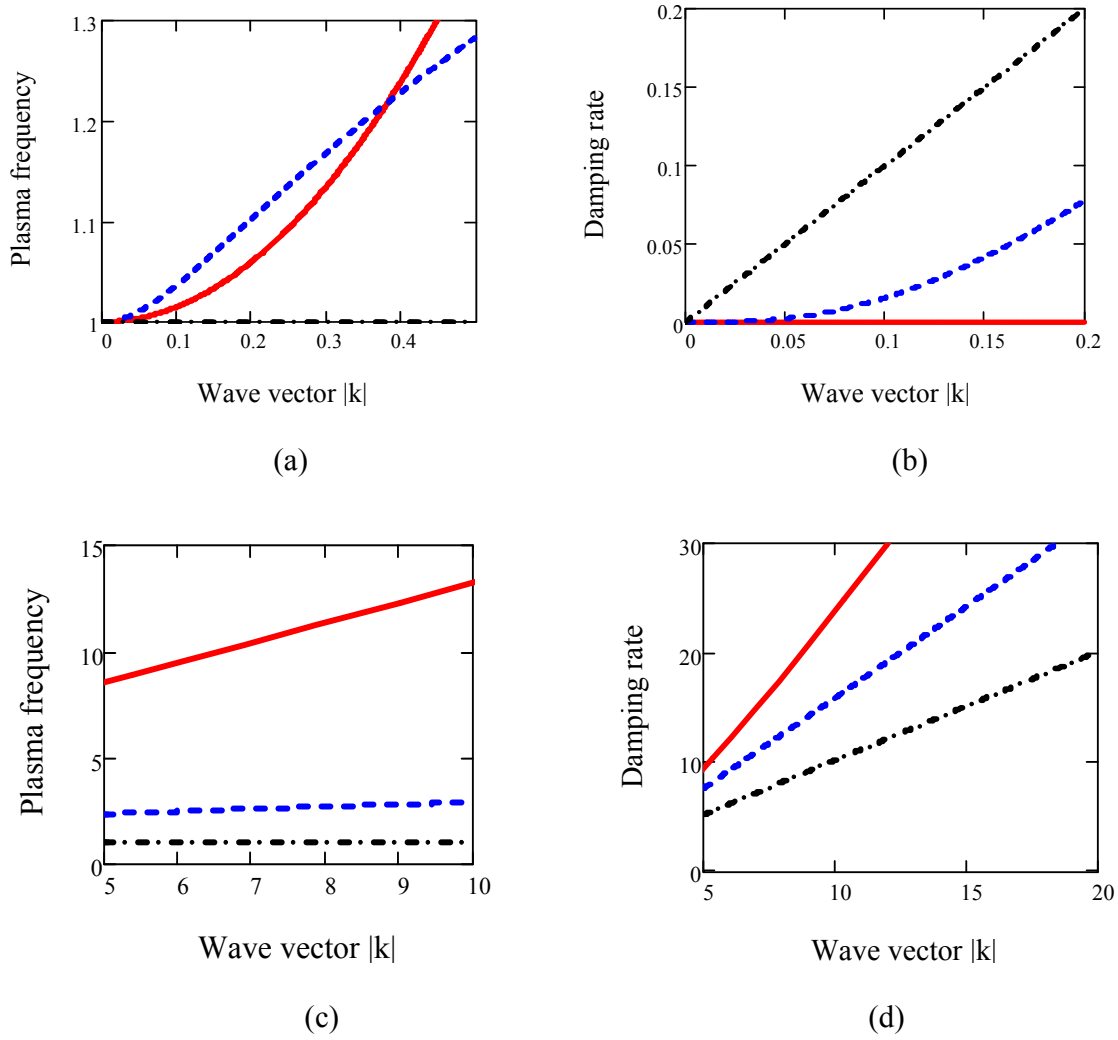


Figure 6.9 Plasma frequency and Landau damping rate at long and short wavelength limit. The abscissa is the wavelength in units of $1/r_D$. Graph (a) and (b) show the plasma frequency and Landau damping rate in units of $\omega_p$ at $kr_D << 1$. Graph (c) and (d) show the plasma frequency and Landau damping rate in units of $\omega_p$ at $kr_D >> 1$. The solid red line is for the Maxwellian plasma approximate formula, the blue dash line is for the 3rd Lorenzian plasma formula and the black dot-dash line is for the 2nd Lorenzian plasma formula.

$$\tilde{\Phi}(\vec{x},t) = \frac{Z_i e}{4\pi\varepsilon_0}\left[\frac{1}{|\vec{x}|} - \frac{2\omega_p}{\pi}\int_0^t \frac{\sin(\omega_p\tau)}{|\vec{x}+\vec{v}_0\tau|}\arctan\left(\frac{|\vec{x}+\vec{v}_0\tau|}{\beta\tau}\right)d\tau\right], \qquad (6.37)$$

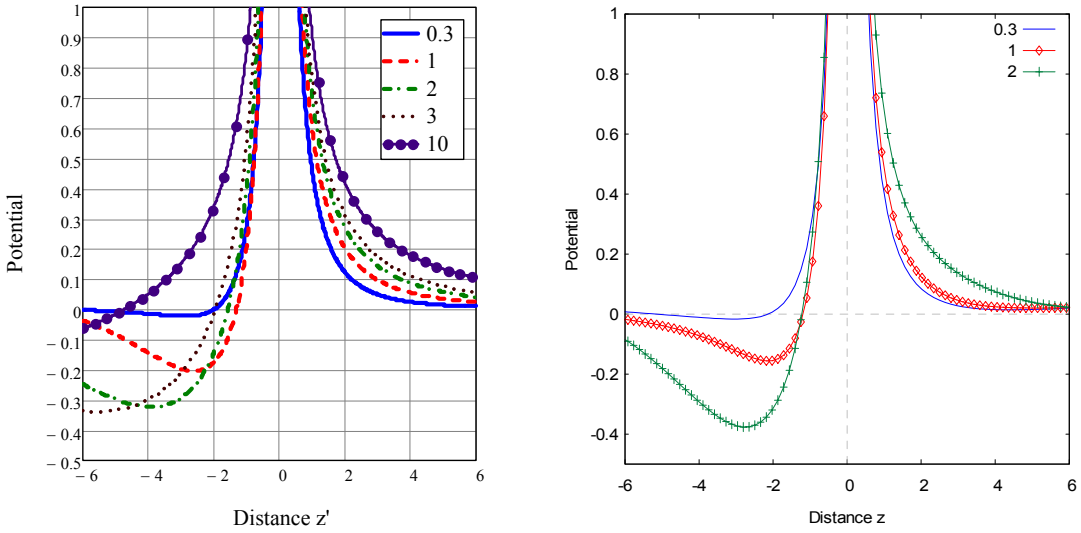


(a) (b)

Figure 6.10 Electric Potential along the moving direction for various ion speeds. The abscissa is the longitudinal distance from the moving ion and the ordinate is the electrical potential in units of $Z_i e / r_D$. (a) shows the analytic results for the second power Lorenzian plasma at $\psi = 60\pi$ and (b) shows the numerical results for the Maxwellian plasma. The $v_i / \sqrt{2}\beta_e = 1$ curve (red) and $v_i / \sqrt{2}\beta_e = 2$ curve (green) curve are taken at $\psi = 7\pi$ and the $v_i / \sqrt{2}\beta_e = 0.3$ curve (blue) is taken at $\psi = 15\pi$.

for $\beta_{x,y,z} = \beta$. Equation (6.5) can also be used to calculate the electric potential for the Maxwellian plasma by the FFT technology as $\tilde{n}_1(\vec{k}, t)$ has already been numerically solved. The results of the induced electric potential at $\psi >> 1$ are shown in Figure 8. Figure 6.10 (a) shows the analytic result expressed in equation (6.37) for the second power Lorentzian plasma and the snapshot of Figure 6.10 (a) is taken at $\psi = 60\pi$. Compared with the numerical results for the Maxwellian plasma[25-27], the results for the Lorentzian plasma agrees very well for $v_i \le \sqrt{2}\beta_e$ and is more flattened for higher velocities. Figure 6.10 (b) shows the FFT results for the Maxwellian plasma, which

agrees very well with the previous results (Figure 7 of reference [26], figure 4 of reference [27] and figure 9 of reference [25]). Since the Landau damping is slow for relatively long wavelength, some small differences at the tail may still exist. As the longitudinal range of the FFT calculation is limited by the memory of the computer and solving the dynamical equation (6.25) for a very long time range is also time-consuming, figure 6.10 (b) only shows results for relatively short time range and $v_i \le 2\beta_e$.

### 6.2.5 Summary and Discussion

The dynamic model described in section 1 and section 2 depends on the thermal distribution one chooses. This dependence seems to be weak while the ion is moving with velocity $v_i \le \sigma_e$. As a result, the analytic formula obtained for the Lorenzian distribution can describe the process with good accuracy. For fast ions, the effects due to the thermal distribution become strong but for ion velocity up to a few $\sigma_e$, the formula obtained for the 3rd power Lorenzian distribution may still serve as an qualitative estimation. Numerical solution for the Maxwellian distribution is straightforward under this model and could be much faster than the Particle In Cell simulations. As shown in section 3, the shielding effects for a rest ion sitting in anisotropic plasma seems to decays exponentially.

### *6.3 Amplification of Ion Shielding Signal in FEL (1D Calculation)*

As the electron beam is modulated by the ion, the modulation has to be amplified through some instability mechanisms. In this section, the instability is realized by a FEL amplifier and the calculation under 1D FEL theory is presented.

#### 6.3.1 Introduction

Assuming the velocity distribution of the electron beam is the second order Lorentzian distribution, from equation (6.66), the initial current density modulation in the lab frame is given by

$$\tilde{j}_1(z,t) = -\frac{Z_i ec}{\pi^2 a_x a_y a_z}\int_0^{\psi_p} \frac{\xi \sin\xi d\xi}{\left(\xi^2 + \left(\bar{x} + \bar{v}_{0x}\xi\right)^2 + \left(\bar{y} + \bar{v}_{0y}\xi\right)^2 + \left(\frac{\gamma_0\left(z-\beta ct\right)}{a_z} + \bar{v}_{0z}\xi\right)^2\right)^2}. \tag{6.38}$$

As the 1D FEL theories are well developed in the frequency domain, we will Fourier transform (6.38) into the frequency domain and calculate the evolution for each frequency component. Then we transform the results back to the time domain to get the output of the amplified electron current density. In order to avoid the fast oscillating factor, the Fourier transformation has been done according to the following formula

$$\hat{\tilde{j}}_1(z,\omega) = \frac{1}{\omega}\int_{-\infty}^{\infty} \tilde{j}_1(z,t) e^{-i\psi} d\psi\,, \tag{6.39}$$

$$\tilde{j}_1(z,t) = \frac{1}{2\pi} e^{ik_w z}\int_{-\infty}^{\infty} \hat{\tilde{j}}_1(z,k) e^{ik(z-ct)} d\omega\,, \tag{6.40}$$

where $\psi = (k_w + k)z - \omega t$, $\hat{\tilde{j}}_1(z,\omega) \equiv e^{-i\left(\frac{\omega}{c}+k_w\right)z}\tilde{j}_1(z,\omega)$ and $\tilde{j}_1(z,\omega) = \int_{-\infty}^{\infty} \tilde{j}_1(z,t)e^{i\omega t}dt$.

### 6.3.2 Review 1D FEL Theory with Non-zero Initial Modulation

For a specific radiation/amplification frequency, the dynamics inside the FEL is determined by the following Hamiltonian [28, 29]. The Hamiltonian is given by

$$H = CP + \frac{\omega}{2c\gamma_z^2\varepsilon_0}P^2 - \left(U(z)e^{i\psi} + U^*(z)e^{-i\psi}\right) + e\int d\psi E_z \,. \tag{6.41}$$

The conjugate variable and its momentum is $(\psi, P)$ which are defined as,

$$P = \varepsilon - \varepsilon_0 \,,$$

$$\psi = k_w z + kz - \omega t \,,$$

and the time variable is $z$, where $\varepsilon$ is the energy of the electron, $\varepsilon_0$ is the average energy of the total bunch, $\omega$ is the frequency of the considered Fourier component, $U(z)$ is the complex amplitude of the effective potential of the particle interaction with the electromagnetic wave, $E_z$ is the longitudinal space charge field and $k_w$ is the wave number of the FEL wiggler[13]. The coefficients in the Hamiltonian is the detune of the designed energy $\varepsilon_0$,

[13] Please refer [29] E. L. Saldin, E. A. Schneidmiller, and M. V. Yurkov, *The Physics of Free Electron Lasers*(Springer, New York, 1999). equation (2.6) for detailed derivation of the Hamiltonian (6.41).

$$C = k_w - \frac{k}{2\gamma_z^2},$$

and the longitudinal energy is defined as

$$\gamma_z^{-2} \equiv 1 - \beta_z^2 = 1 - \beta^2 + \beta_x^2 + \beta_y^2 = \gamma^{-2}\left(1 + K^2\right),$$

where the undulator parameter $K$ is defined as

$$K \equiv \frac{eB_w}{m_e c k_w}.$$

The evolution of the electron beam is determined by the 1-D Vlasov equation,

$$\frac{\partial}{\partial z} f + \frac{\partial H}{\partial P}\frac{\partial}{\partial \psi} f - \frac{\partial H}{\partial \psi}\frac{\partial}{\partial P} f = 0. \tag{6.42}$$

From (6.41), we obtain the following results

$$\frac{\partial H}{\partial P} = C + \frac{\omega}{c\gamma_z^2 \varepsilon_0} P, \tag{6.43}$$

$$\frac{\partial}{\partial \psi} H = -iU(z)e^{i\psi} + iU^*(z)e^{-i\psi} + eE_z. \tag{6.44}$$

As we are considering one Fourier components with specific frequency, we can write the distribution function into the following form,

$$f(\psi, P, z) = f_0(P) + \tilde{f}_1(P, z)e^{i\psi} + \tilde{f}_1^*(P, z)e^{-i\psi}, \tag{6.45}$$

where $f_0(P)$ is the equilibrium distribution and $\tilde{f}_1(P, z)$ is the complex amplitude of the perturbation. In order to have a solution for the Vlasov equation, the space charge force must have the following form,

$$E_z(z) = \tilde{E}_z(z)e^{i\psi} + \tilde{E}_z{}^*(z)e^{-i\psi}. \tag{6.46}$$

Inserting equation (6.45) ~ (6.46) into equation (6.42), the linearized Vlasov equation is obtained as the following

$$\frac{\partial}{\partial z}\tilde{f}_1(P,z)+i\left(C+\frac{\omega}{c\gamma_z^2\varepsilon_0}P\right)\tilde{f}_1(P,z)+\left(iU(z)-e\tilde{E}_z\right)\frac{\partial}{\partial P}f_0=0. \tag{6.47}$$

Next, we will derive the relation between the longitudinal space charge and the current density perturbation. In free space, the Maxwell equations are

$$\frac{\partial}{\partial z}E_z=\frac{\rho(z,t)}{\varepsilon_0}, \tag{6.48}$$

and the 1D continuous equation reads

$$\frac{\partial}{\partial t}\rho(z,t)=-\frac{\partial}{\partial z}j(z,t). \tag{6.49}$$

Combining equation (6.48) with (6.49), one obtain the following relation

$$\frac{\partial}{\partial z}\frac{\partial}{\partial t}E_z=\frac{1}{\varepsilon_0}\frac{\partial}{\partial t}\rho(z,t)=-\frac{1}{\varepsilon_0}\frac{\partial}{\partial z}j(z,t). \tag{6.50}$$

Assuming the space charge field solely comes from the perturbation, one gets

$$\frac{\partial}{\partial t}E_z=\frac{1}{\varepsilon_0}\frac{\partial}{\partial t}\rho(z,t)=-\frac{1}{\varepsilon_0}j(z,t). \tag{6.51}$$

Since the perturbed charge density is related to the perturbed current by

$$j_1(z,t)=\tilde{j}_1(z)e^{i\psi}+\tilde{j}_1^*(z)e^{-i\psi}=-ece^{i\psi}\int_{-\infty}^{\infty}\tilde{f}_1(P,z)dP+c.c. \tag{6.52}$$

, the complex magnitude of the longitudinal space charge field is related to the distribution perturbation amplitude by

$$\tilde{E}_z(z)=-i\frac{\tilde{j}_1(z)}{\varepsilon_0\omega}. \tag{6.53}$$

From (6.47) and (6.53), one has

$$\frac{\partial}{\partial z}\left\{\tilde{f}_1(P,z)\cdot\exp\left[i\left(C+\frac{\omega}{c\gamma_z^2\varepsilon_0}P\right)z\right]\right\}=-\exp\left[i\left(C+\frac{\omega}{c\gamma_z^2\varepsilon_0}P\right)z\right]\left(iU(z)+i\frac{\tilde{j}_1(z)e}{\varepsilon_0\omega}\right)\frac{\partial}{\partial P}f_0. \tag{6.54}$$

Integrating both sides of equation (6.54) generates

$$\tilde{f}_1(P,z) = -\int_0^z \exp\left[ i\left( C + \frac{\omega}{c\gamma_z^2 \varepsilon_0} P \right)(z'-z) \right] \left( iU(z') + i\frac{\tilde{j}_1(z')e}{\varepsilon_0 \omega} \right) \frac{\partial}{\partial P} f_0 dz' + \tilde{f}_1(P,0) \exp\left[ -i\left( C + \frac{\omega}{c\gamma_z^2 \varepsilon_0} P \right) z \right], \quad (6.55)$$

which is equation (2.52) of reference[29]. Integrating (6.55) over the energy $P$ and inserting (6.52) generates

$$\begin{aligned} \tilde{j}_1(z) = in_0 ec \int_0^z dz' \left( U(z') + \frac{\tilde{j}_1(z')e}{\varepsilon_0 \omega} \right) \int_{-\infty}^{\infty} dP \exp\left[ i\left( C + \frac{\omega}{c\gamma_z^2 \varepsilon_0} P \right)(z'-z) \right] \frac{\partial}{\partial P} F(P) \\ - ec \int_{-\infty}^{\infty} \tilde{f}_1(P,0) \exp\left[ -i\left( C + \frac{\omega}{c\gamma_z^2 \varepsilon_0} P \right) z \right] dP \end{aligned} . \quad (6.56)$$

The effective potential is defined as (ref [29] eq.(2.7))

$$U(z) = -\frac{e\theta_s \tilde{E}(z)}{2i}, \quad (6.57)$$

and the radiation field is related to the current density perturbation by (we assume that no radiation field at the entrance of the FEL).

$$\frac{d}{dz} \tilde{E}(z) = -\frac{\theta_s}{2\varepsilon_0 c} \tilde{j}_1(z) \quad (6.58)$$

, where $\theta_s$ is the transverse angle of the electron velocity inside the undulator and is related to the undulator parameter by $\theta_s = \frac{K}{\gamma}$. Inserting equation (6.57) and (6.58) into (6.56) and using the reduced variables as defined below,

$$\Gamma = \left( \frac{\pi \omega j_0 \theta_s^2}{c\gamma_z^2 I_A \gamma} \right)^{\frac{1}{3}}, \qquad \hat{z} = z\Gamma, \qquad \hat{P} = \frac{P}{\rho \varepsilon_0},$$

$$\rho = \frac{\gamma_z^2 \Gamma c}{\omega}, \qquad \hat{C} = C/\Gamma, \qquad \hat{\Lambda}_p^2 = \frac{4\pi j_0}{\gamma_z^2 I_A \gamma \Gamma^2}, \quad (6.59)$$

equation (6.56) can be written as (ref [29] eq.(2.19))

$$\frac{d}{d\hat{z}}\tilde{E}(z)=\int_0^{\hat{z}}d\hat{z}'\left(\tilde{E}(z)+i\hat{\Lambda}_p^2\frac{d}{d\hat{z}'}\tilde{E}(z')\right)\int_{-\infty}^{\infty}d\hat{P}\exp\left[i\left(\hat{C}+\hat{P}\right)\left(\hat{z}'-\hat{z}\right)\right]\frac{\partial}{\partial\hat{P}}F(\hat{p})$$
$$+\frac{e\theta_s}{2\varepsilon_0\Gamma}\int_{-\infty}^{\infty}\tilde{f}_1(\hat{P})\exp\left[-i\left(\hat{C}+\hat{P}\right)\hat{z}\right]d\hat{P} \qquad (6.60)$$

where the following relation are used

$$F(P)=F(\hat{p})\frac{\omega}{c\gamma_z^2\varepsilon_0\Gamma},$$

$$\tilde{f}_1(P)=\tilde{f}_1(\hat{p})\frac{\omega}{c\gamma_z^2\varepsilon_0\Gamma}.$$

If we define a reference electric field as $E_0\equiv\frac{\theta_s j_0}{2\varepsilon_0 c\Gamma}$, we obtain

$$\frac{d}{d\hat{z}}\tilde{E}(z)=\int_0^{\hat{z}}d\hat{z}'\left(\tilde{E}(z)+i\hat{\Lambda}_p^2\frac{d}{d\hat{z}'}\tilde{E}(z')\right)\int_{-\infty}^{\infty}d\hat{P}\exp\left[i\left(\hat{C}+\hat{P}\right)\left(\hat{z}'-\hat{z}\right)\right]\frac{\partial}{\partial\hat{P}}F(\hat{p})$$
$$+E_0\cdot\frac{1}{n_0}\int_{-\infty}^{\infty}\tilde{f}_1(\hat{P})\exp\left[-i\left(\hat{C}+\hat{P}\right)\hat{z}\right]d\hat{P}$$

Thus the equation for the radiation field in units of the reference electric field is

$$\frac{d}{d\hat{z}}\hat{\tilde{E}}(\hat{z})=\int_0^{\hat{z}}d\hat{z}'\left(\hat{\tilde{E}}(\hat{z}')+i\hat{\Lambda}^2{}_p\frac{d}{d\hat{z}'}\hat{\tilde{E}}(\hat{z}')\right)\int_{-\infty}^{\infty}d\hat{P}\exp\left[i\left(\hat{C}+\hat{P}\right)\left(\hat{z}'-\hat{z}\right)\right]\frac{\partial}{\partial\hat{P}}F\left(\hat{P}\right)$$
$$+\frac{1}{n_0}\int_{-\infty}^{\infty}\tilde{f}_1\left(\hat{P},0\right)\exp\left[-i\left(\hat{C}+\hat{P}\right)\hat{z}\right]d\hat{P} \qquad (6.61)$$

, where $\hat{\tilde{E}}(z)=\frac{\tilde{E}(z)}{E_0}$. The initial condition $\tilde{f}_1(\hat{P},0)$ can be obtained by the following integral

$$\tilde{f}_1(P,0)=\frac{1}{2\pi}\int_{-\pi}^{\pi}f_1(\psi,P,0)e^{-i\psi}d\psi.$$

### 6.3.3 Equivalent Differential Equation for Cold Electron Beam

Considering $F(\hat{P}) = \delta(\hat{P})$, the integral over $\hat{P}$ in equation (6.61) is

$$\int_{-\infty}^{\infty} d\hat{P} \exp\left[i\left(\hat{C}+\hat{P}\right)\left(\hat{z}'-\hat{z}\right)\right]\frac{\partial}{\partial \hat{P}}\delta\left(\hat{P}\right) = -i\left(\hat{z}'-\hat{z}\right)\exp\left[i\hat{C}\left(\hat{z}'-\hat{z}\right)\right]. \tag{6.62}$$

Inserting (6.62) into (6.61), and multiplying both sides by $e^{i\hat{C}\hat{z}}$, one obtains

$$\begin{aligned}\exp\left[i\hat{C}\hat{z}\right]\frac{d}{d\hat{z}}\hat{\tilde{E}}\left(\hat{z}\right) = & -i\int_0^{\hat{z}} d\hat{z}'\left(\hat{\tilde{E}}\left(\hat{z}'\right)+i\hat{\Lambda}_p^2\frac{d}{d\hat{z}'}\hat{\tilde{E}}\left(\hat{z}'\right)\right)\left(\hat{z}'-\hat{z}\right)\exp\left[i\hat{C}\left(\hat{z}'\right)\right] \\ & + \frac{1}{n_0}\int_{-\infty}^{\infty}\tilde{f}_1\left(\hat{P},0\right)\exp\left[-i\hat{P}\hat{z}\right]d\hat{P}\end{aligned}. \tag{6.63}$$

If we define

$$H\left(\hat{z}\right) = \hat{\tilde{E}}\left(\hat{z}\right)e^{i\hat{C}\hat{z}}, \tag{6.64}$$

and apply the following relation

$$e^{i\hat{C}\hat{z}}\frac{d}{d\hat{z}}\hat{\tilde{E}}\left(\hat{z}\right) = \frac{d}{d\hat{z}}H\left(\hat{z}\right) - i\hat{C}H\left(\hat{z}\right)$$

, equation (6.63) can be rewritten into

$$\begin{aligned}\frac{d}{d\hat{z}}H\left(\hat{z}\right) - \left(i\hat{C}\right)H\left(\hat{z}\right) = & -i\int_0^{\hat{z}} d\hat{z}'\left(H\left(\hat{z}'\right)+i\hat{\Lambda}_p^2\frac{d}{d\hat{z}}H\left(\hat{z}'\right)+\hat{\Lambda}_p^2\hat{C}H\left(\hat{z}'\right)\right)\left(\hat{z}'-\hat{z}\right) \\ & + \frac{1}{n_0}\int_{-\infty}^{\infty}\tilde{f}_1\left(\hat{P},0\right)\exp\left[-i\hat{P}\hat{z}\right]d\hat{P}\end{aligned}. \tag{6.65}$$

The second derivative of (6.65) with respect to $\hat{z}$ reads

$$\begin{aligned}\frac{d^3}{d\hat{z}^3}H\left(\hat{z}\right) - \left(i\hat{C}\right)\frac{d^2}{d\hat{z}^2}H\left(\hat{z}\right) = & iH\left(\hat{z}\right) - \hat{\Lambda}_p^2\frac{d}{d\hat{z}}H\left(\hat{z}\right) + i\hat{\Lambda}_p^2\hat{C}H\left(\hat{z}\right) \\ & + \frac{1}{n_0}\frac{d^2}{d\hat{z}^2}\int_{-\infty}^{\infty}\tilde{f}_1\left(\hat{P},0\right)\exp\left[-i\hat{P}\hat{z}\right]d\hat{P}\end{aligned}. \tag{6.66}$$

Applying the following relations,

$$\frac{d}{d\hat{z}}H(\hat{z}) = i\hat{C}e^{i\hat{C}\hat{z}}\tilde{\hat{E}}(\hat{z}) + e^{i\hat{C}\hat{z}}\frac{d}{d\hat{z}}\tilde{\hat{E}}(\hat{z}),$$

$$\frac{d^2}{d\hat{z}^2}H(\hat{z}) = -\hat{C}^2e^{i\hat{C}\hat{z}}\tilde{\hat{E}}(\hat{z}) + 2i\hat{C}e^{i\hat{C}\hat{z}}\frac{d}{d\hat{z}}\tilde{\hat{E}}(\hat{z}) + e^{i\hat{C}\hat{z}}\frac{d^2}{d\hat{z}^2}\tilde{\hat{E}}(\hat{z}),$$

$$\frac{d^3}{d\hat{z}^3}H(\hat{z}) = -3\hat{C}^2e^{i\hat{C}\hat{z}}\frac{d}{d\hat{z}}\tilde{\hat{E}}(\hat{z}) - i\hat{C}^3e^{i\hat{C}\hat{z}}\tilde{\hat{E}}(\hat{z}) + 3i\hat{C}e^{i\hat{C}\hat{z}}\frac{d^2}{d\hat{z}^2}\tilde{\hat{E}}(\hat{z}) + e^{i\hat{C}\hat{z}}\frac{d^3}{d\hat{z}^3}\tilde{\hat{E}}(\hat{z})$$

, we obtain the differential equation for the radiation field,

$$\begin{aligned}&\frac{d^3}{d\hat{z}^3}\tilde{\hat{E}}(\hat{z}) + 2i\hat{C}\frac{d^2}{d\hat{z}^2}\tilde{\hat{E}}(\hat{z}) + \left(\hat{\Lambda}_p^2 - \hat{C}^2\right)\frac{d}{d\hat{z}}\tilde{\hat{E}}(\hat{z})\\ &= i\tilde{\hat{E}}(\hat{z}) - \frac{1}{n_0}\int_{-\infty}^{\infty}\hat{P}^2\tilde{f}_1(\hat{P},0)\exp\left[-i\left(\hat{P}+\hat{C}\right)\hat{z}\right]d\hat{P}\end{aligned} \tag{6.67}$$

, which is identical to Saldin's result except for an inhomogeneous term caused by the initial modulation[14] (ref [29] eq.(2.57)).

### 6.3.4 Equivalent Differential Equation for Lorentzian Electron Beam

If we assume the energy distribution of the background has the following form

$$F(\hat{P}) = \frac{1}{\pi\hat{q}}\frac{1}{1+\frac{\hat{P}^2}{\hat{q}^2}}, \tag{6.68}$$

the $\hat{P}$ integral in eq.(6.61) becomes

[14] This inhomogeneous term is claimed to be small in ref [30]. In order to study the detailed effects of this term for the CeC purpose, one needs to solve for $f(\vec{x},v_x,t)$ in the modulator.

$$\int_{-\infty}^{\infty} d\hat{P}\exp\left[i\left(\hat{C}+\hat{P}\right)\left(\hat{z}'-\hat{z}\right)\right]\frac{\partial}{\partial\hat{P}}F\left(\hat{P}\right)=-i\left(\hat{z}'-\hat{z}\right)\exp\left[i\hat{C}\left(\hat{z}'-\hat{z}\right)-\left|\hat{q}\left(\hat{z}'-\hat{z}\right)\right|\right].$$

The integral differential equation is written to

$$\frac{d}{d\hat{z}}\hat{\tilde{E}}\left(\hat{z}\right)=g_0\left(\hat{z}\right)-i\int_0^{\hat{z}}d\hat{z}'\left(\hat{\tilde{E}}\left(\hat{z}'\right)+i\hat{\Lambda}_p^2\frac{d}{d\hat{z}'}\hat{\tilde{E}}\left(\hat{z}'\right)\right)\left(\hat{z}'-\hat{z}\right)\exp\left[-\left(\hat{q}+i\hat{C}\right)\left(\hat{z}-\hat{z}'\right)\right]$$

, where

$$g_0\left(\hat{z}\right)\equiv\frac{1}{n_0}\int_{-\infty}^{\infty}\tilde{f}_1\left(\hat{P},0\right)\exp\left[-i\left(\hat{C}+\hat{P}\right)\hat{z}\right]d\hat{P}\ . \tag{6.69}$$

Defining

$$H\left(\hat{z}\right)\equiv\exp\left[\left(\hat{q}+i\hat{C}\right)\hat{z}\right]\hat{\tilde{E}}\left(\hat{z}\right), \tag{6.70}$$

and following the similar procedure as the last section, one obtain the differential equation for $H\left(\hat{z}\right)$

$$\frac{d^3}{d\hat{z}^3}H\left(\hat{z}\right)-\left(\hat{q}+i\hat{C}\right)\frac{d^2}{d\hat{z}^2}H\left(\hat{z}\right)+\hat{\Lambda}_p^2\frac{d}{d\hat{z}}H\left(\hat{z}\right)-\left[i+\hat{\Lambda}_p^2\left(\hat{q}+i\hat{C}\right)\right]H\left(\hat{z}\right)=g_2\left(\hat{z}\right) \tag{6.71}$$

, where

$$g_2\left(\hat{z}\right)\equiv\frac{1}{n_0}\int_{-\infty}^{\infty}\left(\hat{q}-i\hat{P}\right)^2\tilde{f}_1\left(\hat{P},0\right)\exp\left[\left(\hat{q}-i\hat{P}\right)\hat{z}\right]d\hat{P}. \tag{6.72}$$

Defining $\hat{C}_{eff}=\hat{C}-i\hat{q}$, equation (6.70) and (6.71) become

$$H\left(\hat{z}\right)\equiv\exp\left[i\hat{C}_{eff}\hat{z}\right]\hat{\tilde{E}}\left(\hat{z}\right), \tag{6.73}$$

$$\frac{d^3}{d\hat{z}^3}H\left(\hat{z}\right)-i\hat{C}_{eff}\frac{d^2}{d\hat{z}^2}H\left(\hat{z}\right)+\hat{\Lambda}_p^2\frac{d}{d\hat{z}}H\left(\hat{z}\right)-i\left[1+\hat{\Lambda}_p^2\hat{C}_{eff}\right]H\left(\hat{z}\right)=g_2\left(\hat{z}\right). \tag{6.74}$$

Equations (6.73) and (6.74) have exactly the same form as (6.64) and (6.66). Thus the equation of motion for the radiation field $\hat{\tilde{E}}\left(\hat{z}\right)$ is

$$\begin{aligned}&\frac{d^3}{d\hat{z}^3}\hat{\tilde{E}}(\hat{z})+2i\hat{C}_{eff}\frac{d^2}{d\hat{z}^2}\hat{\tilde{E}}(\hat{z})+\left(\hat{\Lambda}_p^2-\hat{C}_{eff}^2\right)\frac{d}{d\hat{z}}\hat{\tilde{E}}(\hat{z})\\&=i\hat{\tilde{E}}(\hat{z})+\frac{1}{n_0}\exp\left(-i\hat{C}_{eff}\hat{z}\right)\frac{d^2}{d\hat{z}^2}\int_{-\infty}^{\infty}\tilde{f}_1(\hat{P},0)\exp\left[\hat{q}\hat{z}-i\hat{P}\hat{z}\right]d\hat{P}\end{aligned}. \quad (6.75)$$

Inserting $\hat{C}_{eff}=\hat{C}-i\hat{q}$ back into equation (6.75), we obtain the differential equation of the radiation field generated by a Lorentzian electron beam

$$\begin{aligned}&\frac{d^3}{d\hat{z}^3}\hat{\tilde{E}}(\hat{z})+2\left(i\hat{C}+\hat{q}\right)\frac{d^2}{d\hat{z}^2}\hat{\tilde{E}}(\hat{z})+\left[\hat{\Lambda}_p^2+\left(i\hat{C}+\hat{q}\right)^2\right]\frac{d}{d\hat{z}}\hat{\tilde{E}}(\hat{z})-i\hat{\tilde{E}}(\hat{z})\\&=\frac{1}{n_0}\int_{-\infty}^{\infty}\left(\hat{q}-i\hat{P}\right)^2\tilde{f}_1(\hat{P},0)\exp\left[-i\left(\hat{P}+\hat{C}\right)\hat{z}\right]d\hat{P}\end{aligned}. \quad (6.76)$$

Comparing equation (6.76) with (6.67), we see that the energy spread adds an additional imaginary part to the detune $\hat{C}$, which is responsible for the Landau damping of the current density.

### 6.3.5 Solution of The Homogeneous Differential Equation

The solution of equation (6.76) has general solution parts from the homogenous equation and the inhomogeneous part from the particular solution. The solution for the homogenous equation

$$\frac{d^3}{d\hat{z}^3}\hat{\tilde{E}}(\hat{z})+2\left(i\hat{C}+\hat{q}\right)\frac{d^2}{d\hat{z}^2}\hat{\tilde{E}}(\hat{z})+\left[\hat{\Lambda}_p^2+\left(i\hat{C}+\hat{q}\right)^2\right]\frac{d}{d\hat{z}}\hat{\tilde{E}}(\hat{z})-i\hat{\tilde{E}}(\hat{z})=0 \quad (6.77)$$

has the following form

$$E(\hat{z})=A_1e^{\lambda_1\hat{z}}+A_2e^{\lambda_2\hat{z}}+A_3e^{\lambda_3\hat{z}} \quad (6.78)$$

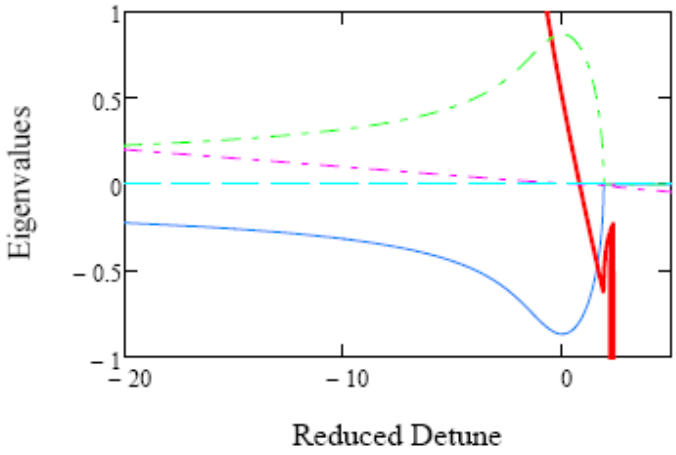


Figure 6.11 Eigenvalues for the homogeneous differential equation (6.77) for $\hat{\Lambda}_p = 0$ and $\hat{q} = 0$. The green dot-dash curve and the purple dot-dash curve are the real and imaginary part of the growth mode respectively. The dark blue solid curve and the red solid curve are the real and imaginary part of the damping mode. The light blue solid curve is the oscillating mode.

, where $\lambda_i$ are the eigenvalues to be determined by equation

$$\lambda^3 + 2\left(\hat{q} + i\hat{C}\right)\lambda^2 + \left[\hat{\Lambda}_p^2 + \left(\hat{q} + i\hat{C}\right)^2\right]\lambda - i = 0 \qquad (6.79)$$

, and the coefficients $A_i$ are determined by the initial condition. The solution of equation (6.79) can be expressed analytically as

$$\lambda_1 = -\frac{a_2}{3} + S + T,$$

$$\lambda_2 = -\frac{a_2}{3} - \left(\frac{1}{2} - \frac{\sqrt{3}}{2}i\right)S - \left(\frac{1}{2} + \frac{\sqrt{3}}{2}i\right)T,$$

$$\lambda_3 = -\frac{a_2}{3} - \left(\frac{1}{2} + \frac{\sqrt{3}}{2}i\right)S - \left(\frac{1}{2} - \frac{\sqrt{3}}{2}i\right)T,$$

where

$$a_2 = 2\left(\hat{q} + i\hat{C}\right), \qquad a_1 = \hat{\Lambda}_p^2 + \left(\hat{q} + i\hat{C}\right)^2, \qquad a_0 = -i,$$

$$S = \left(R + \sqrt{D}\right)^{\frac{1}{3}}, \qquad T = \left(R - \sqrt{D}\right)^{\frac{1}{3}}, \qquad Q = \frac{3a_1 - a_2^2}{9},$$

$$D = Q^3 + R^2, \qquad R = \frac{9a_1a_2 - 27a_0 - 2a_2^3}{54}.$$

Figure 6.11 shows the eigenvalues for $\hat{\Lambda}_p = 0$ and $\hat{q} = 0$ as a function of the detune $\hat{C}$.

### 6.3.6 Small Energy Spread Approximation for $\hat{q}^2 << 1$

As one can see from equation (6.76), the inhomogeneous term is due to the energy spread of the equilibrium distribution and the initial perturbation itself. If we assume the energy spread is small enough such that $\int_{-\infty}^{\infty} \hat{P}^2 f_1\left(\hat{P}\right) d\hat{P} << 1$ and $\hat{q}^2 << 1$, the inhomogeneous part of the solution is negligible comparing with the homogenous part and the coefficients $A_i$ are determined by the following equation,

$$\begin{pmatrix} A_1 \\ A_2 \\ A_3 \end{pmatrix} = \begin{pmatrix} 1 & 1 & 1 \\ \lambda_1 & \lambda_2 & \lambda_3 \\ \lambda_1^2 & \lambda_2^2 & \lambda_3^2 \end{pmatrix}^{-1} \begin{pmatrix} \hat{E}(0) \\ \frac{d}{d\hat{z}}\hat{E}(0) \\ \frac{d^2}{d\hat{z}^2}\hat{E}(0) \end{pmatrix}. \tag{6.80}$$

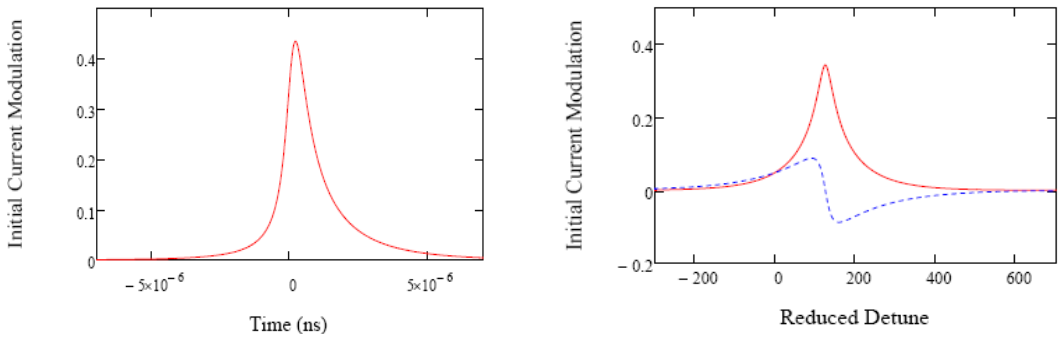


Figure 6.12 Initial current density modulations for an ion moving with velocity $v_z = 0.5\beta_z$ where $\beta_z$ is the velocity spread of the electrons in co-moving frame. (a) the current density modulation in time domain with the longitudinal Debye radius being $700nm$ . The abscissa is time in units of seconds and the ordinate is the current density modulation. (b) the current density in frequency domain. The abscissa is the detune $\hat{C}$ and the ordinate is the Fourier components of the current density at the corresponding detune.

The initial condition of the radiation field is determined by the initial condition of the current density modulation through equation (6.58). Inserting equation (6.38) into equation (6.39) generates the initial current density modulation in the frequency domain

$$\tilde{j}_1(x,y,z,\omega) = -\frac{Z_i ec}{2\pi a_x a_y a_z \omega} a_\psi \int_0^\infty \frac{\xi \sin\xi e^{\left(i\left(\frac{\omega}{\beta c}-k_w-k\right)z+\left(i\bar{v}_{0z}\xi-f_\perp\right)a_\psi\right)}}{f_\perp(\xi)^3}\left[1+a_\psi f_\perp(\xi)\right]d\xi \qquad (6.81)$$

, where $a_\psi = \frac{a_z\omega}{\beta c\gamma_0}$ and $f_\perp(\xi)^2 = \xi^2 + \left(\bar{x}+\bar{v}_{0x}\xi\right)^2 + \left(\bar{y}+\bar{v}_{0y}\xi\right)^2$. Figure (6.12) shows the initial modulation of the electron current caused by a moving ion with velocity $v_z = 0.5\beta_z$ and longitudinal Debye radius being $0.7\mu m$ at the time domain and the frequency domain. From equation (6.58), one gets the initial condition for $\frac{d}{d\hat{z}}\hat{\tilde{E}}(0)$, $\frac{d^2}{d\hat{z}^2}\hat{\tilde{E}}(0)$ and

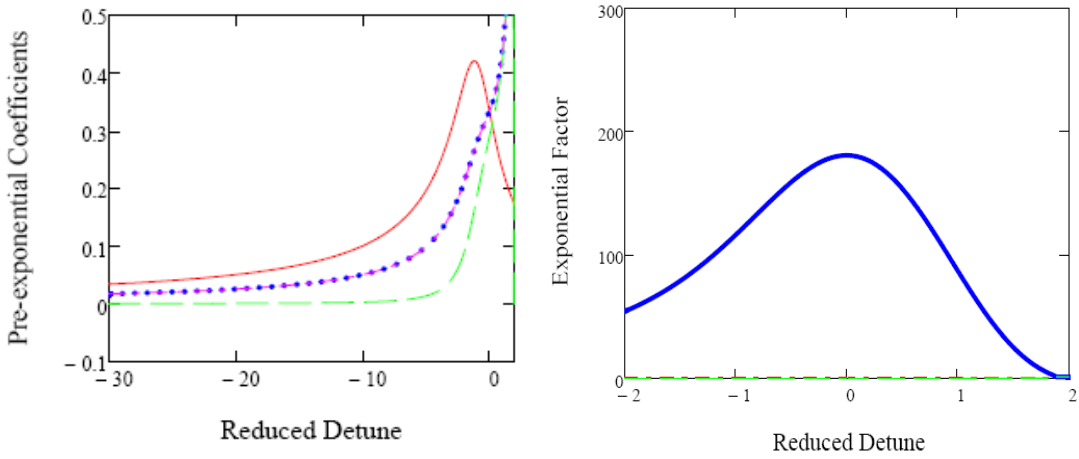


(a) (b)

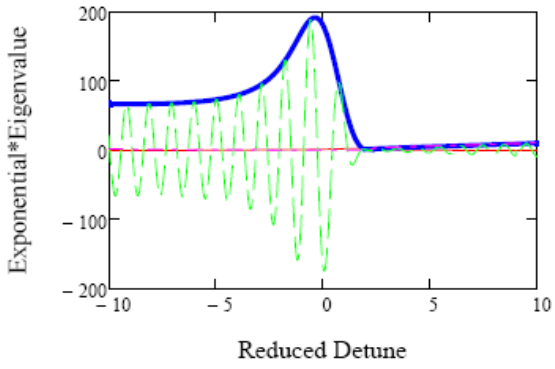


(c)

Figure 6.13 The dependence of each factors of expression (6.87) on the detune $\hat{C}$. (a) the amplitude of coefficients $A_i$ calculated from equation (6.88) as a function of the detune[15]. The red solid curve is for the oscillation mode, the blue solid curve is for the growth mode and the purple dot-dash curve is for the damping mode. The green dash curve is the real part of the growth mode; (b) the amplitude of the exponential factors $e^{\lambda_i \hat{z}}$ after $\hat{z} = 6$ of propagation inside the FEL as a function of the detune $\hat{C}$. The blue solid curve is the growth mode, the red solid curve is the oscillating mode and the green solid curve is the damping mode; (c) the amplitude of the eigenvlaue multiplying the exponential factor, $\lambda_i e^{\lambda_i \hat{z}}$ after $\hat{z} = 6$ of propagation in side the FEL as a function of the detune. The blue solid curve is the growth mode, the red solid curve is the oscillating mode and purple dash-dot curve is the damping mode. The green curve is the real part of the growth mode.

[15] There is a divergence of $A_i$ around $\hat{C} = 1.89$ which is due to the degenerate of the eigenvalues as shown in Figure 6.11. This divergence can be cured by rearrange the terms in (6.87).

$\frac{d^3}{d\hat{z}^3}\hat{\tilde{E}}(0)$ as the following,

$$\frac{d}{d\hat{z}}\hat{\tilde{E}}(0) = -\frac{\tilde{j}_1}{ecn_0} = \frac{Z_i}{2\pi n_0 a_x a_y a_z \omega} a_\psi \int_0^\infty \frac{\xi \sin\xi e^{a_\psi\left(i\bar{v}_{0z}\xi - f_\perp\right)}}{f_\perp^{\ 3}}\left[1 + a_\psi f_\perp\right]d\xi \tag{6.82}$$

$$\frac{d^2}{d\hat{z}^2}\hat{\tilde{E}}(0) = -i\hat{C}\frac{d}{d\hat{z}}\hat{\tilde{E}}(0), \tag{6.83}$$

$$\frac{d^3}{d\hat{z}^3}\hat{\tilde{E}}(0) = -\hat{C}^2\frac{d}{d\hat{z}}\hat{\tilde{E}}(0). \tag{6.84}$$

Combining equation (6.82), (6.83) and (6.84) with the homogeneous differential equation (6.77), we get the initial condition for the radiation field right after the electron beam entering the FEL[16]

$$\hat{\tilde{E}}(0) = -i\left[\hat{\Lambda}_p^{\,2} + \hat{q}^{\,2}\right]\frac{d}{d\hat{z}}\hat{\tilde{E}}(0). \tag{6.85}$$

Equation (6.82), (6.83) and (6.85) serves as the starting point of the radiation field and their evolution are determined by the solution of the homogenous equation (6.78), which can be written into the following matrix form,

$$\begin{pmatrix} \hat{E}(\hat{z}) \\ \frac{d}{d\hat{z}}\hat{E}(\hat{z}) \\ \frac{d^2}{d\hat{z}^2}\hat{E}(\hat{z}) \end{pmatrix} = \begin{pmatrix} e^{\lambda_1\hat{z}} & e^{\lambda_2\hat{z}} & e^{\lambda_3\hat{z}} \\ \lambda_1 e^{\lambda_1\hat{z}} & \lambda_2 e^{\lambda_2\hat{z}} & \lambda_3 e^{\lambda_3\hat{z}} \\ \lambda_1^2 e^{\lambda_1\hat{z}} & \lambda_2^2 e^{\lambda_2\hat{z}} & \lambda_3^2 e^{\lambda_3\hat{z}} \end{pmatrix}\begin{pmatrix} 1 & 1 & 1 \\ \lambda_1 & \lambda_2 & \lambda_3 \\ \lambda_1^2 & \lambda_2^2 & \lambda_3^2 \end{pmatrix}^{-1}\begin{pmatrix} -i\left(\hat{\Lambda}_p^2 + \hat{q}^2\right) \\ 1 \\ -\hat{C}^2 \end{pmatrix}\frac{d}{d\hat{z}}\hat{E}(0). \tag{6.86}$$

[16] Since the electric field is normalized by $E_0$, the factor $\theta_s$ is hidden in the normalization. The discontinuity of the radiation field comes from the discontinuity of $\theta_s$ but the current density is continuous at the entrance.

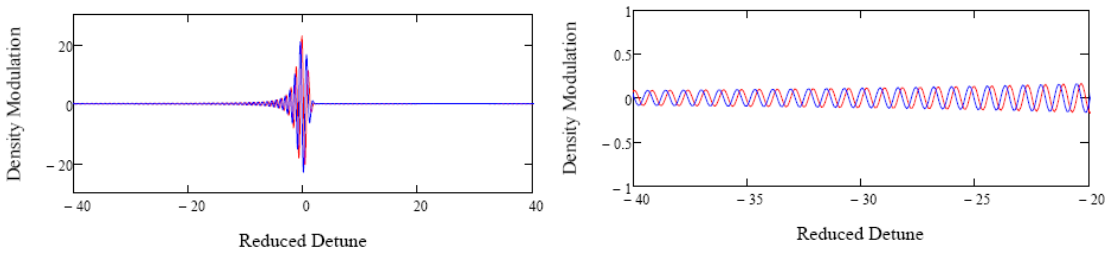


(a) (b)

Figure 6.14 The amplified current density in the frequency/detune domain calculated from equation (6.87) for $\hat{z}=8$, $\hat{q}=0$ and $\hat{\Lambda}_p=0$. The abscissa is the normalized detune and the ordinate is the current density in the frequency domain. The red solid curve is the real part of the current density and the blue solid curve is the imaginary part.

From equation (6.58), the evolution of the current density in the detune domain, i.e. frequency domain, is thus given by

$$\begin{aligned}\tilde{j}_1\left(\hat{z},\hat{C}\right) &= -ecn_0\left[A_1\left(\hat{C}\right)\lambda_1\left(\hat{C}\right)e^{\lambda_1\left(\hat{C}\right)\hat{z}} + A_2\lambda_2\left(\hat{C}\right)e^{\lambda_2\left(\hat{C}\right)\hat{z}} + A_3\lambda_3\left(\hat{C}\right)e^{\lambda_3\left(\hat{C}\right)\hat{z}}\right]\hat{E}'\left(0,\hat{C}\right) \\ &= \left[A_1\left(\hat{C}\right)\lambda_1\left(\hat{C}\right)e^{\lambda_1\left(\hat{C}\right)\hat{z}} + A_2\left(\hat{C}\right)\lambda_2\left(\hat{C}\right)e^{\lambda_2\left(\hat{C}\right)\hat{z}} + A_3\left(\hat{C}\right)\lambda_3\left(\hat{C}\right)e^{\lambda_3\left(\hat{C}\right)\hat{z}}\right]\tilde{j}_1\left(0,\hat{C}\right)\end{aligned} \tag{6.87}$$

, where $A_i\left(\hat{C}\right)$ are determined by

$$\begin{pmatrix}A_1\\A_2\\A_3\end{pmatrix} = \begin{pmatrix}1 & 1 & 1\\ \lambda_1 & \lambda_2 & \lambda_3\\ \lambda_1^2 & \lambda_2^2 & \lambda_3^2\end{pmatrix}^{-1}\begin{pmatrix}-i\left(\hat{\Lambda}_p^2+\hat{q}^2\right)\\ 1\\ -i\hat{C}\end{pmatrix}. \tag{6.88}$$

Figure 6.13 show $A_i$, $e^{\lambda_i\hat{z}}$ and $\lambda_i e^{\lambda_i\hat{z}}$ as a function of the detune $\hat{C}$. The long tail of figure 6.13 (c) is caused by the large imaginary part of the eigenvalue as $\left|\hat{C}\right|>>1$, which is related to the fact that the graph is plotted at $\hat{q}=0$ and $\hat{\Lambda}_p=0$. As there is no dispersion, Landau damping or plasma oscillation for such a case, the initial modulation will just stay

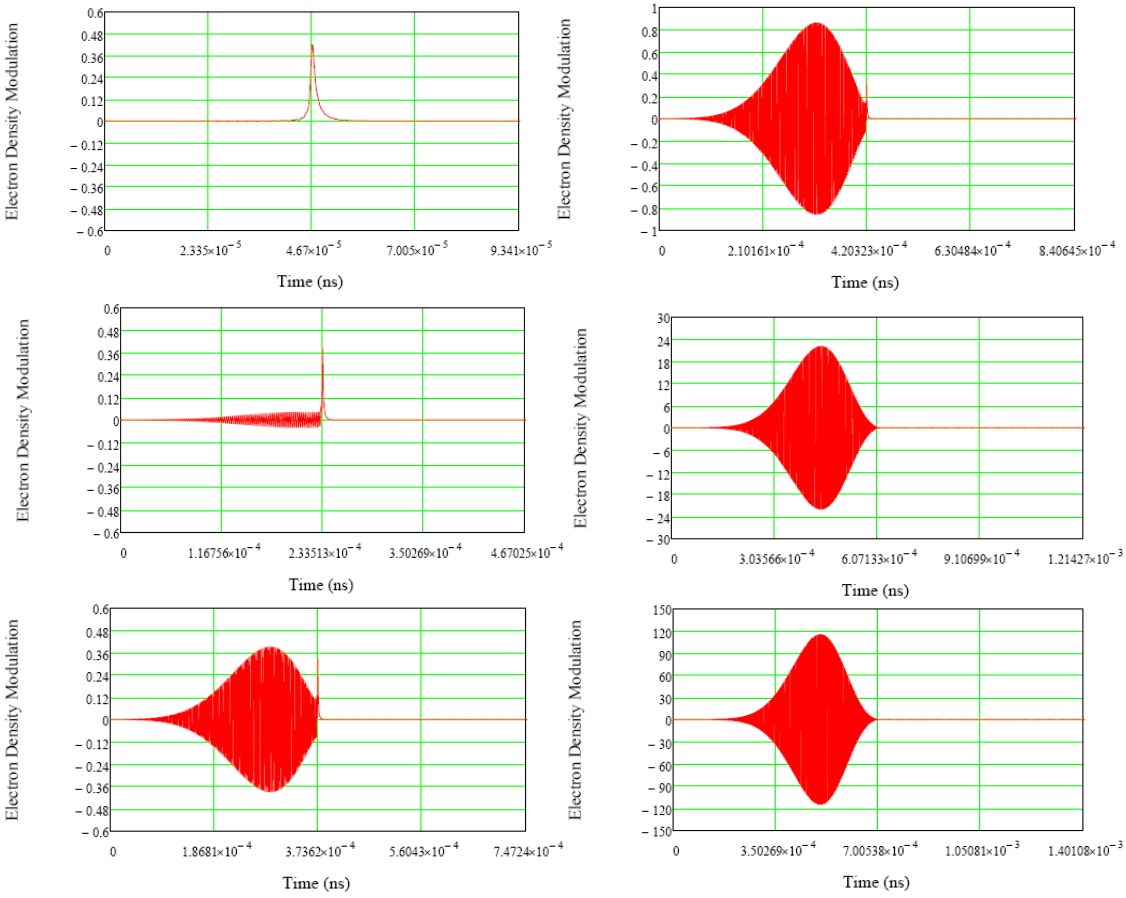


Figure 6.15 The evolution of the current density in an FEL. The abscissa are the time in units meter. The electron beam is going left wards and the origin is when the light/radiation field gets to the location. From up left to the down right, the plots shows the evolution of the current density at different location of the FEL for $\hat{z} = 1$, 5, 8, 9, 13 and 15 respectively. As $\hat{q} = 0$ and $\hat{\Lambda}_p = 0$, the initial modulation at the entrance stays unchanged.

on top of the amplified current density and thus left the initial broad band signal staying in the frequency domain as shown in figure (6.14) (b). The current density in the time domain is given by the inverse Fourier transformation (6.40). Since $\hat{k} = 2\gamma_z^2\left(\hat{k}_w - \hat{C}\right)$, the integration variable in (6.40) can be changed to the detune $\hat{C}$ as shown below,

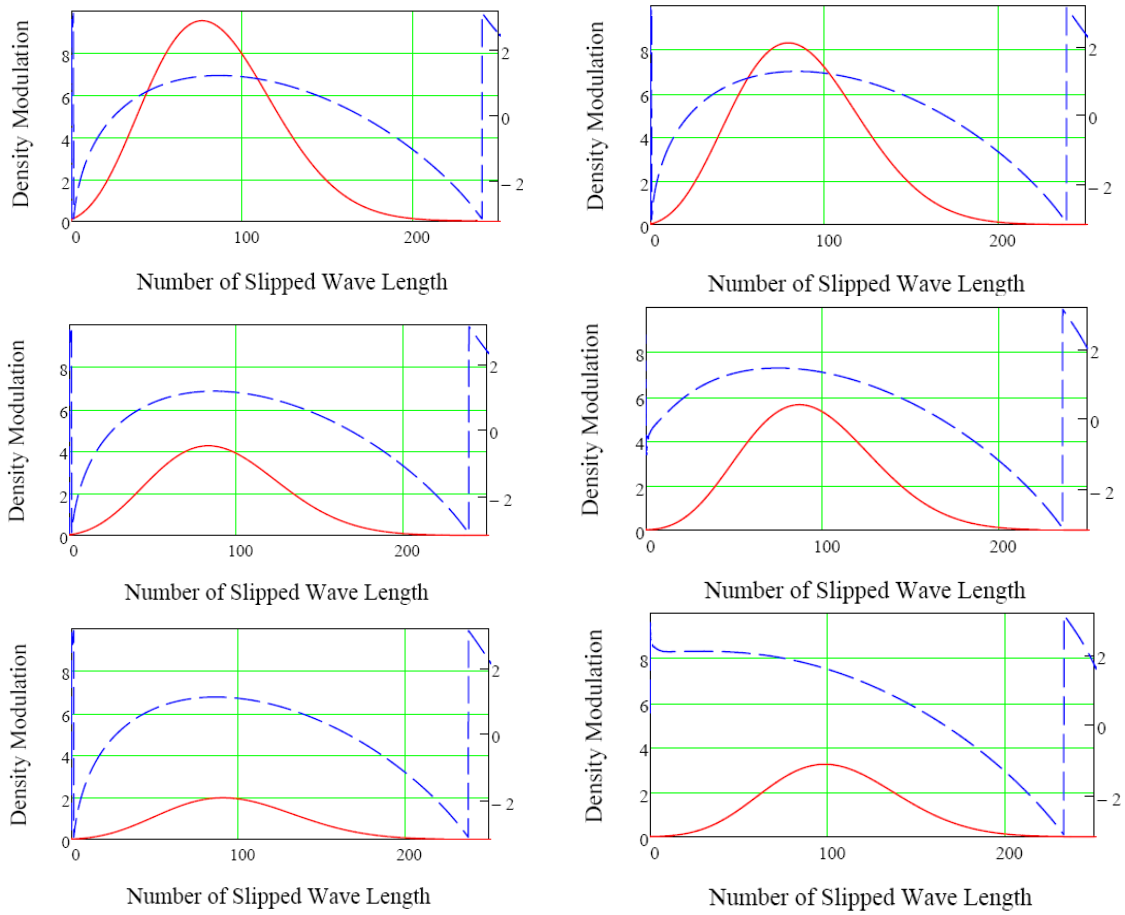


Figure 6.16 Space charge and energy spread effects to the FEL amplification. The abscissa is time in units of the resonant wavelength of the FEL. The initial electron modulation locates at the origin of abscissa and the electrons are moving rightwards. The ordinate is the amplitude (red solid curve) and the phase (blue dash curve) of the amplified wave-packet at $\hat{z} = 13$. The three graphs on the left shows the energy spread effects for $\hat{q} = 0.1$, 0.2 and 0.3 with no space charge effects and the three graphs on the right shows the space charge effects for $\hat{\Lambda}_p = 0.2$, 0.4 and 0.6 with energy spread being $\hat{q} = 0.1$[17].

$$\begin{aligned} \tilde{j}_1(z,t) &= \frac{c\Gamma}{2\pi} e^{i\hat{k}_w\hat{z}} \int_{-\infty}^{\infty} \hat{\tilde{j}}_1(\hat{z},\hat{C}) e^{i\hat{k}(\hat{z}-c\hat{t})} d\hat{k} \\ &= -\frac{c\Gamma 2\gamma_z^2}{2\pi} e^{i\hat{k}_w\hat{z}} e^{i2\gamma_z^2\hat{k}_w(\hat{z}-c\hat{t})} \int_{-\infty}^{\infty} \hat{\tilde{j}}_1(\hat{z},\hat{C}) e^{-i2\gamma_z^2(\hat{z}-c\hat{t})\hat{C}} d\hat{C} \end{aligned} \quad (6.88)$$

[17] For parameters shown in table 6.1, $\hat{\Lambda}_p \approx 0.2$ and $\hat{q} \approx 0.15$.

Inserting equation (6.87) into equation (6.88) and carrying out the integration over $\hat{C}$ generates the amplified current density in the time domain. Figure 6.15 shows the time domain current density evolution from $\hat{z}=1$ to $\hat{z}=15$ with $\hat{q}=0$ and $\hat{\Lambda}_p=0$. As previously expected, the initial modulation stays unchanged. One can also see from figure (6.15) that the wave-packet start to overtake the initial modulation after $\hat{z}\approx 8$. In SASE, this distance corresponds to the built-up time. Figure 6.16 shows the envelope and its phase of the amplified wave-packets, which is obtained by removing the fast oscillating factor as shown below

$$\tilde{j}_{1envelope}(z,t)=-\frac{c\Gamma 2\gamma_z^2}{2\pi}\int_{-\infty}^{\infty}\hat{\tilde{j}}_1(\hat{z},\hat{C})e^{-i2\gamma_z^2(\hat{z}-c\hat{t})\hat{C}}d\hat{C}\,. \tag{6.89}$$

| | | | |
|---|---|---|---|
| Energy, MeV | 136.2 | γ | 266.45 |
| Peak current, A | 100 | $\lambda_o$, nm | 700 |
| Bunchlength, psec | 50 | $\lambda_w$, cm | 5 |
| Emittance, norm | 5 mm mrad | $a_w$ | 0.994 |
| Energy spread | 0.03% | Wiggler | Helical |

Table 6.1 Designed Parameter Of CeC Amplifier for eRHIC (Taken from [19])

As one can see from figure (6.16), the energy spread reduces the amplification amplitude significantly due to Laudau damping and the initial modulation also disappears after certain distance of propagation due to the same reason. The group velocity of the wave-packets depends on the space charge and energy spread as well. As the space charge factor increases from 0.2 to 0.6, the slippage of the peak changes about 25%.

### 6.3.7 Summary and Discussion

There are two major approximations made in above calculations. The first one is ignoring the diffraction effects due to the finite transversal beam size and the other approximation is the Lorentzian energy distribution. In order to include the diffraction effects and consider the more realistic energy distribution, 3D simulation codes are usually used. However some useful scaling law such as the dependence of the group velocity on the energy spread and the space charge can be obtained through this analytical approach.

## REFERENCES


[1] J. Bosser, in *Advanced Accelerator Physics* (CERN Accelerator School, Rhodes, Greece, 1993), Vol. 2, p. 673.

[2] I. Ben-Zvi, in *EPAC 2006* (Edinburgh, Scotland, 2006), p. 936.

[3] I. Ben-zvi, in *COOL05*, edited by Sergei Nagaitsev and R. J. Pasquinelli (Galena, Illinois, 2005), Vol. 821, p. 75.

[4] V.V.Parkhomchuk and V.B.Reva, Journal of Experimental and Theoretical Physics **91**, 975 (2000).

[5] V.V.Parkhomchuk, Nuclear Instruments and Methods In Physics Research A **441**, 9 (2000).

[6] P.Zenkevich, A.Dolinskii, and I.Hofmann, Nuclear Instruments and Methods In Physics Research **A**, 454 (2004).

[7] Y. S. Derbenev, in *7th All Union Conference on Charged Particle Accelerators* (1980).

[8] V. N.Litvinenko and Y. S.Derbenev, in *29th International Free Electron Laser Conference* (Novosibirsk, Russia, 2007), p. 268.

[9] D.Reistad, T.Bergmark, H.Calen, et al., in *EPAC 2000* (Vienna, Austria, 2000), p. 576.

[10] A. Burov, Nuclear Instruments and Methods In Physics Research A **441**, 23 (2000).

[11] A. V. Fedotov, I. Ben-zvi, V. N. Litvinenko, et al., in *PAC'05* (Knoxville, Tennessee, 2005).

[12] A. Burov, Phys. Rev. ST Accel. Beams **9**, 120101 (2006).

[13] A. Fedotov, in *Electron Cooling Group Internal Reports* (Upton, New York, 2007).

[14] M.Blaskiewicz, J.M.Brennan, P.Cameron, et al., in *EPAC 2002* (Paris, France, 2002).

[15] S.Peggs and W.Mackay, in *RHIC/AP/36*, 1994).

[16] G.Wang, in *COOL05 Workshop* (Galena, Illinols, USA, 2005).

[17] J.L.Laclare, in *CERN Accelerator School: 5th General Accelerator Physics Course* (Jyvaskyla, Finland, 1992).

[18] W. Chong-Lung, Journal of Plasma Physics **25**, 225 (1981).

[19] V. N. Litvinenko, J. Bengtsson, I. Ben-zvi, et al., in *The 30th International Free Electron Laser Conference* (Gyeongju, Korea, 2008).

[20] D. Montgomery, G. Joyce, and R. Sugihara, Plasma Physics **10**, 681 to 686 (1967).

[21] G. Cooper, Physics of Fluids **12**, 2707 (1970).

[22] C. R. James and F. Vermeulen, Canadian Journal of Physics **48**, 349 (1970).

[23] A.J.Turski, Annals of Physics **35**, 240 (1965).

[24] A.J.Turski, Annalen der Physik **22**, 180 (1969).

[25] E.W.Laing, A.Lamont, and P.J.Fielding, Journal of Plasma Physics **5**, 441~454 (1971).

[26] C.-L. Wang, G. Joyce, and D.R.Nicholson, Journal of Plasma Physics **25**, 225 (1981).

[27] P. Chenevier, J.M. Dolique, and H.Peres, Journal of Plasma Physics **10**, 185 (1973).

[28] E.L.Saldin, E.A.Schneidmiller, and M.V.Yurkov, physics reports **260**, 187 (1995).

[29] E. L. Saldin, E. A. Schneidmiller, and M. V. Yurkov, *The Physics of Free Electron Lasers* (Springer, New York, 1999).